Dissertation

submitted to the
Combined Faculties for the Natural Sciences and for Mathematics
of the Ruperto-Carola University of Heidelberg, Germany
for the degree of
Doctor of Natural Sciences

presented by

Diplom-Physicist Sami Dib
born in: Beirut, Lebanon

Oral examination: 16$^{\text{th}}$ February 2005

Turbulence and structure formation in the interstellar medium

Referees: **Prof. Dr. Andreas Burkert**
Prof. Dr. Hans-Walter Rix

to Mahdi

Turbulenz und Strukturbildung im interstellaren Medium

Die Struktur und Dynamik des Interstellare Mediums (ISM) sind das Ergebnis der Wechselwirkung zwischen verschiedensten physikalischen Prozessen, wie z.B., Turbulenz, Gravitation, thermische Prozesse, Magnetfelder und kosmische Strahlung, die die Entstehung von Molekulwolken und Sternen beeinflussen, die wiederum die Eigenschaften einer Galaxie beschreiben. In dieser Arbeit wurde die Rolle der thermischen und graviativen Instabilität des ISMs im Detail untersucht. Unsere Ergebnisse zeigen, dass, thermische Instabilität (TI) massgeblich für die Strukturentwicklung des ISMs verantwortlich ist und dass sie das diffuse interstellare Gas um einen Faktor von ~ 100 komprimieren kann, was zur Entstehung von molekularen Strukturen führt. Diese Strukturen können gravitativ gebunden sein falls sie genügend hohe Dichten erreichen. Diese TI, die auf kleinen Skalen wirkt ($\lesssim 60$ pc), ist allerdings nicht in der Lage, die Turbulenz des ISMs zu erhalten. Die Turbulenz des ISMs findet ihren Ursprung wahrscheinlich eher auf grösseren galaktischen Skalen, z.B., durch Supernova-Explosionen oder galaktische Scherbewegung. Dies wird durch unsere Untersuchung der Zwerggalaxie Holmberg II bestätigt, in der Turbulenzen auf ~ 6 kpc erzeugt werden. Wir zeigen auch, dass die Wechselwirkung zwischen Turbulenz und TI die beobachtete Struktur des H I Gases in Holmberg II erklären kann. Weiterhin untersuchen wir, wie sich die Dynamik des ISM ändert, wenn die Turbulenz durch Supernova-Explosionen mit unterschiedlichen Raten erzeugt wird. Es war uns möglich zu zeigen, dass die konstante Geschwindigkeits-Dispersion in den äusseren Bereichen von Galaxien durch die Wechselwirkung von Supernova Explosionen und TI erklärt werden kann. Unsere Untersuchungen zeigen ausserdem, dass für den Fall, dass die Dichte des Gases und die Supernova-Raten dem Kennicutt-Gesetz folgen, eine Geschwindigkeits-Dispersion von $\sim 5-6$ km s^{-1} in den äusseren Bereichen von Galaxien erzeugt wird, was dies ist in guter Übereinstimmung mit Beobachtungen.

Turbulence and structure formation in the interstellar medium

The interstellar medium (ISM) structure and dynamics are the result of the interplay between many physical processes such as turbulence, gravity, thermal processes, magnetic fields and cosmic rays which determine the modes of molecular cloud and star formation, and which in turn, define the global galactic properties. In this thesis, we have examined in detail the role played by thermal and gravitational instabilities in the ISM. We have shown that thermal instability (TI) is an effective agent of structure formation in the ISM which can compress diffuse interstellar gas by a factor of ~ 100, leading to the formation of dense molecular structures, which can, if dense enough, become gravitationally bound. However, TI, which operates on small scales ($\lesssim 60$ pc), is unable to drive a self-sustained turbulence in the ISM. The bulk of turbulent motions is most likely injected into the ISM on larger scales by, e.g., supernova explosions or galactic shear. Confirming this idea, we find that turbulence is injected into the ISM of a dwarf irregular galaxy, i.e., Holmberg II, on a scale of ~ 6 kpc. We also show that the interaction of turbulence and TI can explain the observed large scale morphology of the H I gas in Holmberg II. Additionally, we investigate the dynamics of the ISM when the turbulence is driven by supernova explosions occurring at different rates in the medium. It was possible to show that the constancy of the velocity dispersion in the outer parts of galaxies can be explained as the result of the interplay between supernova driving and TI. We also showed that if the gas density and the supernova rates follow a Kennicutt-type law, the resulting velocity dispersion is of the order of $\sim 5-6$ km s^{-1} at the outer galactic radii, in perfect agreement with the observations.

Contents

1 The multiphase interstellar medium **1**
1.1 The observed ISM . . . 1
1.1.1 Molecular gas . . . 1
1.1.2 Neutral atomic gas . . . 3
1.1.3 Ionized gas . . . 6
1.1.4 Dust . . . 7
1.1.5 Magnetic fields . . . 8
1.1.6 Cosmic rays . . . 9
1.2 Turbulence in the ISM . . . 10
1.2.1 Turbulence supported molecular clouds ? . . . 11
1.2.2 Turbulence drivers in the ISM . . . 14
1.3 ISM models . . . 17
1.4 Outline of this thesis . . . 19

2 Equations and Analysis **21**
2.1 The hydrodynamics equations . . . 21
2.2 The code . . . 22
2.3 Clump finding and Virial analysis . . . 24
2.4 Generating artificial turbulence . . . 26
2.5 Scalings . . . 27

3 Gas instabilities in the interstellar medium **29**
3.1 Thermal instability . . . 29
3.1.1 The dynamical effect of thermal instability . . . 31
3.1.2 The effect of thermal conduction . . . 32
3.1.3 The effect of magnetic fields . . . 33
3.2 Gravitational instability . . . 34

4 A two phase model of the ISM **37**
4.1 Introduction . . . 37
4.2 A three-dimensional two-phase medium . . . 38
4.3 Parameter Study . . . 39
4.4 Analysis of an efficient cooling medium . . . 39
4.5 Does thermal instability drive turbulence ? . . . 44
4.6 The role of gravity . . . 47
4.7 Larson relations . . . 49

5 The origin of the H I holes in dwarf irregular galaxies **55**
5.1 Introduction . . . 55
5.2 The simulations . . . 58
5.3 From physical data to observations . . . 64
5.4 The observable quantity . . . 66
5.5 The physical size-correlation length relation in Ho II . . . 67
5.6 Comparing the models with the observations . . . 68
5.6.1 Comparison to the isothermal models . . . 68
5.6.2 Comparison to the models with cooling and heating . . . 69
5.7 Conclusions and discussion . . . 72

6 Supernova driven turbulence **75**
6.1 Introduction . . . 75
6.2 The model . . . 78
6.3 Analysis and derivation of the observables . . . 79
6.4 The effect of the feedback efficiency . . . 85
6.5 The supernova rate-velocity dispersion relation . . . 88
6.5.1 Comparison to the observations . . . 92
6.6 The need for improved models . . . 95
6.7 Summary and discussion . . . 99

7 Conclusions and perspectives **103**
7.1 Conclusions . . . 103
7.2 Perspectives . . . 106
7.2.1 On the small scales . . . 107
7.2.2 On the large scales . . . 108
7.2.3 AMR codes . . . 109

A Code scaling prescriptions **111**

Chapter 1

The multiphase interstellar medium

The interstellar medium (ISM) is the gas reservoir of galaxies albeit it constitutes only a small fraction of their total mass. In terms of the baryonic matter, the mass fraction of the ISM varies from ≤ 5 percent in elliptical galaxies (Young 2002) to $\sim$ 1-10 percent in spiral galaxies depending on the morphological type (Casoli et al. 1998, Ferrière 2001) and up to 60 percent in gas rich dwarf irregular galaxies (Tully et al. 1978; Warren et al. 2004). However, the ISM is not merely a passive substrate in which stars evolve. Interstellar matter exhibits wide temperature and density contrasts. Stars exchange mass and energy with the ISM at their birth, during the whole sequence of their evolution up to the very late stages of their existence. Under the influence of gravity, stars form in the densest regions of the ISM which are made of dense and cold molecular matter. In the interior of stars, galactic matter goes through a succession of thermonuclear reactions which ultimately leads to the enrichment of the gas in heavier elements. The newly processed matter is dragged out to the stars surface and is re-injected into the ISM by powerful stellar winds. At the end of their lifetimes, high mass stars ($\geq 8 - 10$ $M_\odot$) display a violent outburst (i.e., supernova) that will release the stellar matter back into the ISM. Supernovae also inject into the ISM a significant amount of energy ($\sim 10^{51}$ ergs) which, in addition of generating turbulent motions, will lead to strong compressions of the matter around them, giving eventually birth to new molecular regions prone to star formation.

1.1 The observed ISM

In this section, we present in more detail the different phases of the ISM and discuss the observational techniques commonly used to study their structure and dynamics. It borrows from the excellent reviews of Ferrière (2001), Vázquez-Semadeni et al. (2000b) and McKee (1999) and the thesis of Korpi (1999). The basic properties of the different phases of the ISM in the Galaxy are resumed in Tab. 1.1. The vertical columns represent the different phases of the ISM (in different theoretical models that will be addressed in § 1.3) and their typical number density, temperature, vertical scale height, volume filling factor and characteristic velocity dispersion.

Cold molecular medium (CMM)	n [cm^{-3}]	T [K]	h [pc]	F	σ [km s^{-1}]
SE	$10^2 - 10^6$	7-30	~ 65	$\sim 5 \times 10^{-4}$	0.1-3
Cold neutral medium (CNM)	n [cm^{-3}]	T [K]	h [pc]	F	σ [km s^{-1}]
FGH	20-30	60-90	~ 160	0.02-0.04	$\sim 4 - 15$
MO	42	80	...	0.024	
SE	20	80	90-100	0.02	
W	4.2-80	41-210	...	...	
Warm neutral medium (WNM)	n [cm^{-3}]	T [K]	h [pc]	F	σ [km s^{-1}]
FGH	0.1	10^4	160	0.96-0.98	6-15
MO	0.37	8000	...	0.146	
SE	0.3	6000	150	0.2	
W	0.1-0.59	5500-8700	...	...	
Warm ionized medium (WIM)	n [cm^{-3}]	T [K]	h [pc]	F	σ [km s^{-1}]
MO	0.25	8000	...	0.23	6-15
SE	0.03	8000	1500*	0.1	
Hot ionized medium (HIM)	n [cm^{-3}]	T [K]	h [pc]	F	σ [km s^{-1}]
MO	3.5^{-3}	4.5×10^5	...	0.60	$\gtrsim 15$
SE	3×10^{-3}	6.5×10^5	2400-5000	0.7	

Table 1.1: Parameters for the different phases of the ISM according to different authors. n is the number density, T the temperature, h the vertical scale height, F the volume filling factor and σ the characteristic velocity dispersion (from Cernicharo 1991). The different models are FGH : Field et al. (1969), MO : McKee and Ostriker (1977), SE : Scheffler and Elsaesser (1987) and W : Wolfire et al. (1995). The effective half thickness h in SE are calculated from a magneto-hydrodynamical model where gravitational acceleration is opposed by thermal, turbulent, magnetic and cosmic rays pressure and the value of h for the WIM is adopted from Boulares and Cox (1990).

1.1.1 Molecular gas

In our Galaxy, half of the mass of the ISM is in the form of molecular clouds (Genzel 1992). Molecular clouds span in mass from 10^3 $M_\odot$ up to 10^6 $M_\odot$ forming giant molecular clouds (GMCs) (Blitz 1993). At the image of the larger scale ISM, the structure of molecular clouds displays considerable inhomogeneity. Local density fluctuations (i.e., clumps) can be found in molecular clouds, which might, in some cases, host the sites of star formation (i.e., pre-stellar cores). Molecular clouds have been described to have a structure that is hierarchically nested (e.g., Scalo 1985; Vázquez-Semadeni 1994) or fractal (Falgarone et al. 1991). Molecular structures in the ISM are made principally of the H_2 molecule. Only the vibrationally exited lines around 2.2 μm of the H_2 molecule can be detected from the ground. These lines involve levels corresponding to temperatures of about 2500 K above the ground state, and are exited by fluorescence in the vicinity of star bursts or strong shock waves due to turbulence (Combes 2004). The pure rotational lines require space observations. The ISO satellite detected the first of these lines ($S(0)$ to $S(3)$) in many Galactic and extragalactic sources. In the particular case of NGC 891, Valentijn and van der Werf (1999) have detected the first two lines quite far from the center of the galaxy, with a radial emission profile which decreases much slower than the CO molecule luminosity profile. H_2 is also observed in absorption in the ultraviolet (UV) in front of nearby hot stars. Observations with the *FUSE* satellite have shown that molecular hydrogen is ubiquitous in the Galaxy (Shull et al. 2000; Rachford et al. 2001). The molecular fraction is only a few percent in translucent and diffuse clouds, peaking to higher values in dense molecular clouds. However the latter type of observations do not allow astronomers to probe the densest regions of molecular clouds where the UV radiation is obscured by high column densities (i.e., of dust and molecules) present in these regions. In the radio wavelength, the H_2 molecule is not directly observable : because it possesses no permanent electric dipole moment and has a very small moment of inertia, all its permitted transitions lie outside the radio domain (Field et al. 1966). Since cold molecular hydrogen does not radiate, the best tracer of molecular interstellar gas is the CO molecule (Scoville and Sanders 1987). The CO molecule has a small dipole ($\mu = 0.1$ Debye), and therefore requires only mild densities (~ 600 cm^{-3}) to be exited in its rotational lines that fall in the millimeter and sub-millimeter range. The molecule is relatively heavy so that the first level $J = 1$ is at 5.2 K above the ground state, and is therefore ideally suited to trace cold molecular material. Observations of the molecular component of the ISM are also performed using other tracers such as NH_3, CS and HCN which trace higher density regions in molecular clouds as they have higher density thresholds for excitation ($\sim 10^5$ cm^{-3}, $\sim 10^6$ cm^{-3} and $1.5{\times}10^7$ cm^{-3}, respectively, Combes 2004). Observed velocity dispersions in molecular clouds range from 4-15 km s^{-1} in the GMCs down to ~ 1 km s^{-1} in molecular cloud cores (Cernicharo 1991). Millimeter and sub-millimeter observations are carried out today with telescopes such as the IRAM 30 meter telescope, the IRAM Plateau de Bure interferometer (http://iram.fr), The Owens Valley Radio Observatory Millimeter Array (OVRO) and the BIMA array. The latter two arrays are to be merged very soon to form a more powerful telescope, namely the Combined Array for Research in Millimeter-wave Astronomy (CARMA) (http://www.mmarray.org).

1.1.2 Neutral atomic gas

Neutral atomic hydrogen (H I), is not directly observable at optical wavelengths. Under the thermodynamical conditions at which hydrogen atoms are neutral, particle collisions are so

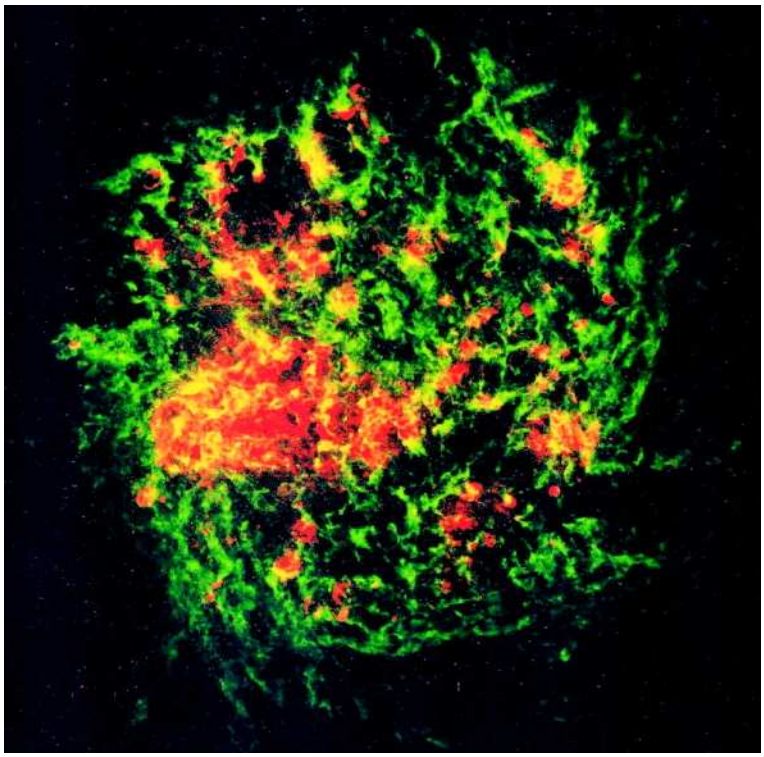

Figure 1.1: Peak H I brightness map (green) with overlaid Hα image (red) of the LMC. Adapted from Kim et al. (1999).

infrequent that nearly all hydrogen atoms have their electron in the ground energy level $n = 1$. It turns out that the electronic transitions between the ground level and an excited state- forming the Lyman series- lie in the UV, with the Lyman-α (Ly-α) transition between the ground level and the first excited state $n = 2$ occurring at a wavelength of 1216 Å. The Ly-α is observed in absorption against background sources. Using the Ly-α in absorption, large surveys of the Galaxy have been performed with the Wisconsin far-ultraviolet spectrometer aboard the $OAO - 2$ satellite (e.g., Savage and Jenkins 1972; Jenkins and Savage 1974) and with the *Copernicus* satellite Bohlin et al. (1978) and the the IUE satellite Shull and van Steenberg (1985a). However, the Ly-α line as a diagnostic tool of H I is plagued by the same extinction problems as the UV and optical molecular lines. Here also, one needs to turn to radio astronomy.

Radio observations of H I hydrogen are done in the 21 cm line which corresponds to the transition between the hyperfine structure levels $1^2\ S_{1/2}$, $F = 0$ and $F = 1$. These levels appear due to the interaction between the magnetic moment of the electron and that of the proton leading to a splitting of the electronic ground level into two extremely close energy levels. The major advantage of the 21 cm line photons resides in their ability to penetrate deep into the ISM, unhindered by extinction. However, the line transition probability is extremely small (i.e., $A_0 = 2.868 \times 10^{-15}\ \mathrm{s}^{-1}$), which means it is necessary to integrate over very long paths in order to obtain a significant signal in the line. Early on, H I maps indicated the presence of

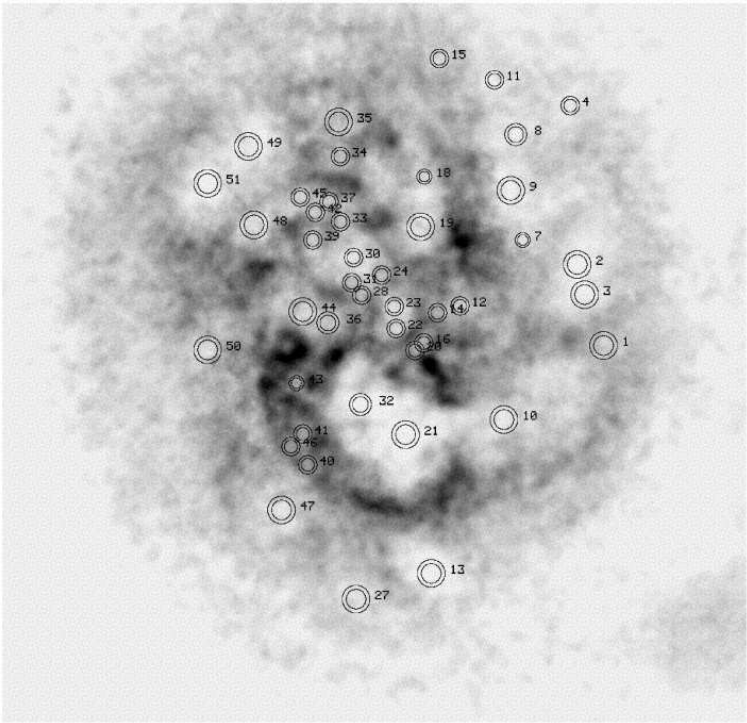

Figure 1.2: H I map of Holmberg II. Adapted from Rhode et al. (1999) who used the data of Puche et al. (1992). Color is inverted (i.e. black corresponds to high surface brightness). The locations of the (by eye) detected H I holes are indicated by the annuli.

the spiral arms in the Galaxy (Oort et al. 1958; Mihalas and Binney 1981), where the average density is found to be about four times larger than in the inter-arm region (Kulkarni et al. 1982). However, on top of the spiral structure, the cold H I gas in our galaxy shows a complex network of filaments, sheets and shells as observed in the Leiden-Dwingeloo H I survey (Hartmann and Burton 1997; see also Heiles 1979 and Dickey and Lockman 1990). Ehlerová et al. (2004) detected ~ 1000 shells and super-shells in the Leiden-Dwingeloo survey, with most of them being located in the Galactic disk. A component of warm neutral hydrogen (i.e., the warm neutral medium (WNM), see Tab. 1.1), predicted by Field et al. (1969) is also observed in the ISM. It has a smoother spatial distribution (Jahoda et al. 1990).

The shells and super-shells seen in the cold H I 21 cm line in the Galaxy are also observed in many nearby galaxies, mostly in gas rich dwarf irregular galaxies such as the Small Magellanic Cloud (SMC) (Stanimirovic et al. 1999), Holmberg II (Puche et al. 1992), the Large Magellanic Cloud (LMC) (Kim et al. 1999) and IC 2574 (Walter and Brinks 1999). The origin of the H I shell and super-shells structure, which for some of them are seen expanding, remains a debated issue. Whereas the smallest H I holes, located towards the center of galaxies are believed to be the result of strong stellar wind and supernova or multiple supernova explosion(s) (Tenorio-Tagle and Bodenheimer 1988), the holes in the outer parts of galactic disks where the star formation efficiency is low might have a different origin. Ideas such as turbulence clearing (Elmegreen 1997), thermal and gravitational instabilities (Wada et al.

2000) or a combination of turbulence and thermal instability effects, as will be detailed in Chap. 5, have been proposed.

Though H I is the most abundant specie in the atomic phase, it is not the dominant agent which regulates its dynamics at temperatures less than ~ 8000 K. Whereas cooling by the Ly-α emission line dominates the cooling for number densities $\lesssim 0.1$ cm^{-1}, other less abundant atoms such as carbon and oxygen play a significant role in the atomic phase of the ISM as their emission lines dominate the cooling of the ISM for number densities in the range $\sim 1 - 10^3$ cm^{-3} (Dalgarno and McCray 1972; Koyama and Inutsuka 2000). The heating and cooling of the ISM will be discussed in more detail in § 1.3.

1.1.3 Ionized gas

The ISM contains also components of warm (Reynolds 1989) and hot ionized gas (H II) (Spitzer and Jenkins 1975); labeled the warm ionized medium (WIM) and the hot ionized medium (HIM), respectively. The warm ionized medium can be found around O and B stars, which have a strong UV radiation capable of ionizing hydrogen atoms, thus creating the so called H II regions. Inside an H II region, ions and free electrons keep recombining until they are ionized by new UV photons coming from the star. The size of the H II regions is thus defined by the position at which the rate of recombination is equal to the rate of photoionization, and is called the Strömgren radius. The equilibrium happens at a temperature of ~ 8000 K, depending on density and metallicity (Mallik 1975). Helium atoms which have a number density of 9.7 percent of the total number density in the ISM are more difficult to ionize. Only stars with spectral types earlier than O8 emit photons which have energies that are higher than the helium ionization energy (24.6 ev). Helium is therefore usually ionized at a distance of the stars which is << to the Strömgren radius. Outside the H II regions, only photons with energies less than 13.6 ev (i.e., wavelength > 912 Å) can be found. These photons, however, are energetic enough to ionize the heavy elements such as C, O, Si and Fe. At standard elemental abundances (Anders and Grevesse 1989), This leads to a minimal ionization fraction in the H I medium of $\sim 10^{-4}$. WHAM observations by Haffner et al. (1999) (see also Reynolds 1985) in the Hα [H II] 6716 Å and [S II] 6583 Å lines show that the warm gas has temperatures in the range of $6 \times 10^3 - 10^4$K. They also inferred a vertical scale high of the WIM of ~ 1 kpc. The thick gaseous component associated with the warm neutral and ionized medium was also investigated using the 21 cm line in absorption in the foreground of pulsars (Harding and Harding 1982; Vivekanand and Narayan 1982).

The presence of hot ionized gas in the Galaxy has been predicted by Spitzer (1956). The most relevant methods to detect this hot gas are (Jenkins 2002): a) absorption by highly ionized atoms in the UV spectra of background sources (i.e., stars for the Galactic disk gas; quasars or active galactic nuclei (AGNs) for the Galactic halo or intra-group medium gas.), b) Soft -rays background radiation due to thermal emission indicative of the existence of a hot plasma. The ions Si IV, C IV, N V and O VI are the most suitable species to trace the collisionally dominated hot gas (i.e., temperature of a few 10^5 K) through their absorption features. The most useful ion being O VI, because its ionization potential is 114 ev which is more energetic than most of the photons emitted by the hottest stars. The values obtained for the Galactic vertical scale height of the hot gas from O VI (Savage et al. 2000; Wakker et al. 2003) and N V (Savage et al. 1997) observations vary significantly, and are in the range

of 1.6-3.9 kpc. In addition to the X-ray emission of the Local Bubble and the isotropic extragalactic emission, Snowden et al. (1998), using ROSAT 0.25-kev X-ray observations detected the presence of a 0.25-kev soft X-ray emission in the Galactic halo. Additionally, the emission exhibits intensity fluctuation, thereby suggesting the emitting gas has a patchy distribution. The derived densities are ~ 0.0065 cm^{-3}. Signatures of emission in the 0.5-1 kev band, shown to be associated with individual supernova remnant or with super-bubbles (i.e., produced by strong stellar winds and multiple supernova explosions) have been observed across the Galaxy, indicating the existence of a hot plasma with temperatures of a few 10^6 K (Aschenbach 1988; McCammon and Sanders 1990). Early X-ray observations in external spiral galaxies (Fabbiano 1989) show the existence of hot gas, radially decreasing outwards. High resolution Chandra and XMM-Netwon satellites observations of normal and starburst galaxies (Dahlem et al. 2003; Strickland et al. 2004a; Strickland et al. 2004b) show correlations between the surface brightness of the diffuse X-ray emission and the star formation rate in galactic disks.

1.1.4 Dust

The existence of dust in the Galaxy was first pointed out by Trumpler (1930). He noticed, when observing stars in some Galactic directions that their light is more dimmed than what is expected from the Pogson inversed squared dilution law. Trumpler (1930), already attributed this light extinction ($\equiv$ absorption+scattering) to the existence of *"fine cosmic dust particles of various size ...producing the observed selective absorption"*. Light is also observed to be more polarized in directions of stars with a higher reddening (Serkowski 1973; Clayton et al. 1992; Wolff et al. 1997). The extinction curves spectral features, that vary from star to star, can be explained by different compositions of dust grains. Spectral features are only observed at wavelength $\lambda > 912$ Å, below which most photons are absorbed by neutral hydrogen. The most prominent spectral feature in extinction curves is the the one at $\lambda = 2175$ Å, attributed to graphite particles (Stecher and Donn 1965; Mathis et al. 1977; Draine 1989). Infrared (IR) bands in extinction curves at 9.7 μm and 18 μm are also observed and attributed to the presence of silicates, and another feature at 3.4 μm is associated with hydrocarbons, mostly CH (Pendleton and Allamandola 2002). In the diffuse phase of the ISM, a large number of weaker features are observed, known as "diffuse interstellar bands" (DIBs) (Jenniskens and Desert 1994) and practically most of them are of unknown origin (Draine 2004). In cold molecular clouds, a strong absorption band is observed at 3 μm attributed to H_2O ice usually associated with other weaker "ice" features of CO, NH_3, CH_3OH and CO_2 (Draine 2004). In a variety of galactic objects, like planetary nebulae, H II regions and reflection nebulae emission in the 3-13 μm region are observed. They are believed to be associated with complex polycyclic aromatic hydrocarbon molecules (PAHs) (Cesarsky et al. 1996; Boulanger et al. 1998). The spectral shape of extinction curves may also be used to study the size distribution of interstellar dust grains. Mathis et al. (1977) were able to reproduce the standard extinction curve of the diffuse ISM in the wavelength interval 0.1-1 μm with a mixture of spherical graphite particles and silicates distributed in size according to the power low $a^{-3.5}da$ over a radius $a = 0.005 - 1$ μm for graphite particles and $a = 0.025 - 0.25$ μm for the silicates (see also Weingartner and Draine 2001a). Kim et al. (1994) showed, using a roughly similar graphite-silicate model to Mathis et al. (1977) that the power low index is shallower for large dust silicate particles (~ -3) in the diffuse clouds and that smaller dust particles ($\leq 0.1\mu m$) are depleted in cold clouds, which is accompanied by an increase in higher size particle densities.

The observations of reduced carbon interstellar abundance by Cardelli et al. (1996) and the need to fit other features of the dust radiation such as polarization or grain albedo exhorted authors to introduce other types of grains in the models such as PAHs (Li and Greenberg 1997) and water ice grains in cold clouds (Zubko et al. 1996). Assuming that the ISM elemental abundances (i.e., here the Local ISM) are similar to solar, another method for understanding the dust grains composition is to study interstellar depletion (i.e., atoms missing in the interstellar gas). The idea is that the missing elements are trapped in dust grains (Draine 2004).

Interstellar dust does not act merely as an absorber of optical light. Photons absorbed from starlight are re-radiated at longer wavelengths, mainly in the far-infrared. Observations with the *IRAS* and *COBE* satellites show the dust column density, derived from the intensities in the interval $100\ \mu m - 1\ mm$, and the H I column density in the diffuse phase and H_2 column density in molecular clouds to be be correlated (Boulanger and Pérault 1988; Boulanger et al. 1996). The temperatures of dust grains can be inferred from their infrared emission spectrum and are found to lie in the range $7 - 20$ K (Lagache et al. 1998). The origin of interstellar dust is, to this date, not fully understood. Nevertheless, what seems to be established is that dust forms in the envelopes of red giant and supergiant stars and in planetary nebulae and is ejected into the ISM by the stellar radiation pressure (Salpeter 1976; Draine 1990). However, the fact that shock waves from supernova explosions have been estimated to destroy interstellar gas at a rate which is higher than its injection rate from stars suggests that dust grains must form directly in the ISM (Jones et al. 1994). The dust to gas number densities ratio in the ISM is estimated to be, on average, around 0.01. Thus dust particles do not have a significant influence on the gas dynamics through their inertia. They contribute however to the heating and chemistry of the ISM. Re-emitted photons from dust grains are usually accompanied with the ejection of a photoelectron (i.e., photoelectric effect), which is, in most cases, the dominant mechanism for heating the interstellar gas (Wolfire et al. 1995; Weingartner and Draine 2001b). Dust particles act as catalyst for molecular cloud formation. In fact, the formation of H_2 is by far more important on dust grains as via the H^- or triple collisions paths (Smith and Rosen 2003; Koyama and Inutsuka 2000). This is part of a project we are currently working on and which will be briefly discussed in Chap. 7. Many instruments have been/are devoted to the study of interstellar dust like the IRAS and ISO satellites but perhaps the most fascinating observations are currently being obtained with the Spitzer Space Telescope (http://www.spitzer.caltech.edu).

1.1.5 Magnetic fields

Spiral (Ruzmaikin et al. 1988; Zweibel and Heiles 1997; Wielebinski and Krause 1993), elliptical (Moss and Shukurov 1996) and dwarf irregular galaxies (Chyży et al. 2000) are observed to possess magnetic fields. The presence of magnetic fields in the Galaxy was first revealed by the discovery of linear polarization of starlight in the optical (Hall 1949; Hiltner 1949). This polarization was explained in terms of the selective extinction by charged dust grains who are aligned with the magnetic field. Light is linearly polarized in the direction of the magnetic field (Davis and Greenstein 1951). In an effort to cover the whole sky, large databases of optical polarization where performed (Mathewson and Ford 1970; Heiles 2000). Stellar polarimetry, however, provides information about the direction of the field and not its strength.

Other methods have been used to derive the strength of the magnetic field. Discussing all

the underlying technical subtleties and a full coverage of the literature about Galactic (on the different scales) and extragalactic magnetic fields are far beyond the scope of this thesis and for a broader perspective, we refer the interested reader to the reviews by Beck et al. (1996) and Beck (2001). Here, we will only discuss the physical principles which stand behind each method and their limitations. The first method used to determine the strength of the magnetic field is based on the Zeeman-splitting of emission lines (usually the 21 cm H I emission line). The Zeeman splitting of a given atomic or molecular line is due to the interaction between the external magnetic field and the magnetic moment of the valence electrons. The amplitude of the Zeeman splitting $\delta\nu$ is directly proportional to the strength of the magnetic field. However, in the case of the 21 cm H I line, $\delta\nu$ is usually smaller than the linewidth itself and cannot be identified. One way to circumvent this problem is to observe the difference between the two circularly polarized components of the 21 cm emission which yields the value of the line of sight field, $B_{\|}$. Zeeman splitting, in addition of providing only an estimate of one component of the magnetic field, $B_{\|}$, is shown to be mostly suited for regions of relatively higher density $1 - 10^4$ cm^{-1} and is particularly used for observations towards molecular clouds and the Galactic center. The second method is the Faraday rotation of linearly polarized radio signals, which samples ionized regions and thus, is usually limited to low density regions ($n \leq 1$ cm^{-3}). The method is based on the following physical mechanism : A linearly polarized electromagnetic wave propagating along the magnetic field of an ionized medium can be decomposed into two circularly polarized modes, a right hand mode whose electric field $\vec{E}$ rotates about the magnetic field in the same sense as the free electrons gyrate around it and, a left hand mode whose $\vec{E}$ rotates in the opposite direction. The right hand mode therefore travels faster, and consequently the plane of polarization experiences a rotation known as the Faraday rotation, and is characterized by the rotation measure (RM) which is proportional to the line of sight electron number density and the line of sight magnetic field product RM $\propto \int_0^L n_e B_{\|} dl$, where dl is a distance element and n_e is determined from the so called dispersion measure $DM = \int_0^L n_e dl$ (Beck 2001). Faraday rotation is usually used to estimate the magnetic field in the Galaxy, in which the sources of linearly polarized light come from pulsars or extragalactic radio continuum sources. Faraday rotation has however a important caveat which is, in addition of providing only the line of sight component of the magnetic field and being applicable only to low density regions, is that it assumes $B_{\|}$ and n_e to be uncorrelated along the line of sight which is not necessarily true. However, Faraday rotation is commonly used to get an estimate of the magnetic field strength in external galaxies. The third method to measure the strength of the magnetic field uses the radio synchrotron emission from relativistic electrons. The synchrotron emissivity is proportional to the total magnetic field but it requires the knowledge of the relativistic electron energy spectral index. The method makes the assumption that the electron number density n_e and the total cosmic rays (ions+electrons) pressure are proportional and the additional assumption of equipartition between cosmic rays pressure P_{CR} and magnetic pressure P_{mag}. Once P_{mag} is determined, the magnetic field strength can be obtained as $B \propto \sqrt{P_{mag}}$.

Without going into a detailed comparison of the estimates yielded by the different methods for the Galactic magnetic field, the commonly accepted picture today is the following (Beck 2001) : The field strength is around 10 ± 3 μG at 3 kpc, drops to 6 ± 2 μG at the solar radius and drops further more at larger Galactic radii to a value of ~ 4 μG. The field strength is larger in spiral arms (10-20 μG) and could reach values as large as 1 mG in clouds compressed by

supernova shocks (Brogan et al. 2000) and in filaments near the Galactic center (Yusef-Zadeh et al. 1996). The large values of the magnetic field in molecular clouds have been thought to provide molecular clouds with support against gravity. This will be discussed in a bit more detail in § 1.2.1. In external galaxies, the mean equipartition strength of the total field was found to be 9 ± 3 μG in a sample of 74 spiral galaxies (Beck 2004). In this section we did not describe ideas about the origin of the magnetic field and its amplification processes in galaxies. We refer the interested reader to Kulsrud (1999) and Davies and Widrow (2000).

1.1.6 Cosmic rays

Cosmic rays are highly energetic, charged particles which are injected into the ISM by stellar winds (i.e., for the less energetic ones) and supernova explosions. Cosmic rays comprise essentially protons $\sim$ 87 %, helium nuclei $\sim$ 10 %, electrons $\sim$ 2 %, and smaller amounts of positrons and anti-protons (Blandford and Eichler 1987). Cosmic rays, which are trapped by the interstellar magnetic field, are further accelerated by the interaction with the electrons and ions present in the ISM or by supernova shock waves (Blandford and Ostriker 1978). The fate of cosmic rays is either to end up losing all their energy in inelastic collisions with interstellar gas particles, ionize gas particles, or escape from the Galaxy. They could escape from the Galaxy either by streaming across magnetic field lines in which the Galactic magnetic field connects with a weak extragalactic field, or simply diffuse across the Galactic magnetic field at the outer edges of the Galaxy (Jokipii and Parker 1969; Ferrière 2001). The primary cosmic-ray flux can be calculated by equating the injection rate to the loss rate and is found to be $\sim 1.8 - 10 \times 10^{-17}$ s^{-1} (Wolfire et al. 1995). The electrons ejected from the ionization of gas particles by cosmic rays contribute to the heating of the ISM (Wolfire et al. 1995; Shull and van Steenberg 1985b). The primary ejected electrons have a mean energy of 35 ev (Spitzer 1978) and thus, are energetic enough to produce a second ionization. Cosmic rays ,injected by supernova explosions, could also trigger Parker instabilities and sustain the dynamo action in galactic disks (Hanasz and Lesch 2000; Hanasz and Lesch 2003; Hanasz et al. 2004).

1.2 Turbulence in the ISM

Flows with high enough Reynolds numbers ($Re = v\ l/\nu \geq 300$), where l is the size of the largest coherent fluid element, v its velocity and ν the kinematic viscosity, are known to be "turbulent" (Frisch 1995). Assuming the kinematic viscosity of a completely ionized gas to be $\nu = 1.2 \times 10^{-16} T^{5/2} \rho^{-1}$ cm^2 s^{-1} (Parker 1979) and adopting standard values of the ISM for the temperature and density (i.e., $T = 10^4$ K and $\rho = 2 \times 10^{-24}$ g cm^{-3}) yields Reynolds number in the range $Re \approx 5 \times 10^9$, which is a clear indication the medium is indeed turbulent. Observationally, the indication for turbulence is provided by the broadening of the observed atomic or molecular lines widths and which can not be attributed to thermal broadening alone (Larson 1981; Blitz 1993; Goodman et al. 1998). These broad lines are usually interpreted as the signature of random motions, or "turbulence". Using interstellar scintillations, which are fluctuations in the amplitude and waves of the radio emission associated with the turbulent structure of the ISM, Armstrong et al. (1995) derived the electron density spectrum in the ISM in the wavenumber range $10^{-13} - 10^{-6}$ m^{-1} and found that it is consistent with a Kolmogorov-type turbulence. Other measurements, on smaller scales, such as clouds densities or density fluctuations derived from measured velocity fluctuations, are shown on the same plot and seem

also to obey a Kolmogorov-like spectrum (see Faison and Goss 2001 for evidence of density fluctuations down to the 10-100 au scales). Ruzmaikin et al. (1988) however, argued that due to the large uncertainties in transforming the velocity fluctuations to density fluctuations the agreement with a Kolmogorov turbulence on the smaller scales might be accidental. The large Reynolds numbers indicate that viscous and Ohmic dissipation play a negligible role over many scales in the ISM. Energy cascades down from the scale on which it is injected to the medium L_{inj}, to the molecular dissipation scale L_d. The scales between L_{inj} and L_d are called the inertial range and the motions in that range are self-similar. For incompressible, isotropic and homogeneous flows, a dimensional analysis (e.g. Landau and Lifshitz 1959; Shu 1992; Cho et al. 2002) leads to Kolmogorov's cascade (Kolmogorov 1941) :

$$E(k) \propto k^{-5/3}, \tag{1.1}$$

where k is the wave number. In Kolmogorov turbulence, the kinetic turbulent energy E_k contained in the large eddies has no other way to dissipate than by interacting with the smaller ones, transferring to them a fraction of the energy. This process continues until the dissipation scale is reached and the kinetic energy will be turned into heat. MHD incompressible turbulence has to account for the anisotropy created by the magnetic field. As eddies motions parallel to the magnetic field are hindered (i.e., only magnetic waves i.e., Alfvén waves travel parallel to the field), Goldreich and Sridhar (1995) showed that the energy cascade is a Kolmogorov-like one for motions perpendicular to the magnetic field $E(k) \propto k_{\perp}^{-5/3}$, where $k_{\perp}$ is the wave number of motions perpendicular to the magnetic field. This result is not entirely surprising as the magnetic fields does not influence the motions which do not bend it. The interstellar medium is however far from this ideal picture, and can be easily assimilated to a compressible medium in which eddies of different sizes can interact directly by means of shocks and compressional waves. Ruzmaikin et al. (1988) discussed the role of weak compressibility on the turbulence cascade. In the case of a weak compressible medium (i.e., weak forcing of turbulence) they found that the energy cascades as $E(k) \propto k^{-3/2}$. For strong compressible turbulence, as shocks dissipate energy on all scales, Kolmogorov turbulence does not hold anymore and the cascade is usually described by the Burgers turbulence (Burgers 1974) which is described by

$$E(k) \propto k^{-2}, \tag{1.2}$$

where the power spectrum describes the Fourier structure of shocks. However, recent simulations by Cho and Lazarian (2003) show that the different MHD modes that exist in compressible turbulence have different energy cascades. Whereas they found Alfvén and slow waves to follow a Kolmogorov-like cascade, fast modes are found to follow a $E(k) = k^{-3/2}$ law. Cho et al. (2003) showed, in the case of a viscosity damped turbulence, that kinetic energy will cascade faster than Kolmogorov ($\approx k^{-4}$) whereas magnetic energy will cascade to the smaller scales slower ($\approx k^{-1}$). High resolution numerical simulations of hydrodynamical and MHD turbulence indicate that Kolmogorov theory might not be valid at all as they show the existence of a bottleneck effect which has not yet been predicted by any theory of turbulence (Kaneda et al. 2003; Haugen and Brandenburg 2004).

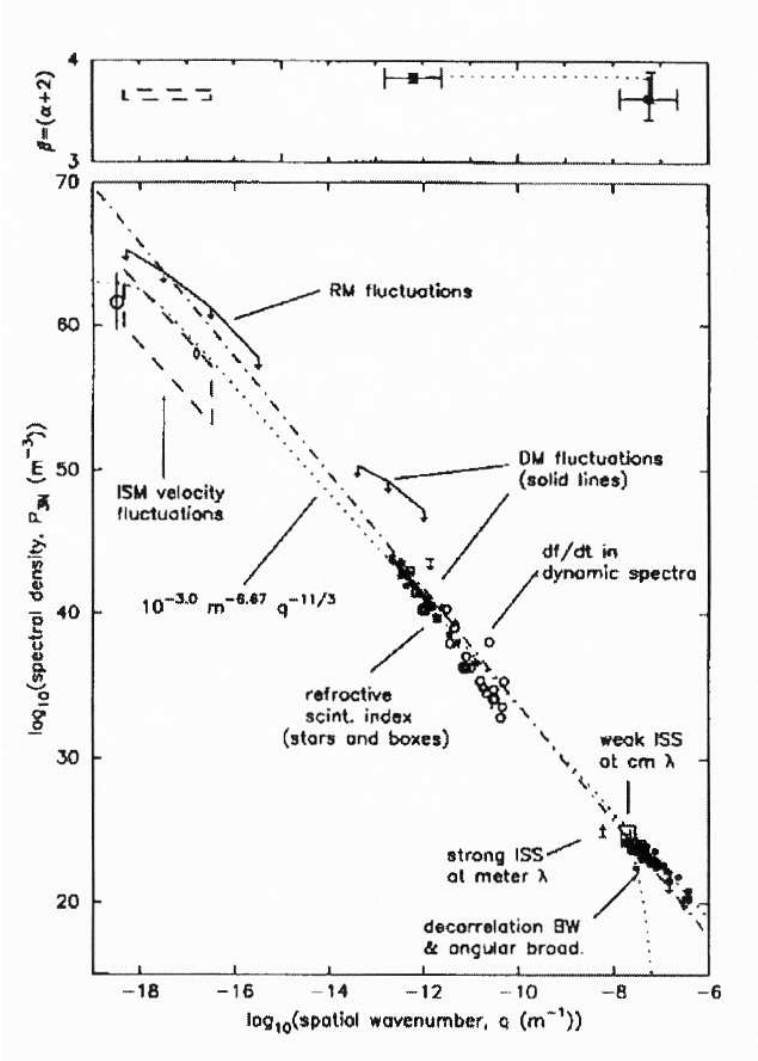

Figure 1.3: Three-dimensional electron density spectrum adapted from Armstrong et al. (1995). The data is compiled using different kinds of observations. The dotted line is a fit which is Kolmogorov-type with a spectral index $k = -11/3$. The dashed-dotted line is a model spectrum with spectral index $k = -4$, suggested by some other observations. Armstrong et al. (1995) interpret this data in terms of a Kolmogorov law for wave-numbers in the range $10^{-18} - 10^{-6}$ m^{-1}.

1.2.1 Turbulence supported molecular clouds ?

In the *classical theory* of star formation if all molecular clouds would have lifetimes of the order of their free-fall time,

$$t_{ff} = \sqrt{\frac{3\pi}{32G\rho}} \sim 1 \times 10^6 yr, \tag{1.3}$$

the rate of star formation in the Galaxy would be of the order of 250 M$_\odot$ yr^{-1} (McKee 1999),

which is substantially different from the averaged Galactic value yielded by the observations $\sim$ 3 $M_\odot$ (McKee and Williams 1997). This implies that molecular clouds are globally supported against gravitational collapse, though not necessarily locally as stars are observed to form in apparently globally stable clouds. The observed broad line widths in molecular clouds suggested that turbulence might play a role in supporting molecular clouds against gravity. Chandrasekhar (1951) investigated the role of micro-turbulence in the subsonic regime. This led him to describe turbulence as an additional pressure term which counteracts gravity and define an effective sound speed $c_{s,eff}$

$$c_{s,eff}^2 = c_s^2 + \frac{1}{3} < v^2 >, \tag{1.4}$$

where $\sqrt{< v^2 >}$ is the *rms* velocity dispersion in the flow and c_s the thermal sound speed. However, the hypothesis of micro-turbulence was proven invalid, as the ISM is seen to be turbulent on large scales, as large or even larger than considered observed systems (Stanimirović and Lazarian 2001; Ossenkopf and Mac Low 2002; Chap. 5 in this thesis). Other problems of this *classical theory* where gravitational collapse is balanced by the gas pressure and micro-turbulence, in addition to the very high expected star formation rates, is that it does not take into account the conservation of angular momentum during collapse nor it accounts for the role played by magnetic fields (see Mac Low and Klessen 2004). In fact, in the *classical theory*, the field lines are frozen to the matter and the magnetic flux ($\phi = \pi R^2 B$ where R is the total radius of the cloud) remains constant. Therefore the opposition to collapse by the magnetic pressure will remain constant during collapse, meaning that, if it was unable to prevent collapse in the early stages, it will remain unable to do so as the field is compressed. Mouschovias and Spitzer (1976) showed (see also Heitsch 2001), based on a Jeans (1902) similar analysis but in the presence of magnetic fields (see. Chap. 3 § 3.2 for the complete derivation of Jeans instability criterion) that there exists a critical mass M_{cr} for magnetostatic support and found that, for a spherical, self-gravitating cloud of radius R, mass M, and with a magnetic field of strength B is unstable if its mass is larger than M_{cr},

$$M > M_{cr} \equiv \frac{5^{3/2}}{48\pi^2} \frac{B^3}{G^{3/2}\rho^2}. \tag{1.5}$$

As Eq. 1.5 shows, the field strength and the density increase hand in hand in a contracting cloud as the collapse proceeds, making the case for magnetostatic support difficult. The possibility that mass could move across field lines was pointed out by Mestel and Spitzer (1956). They proposed that this process could occur, mostly for neutral gas, through the process of ion-neutral drift, known as ambipolar diffusion. For a cloud that is initially subcritical (i.e., magneto-statically stable), if neutral gas drifts to the center of the cloud across the field lines, the density at the center would increase while the magnetic field value remains unchanged. This would reduce the value of M_{cr} and slowly reduce the magnetic support. The timescale of ambipolar diffusion was found to be (for a detailed derivation see Mac Low and Klessen 2004)

$$\tau_{AD} \approx (25 Myrs) \left(\frac{B}{3\mu G}\right)^{-2} \left(\frac{n_n}{10^2 cm^{-3}}\right)^2 \left(\frac{R}{1pc}\right)^2 \left(\frac{x_e}{10^{-6}}\right), \tag{1.6}$$

where n_n is the neutral's number density and x_e the ionization fraction. τ_{AD} was found to be in good agreement with ages estimates of molecular clouds in the range 30-100 Myrs (Blitz

and Shu 1980; Solomon et al. 1987). Shu (1977) and Shu et al. (1987) further developed this model known as the *standard theory* of star formation. In this model, the system contracts in a first phase on a timescale of the order of τ_{AD} until a high central density builds up where the density enhancement builds up via ambipolar diffusion. The system then becomes unstable and the central parts start to collapse further in. In this inside-out collapse a rarefaction wave propagates outwards with the material ahead of it being at rest. The *standard theory* suffers an important drawback as it can only explain the formation of low mass stars from magnetically subcritical cores. The theory can not explain the formation of massive stars from a massive supercritical molecular cloud progenitor, nor does it address the problem of the formation of multiple stellar systems.

In a return to a more dynamical theory for star formation, Bonazzola et al. (1987) suggested a wavelength-dependence for turbulent motions such that the effective sound speed becomes

$$c_{s,eff}^2 = c_s^2 + \frac{1}{3}v^2(k). \tag{1.7}$$

In this formulation, the stability of the system does not only depend on the total amount of kinetic energy (i.e., to be compared with the gravitational energy) but also on its distribution on the different physical scales since $v^2(k)$ depends on the turbulent power spectrum (see also Vázquez-Semadeni and Gazol 1995). These analytical attempts to describe turbulence in molecular clouds are limited as they are restricted to the incompressible regime which is not the case of molecular clouds which show extreme non uniform structures. With the advent of more powerful computing machines, it became crucial to test the interplay between turbulence, gravity and magnetic fields and their effects on the star formation process. Simulations of supersonic, compressible turbulence show that the turbulence is dissipated on a timescale that is less than the free fall time (Stone et al. 1998; Mac Low 1999; Smith et al. 2000). The Inclusion of magnetic fields in the simulations was though to slow down energy dissipation by supporting the clouds magneto-dynamically (McKee and Zweibel 1995). However, numerical simulations show that, here also, MHD-turbulence decays on a timescale of the order of the global free-fall time (Stone et al. 1998; Mac Low 1999; Smith et al. 2000; Heitsch et al. 2001). In these simulations strong compressions by converging supersonic shocks can lead to star formation locally but for the cloud to be globally stable, turbulence or MHD-turbulence has to be constantly driven (see Vázquez-Semadeni et al. 2000b; Mac Low and Klessen 2004 for a more detailed discussion). In the past few years, new ideas has emerged in which clouds are believed to be transient features which form as a result of convergent flows on larger scales in the ISM. In that context the molecular cloud's evolution would depend much on the dynamics of the flow that formed them and the reservoir of mass around them. This would solve to some extent the problem of the global support and the star formation efficiency (Ballesteros-Paredes et al. 1999a; Elmegreen 2000; Ballesteros-Paredes 2004). In this scenario some molecular cloud cores, though dynamically evolving could even be seen in *hydrostatic equilibrium disguise* (Ballesteros-Paredes et al. 2003). According to Ballesteros-Paredes et al. (1999a), this would also explain the lack of 5-10 Myrs old post-T Tauri stars associated with star-forming molecular clouds. We will investigate this scenario in Chap .4, additionally accounting for the effects of thermal instability.

1.2.2 Turbulence drivers in the ISM

Mac Low and Klessen (2004) and Mac Low (2004) reviewed the energy injection into the ISM from several energy sources. These include the magneto-rotational instability (MRI), large scale gravitational instabilities, proto-stellar outflows and H II regions, stellar winds and supernova explosions. Some other mechanisms to stir up the gas in galactic disks such as the role played by tidal interactions with satellite galaxies remain unexplored, and may play a role in injecting a non-negligible amount of kinetic energy into in the ISM.

Magneto-rotational instability

Early on, galactic shear has been considered as a source of energy input into the ISM (Fleck 1981). Galactic shear, however, injects energy on scales of the order of a few kpc. One mechanism to couple the large scale flows to the smaller scale in galactic disks is the magneto-rotational instability (MRI) discussed in detail by Balbus and Hawley (1991) and Hawley and Balbus (1991). The instability generates Maxwell stresses that transfer the energy from shear to turbulent motions. The MRI has an associated energy injection rate of

$$e_{MRI} = \left(3 \times 10^{-29} erg\ cm^{-3}\ s^{-1}\right) \left(\frac{B}{3\mu G}\right)^2 \left(\frac{\Omega}{(220 Myrs)^{-1}}\right). \tag{1.8}$$

It was argued by Sellwood and Balbus (1999) and Mac Low and Klessen (2004) that the energy injected by the MRI may provide an amount of energy that can keep maintain a minimum value of the velocity dispersion in galactic disks, notably in their extended gaseous parts. Piontek and Ostriker (2004) studied, with two-dimensional numerical simulations, MRI developing in a medium subject to thermal instability. Their results indicate that the *rms* turbulent velocities can reach, at most, values of the order $\sim$ 1.2 km s^{-1}, which are much smaller than the observed turbulent velocities in the ISM. Three-dimensional isothermal simulations by (Dziourkevitch et al. 2004) show that a turbulent velocity field with a value of 3 km s^{-1} can be reached in the very inner parts of the disk, but falls rapidly with increasing radius well below the observed constant velocity dispersion value of $\sim$ 5-6 km s^{-1} observed in the external parts of galactic disks (e.g., Dickey et al. 1990). We will discuss this issue in much more detail in Chap. 6.

Thermal and gravitational instabilities

Gravitational instability is a mechanism which can transform gravitational energy into turbulent motions. However, as mentioned in § 1.2.1, turbulence decays faster than the free fall time scale, meaning that gravitational collapse can not sustain turbulence by itself. It is rather believed that gravitational instabilities help transfer energy from the larger galactic scales down to molecular clouds and molecular cloud cores scales. The idea is that shear might lead to local over-densities which can grow (e.g., by thermal instability) until they reach the stage of gravitational contraction. However, the compression of the diffuse gas, which has a mean number density of $\sim 0.1 - 0.5$, by a factor of 50-100 can only proceed through the effect of thermal instability in which local over-densities cool faster then the surrounding medium in a runaway mechanism until they achieve pressure equilibrium with the surrounding medium. However, in the two-dimensional simulations of Piontek and Ostriker (2004), the turbulence generated from the operation of thermal instability alone leads to *rms* velocities of the order $\sim$ 0.45 km s^{-1}, 0.25 km s^{-1} and 0.15 km s^{-1} for the unstable, warm

and cold phases, respectively. These values are all subsonic and at least an order of magnitude below the observed *rms* turbulent velocities in the ISM. Once densities of $\sim 50 - 100$ cm^{-3} are reached, self-gravity starts to operate on the condensations. In a series of papers, Wada and Norman (1999, 2001), Wada et al. (2000) and Wada et al. (2002) investigated this mechanism with two dimensional numerical simulations. The interplay between turbulence, thermal and gravitational instabilities is a problem we shall address in more detail in Chaps. 4 and 5 with three-dimensional numerical simulations. Wada et al. (2002) provided an estimate of the energy input from gravitational instabilities (only) which is

$$e_{inst} = \left(4 \times 10^{-29} erg\ cm^{-3}\ s^{-1}\right) \left(\frac{\Sigma_g}{10\ M_\odot pc^{-2}}\right)^2 \left(\frac{H}{100\ pc}\right) \left(\frac{\lambda}{100\ pc}\right)^2 \left(\frac{\Omega}{(220\ Myrs)^{-1}}\right), \tag{1.9}$$

where Σ_g is the surface density of the gas, H the vertical scale height of the gas, λ the characteristic length scale of turbulence which in practice is the characteristic scale on which velocity fluctuations develop around and inside the gas condensations, and Ω is the angular velocity of the disk. Galactic shear is not the only large scale perturbation that can inject energy into the medium. Shocks induced by the passage of spiral arms can provide strong compressions in which thermal and gravitational instabilities can develop thus contributing to the driving of interstellar turbulence (Gómez and Cox 2002). However, it is clear that the interplay between spiral arms compressions and thermal and gravitational instabilities can not solely account for the observed ISM turbulence. Many galaxies which do not possess a spiral structure show evidence for a turbulent ISM such as dwarf irregular galaxies but also the extended gaseous parts of spirals where the compression by spiral density waves is weak.

proto-stellar outflows

Proto-stellar jets and outflows deliver kinetic and thermal energy into the ISM. The total amount of energy ejected by a solar-type protostar of radius $R = 10R_\odot$ has been estimated by Mac Low and Klessen (2004) to be

$$e_{outflow} \approx \left(2 \times 10^{-28} erg\ cm^{-3} s^{-1}\right) \left(\frac{H}{200\ pc}\right)^{-1} \left(\frac{f_w}{0.4}\right) \times \left(\frac{v_w}{200\ km\ s^{-1}}\right) \left(\frac{v_{rms}}{10\ km\ s^{-1}}\right) \left(\frac{\Sigma_{SF}}{4.5 \times 10^{-9} M_\odot\ pc^{-2}\ yr^{-1}}\right), \tag{1.10}$$

where H is the scale height for star formation in the disk, f_w is the ratio of the ejected to accreted mass by the protostar (McKee 1989), estimated to be around 0.4 (Shu et al. 1988), v_w and v_{rms} are the velocity of the outflow and *rms* velocity of the ISM and Σ_{SF} is a typical value for the surface density of star formation.

stellar winds

The energy release by stellar winds of massive stars is a less instantaneous event than a supernova explosion. Ruzmaikin et al. (1988) estimated the energy release in massive stars to be of the order of $\approx 3 \times 10^{49}$ ergs during ≈ 3 Myrs. Abbott (1982) estimated the energy injection from stellar winds to be $e_{winds} \approx 2 \times 1.2 \times 10^{-27}$ erg particle^{-1} s^{-1}. Assuming an

average number density of the ISM of ≈ 0.3 cm^{-3} yields an energy injection rate per unit volume of $\approx 3.6 \times 10^{-28}$ ergs cm^{-30} s^{-1}.

$$e_{winds} \approx 3.6 \times 10^{-28} erg\ cm^{-3}\ s^{-1} \tag{1.11}$$

H II regions

Another way stars and particularly massive O and B stars inject energy in the ISM is through their ionizing radiation. The radiation pressure can be, in some circumstances, so high that it can lead to the total disruption of the parent molecular cloud core (Kessel-Deynet and Burkert 2003). Abbott (1982), estimated the total amount of ionizing radiation in the Galactic disk to be of the order 1.5×10^{-24} erg s^{-1} cm^{-3}. As already discussed in § 1.1.3, the radiation which heats the H II regions to temperatures of the order 10^4 K causes them to be over-pressurized with respect to the surrounding medium. In this expansion phase, a fraction of the total energy is transferred to the surrounding medium in the form of kinetic energy. For the Milky Way, Mac Low and Klessen (2004) estimated the energy deposited by H II regions in the diffuse phase of the ISM to be

$$e_{\rm H\,II} = \left(3 \times 10^{-30} erg\ s^{-1}\ cm^{-3}\right) \left(\frac{N_H}{1.5 \times cm^{-2}}\right)^{-3/14} \left(\frac{M_{cl}}{10^6 M_\odot}\right)^{1/14} \left(\frac{< M_\star >}{440 M_\odot}\right) \left(\frac{\mathcal{N}(>1)}{650}\right) \left(\frac{v_i}{10\ km\ s^{-1}}\right) \left(\frac{H_c}{100\ pc}\right)^{-1} \left(\frac{R_{sf}}{15\ kpc}\right)^{-2} \left(\frac{t_i}{18.5\ Myrs}\right)^{-1}, \tag{1.12}$$

where N_H is the mean Galactic neutral hydrogen clouds column density (Solomon et al. 1987), M_{cl} the typical mass of Galactic molecular clouds, $< M_\star >$ the mean mass of the Galaxy's stellar clusters which is ~ 440 M$_\odot$ (Matzner 2002), $\mathcal{N}$ is the number of OB associations with an ionizing photon luminosity exceeding 10^{49} s^{-1} and which are susceptible of delivering kinetic energy to the surrounding medium during their expansion and v_i the H II region expansion velocity. H_c is the scale height for massive clusters which in the Galaxy has a value of ~ 100 pc (Bronfman et al. 2000), very similar to the scale height of supernova type II found by Miller and Scalo (1979). R_{sf} is the radius of the star forming disk (i.e., 15 kpc in the Galaxy) and t_i is the cumulative time for massive star formation in clusters. McKee and Williams (1997) estimated that there is about five generations of massive star formation in a cluster, on average, with an average age for each generation of ~ 3.7 Myrs.

Supernova explosions

Mac Low and Klessen (2004) estimated the total energy injection from supernova type II explosions, normalized to Galactic values, to be

$$e_{SN} \approx \left(3 \times 10^{-26} erg\ cm^{-3} s^{-1}\right) \left(\frac{\epsilon_k}{0.1}\right) \left(\frac{\eta_{SN}}{1\ SNu}\right) \left(\frac{H_c}{100\ pc}\right)^{-1} \times \left(\frac{R_{sf}}{15\ kpc}\right)^{-2} \left(\frac{E_{SN}}{10^{51}\ ergs}\right). \tag{1.13}$$

H_c and R_{sf} are the same quantities defined earlier in Eq. 1.12. ϵ_k is the fraction of the energy transmitted into the ISM which goes into kinetic energy. Thornton et al. (1998) showed,

using one-dimensional supernova explosions simulations into the ISM, for a solar metallicity environment and for an ISM number density of 1 cm^{-3}, that around 20 percent of the total supernova energy is injected into the medium, equally distributed in kinetic and thermal energy. In Eq. 1.13, presented by Mac Low and Klessen (2004), it is likely that they have considered only the kinetic energy part of the energy therfore setting the normalization of ϵ_k to 0.1. η_{SN} is the supernova rate. Recent estimates of galactic supernova rates along the Hubble sequence has been performed by Cappellaro et al. (1999). They calculated the supernova rates for S0a-b galaxies to be 0.72 ± 0.21 SNu and 1.21 ± 0.37 for Sbc-d where 1 SNu = 1 SN (100 yr)$^{-1}$ $(10^{10} L_B/L_\odot)^{-1}$ and L_B is the Galactic luminosity in the blue. Mac Low and Klessen (2004) assumed that the Milky Way is lying between an Sb and Sbc type and assumed a Galactic supernova rate of 1 SNu. Using a Hubble constant value of 70 km s^{-1} rather than 75 km s^{-1} used by Mac Low and Klessen (2004), we find that the Supernova type II frequency is 1/57 yr^{-1}. E_{SN} is the total energy input of each supernova explosions. We use $E_{SN} = 10^{51}$ ergs. In any case, the small differences in estimating the supernova rate of the energy input do not change significantly the total supernova energetic input to the Galaxy in terms of kinetic energy, at most they do by a factor of 2.

The previous estimates of the energy input into the ISM from several physical processes show that supernova explosions are the dominant source of energy input into the ISM. However, these estimates are global ones which do not take into account the radial density profiles of the gas in galaxies and the efficiency of each of those physical processes at different radii. It also does not take into account how a physical process might be reduced in efficiency in the presence of one or more processes. For example, recent simulations show that the MRI might be "switched of" in the presence of stellar feedback (Korpi, private communication). In Chaps. 4 and 5 we will study the evolution of a turbulent medium in the presence of thermal and gravitational instabilities and in Chap. 6 the interplay between thermal instability and supernova feedback.

1.3 ISM models

In this section, we summarize some of the most relevant analytical and numerical models of the ISM over the last few decades, discuss some of their predictions and results, and confront them to observations. The first discussion on the existence of different phases in the ISM was delivered by Spitzer (1956) who explained the presence of observed H I clouds at high Galactic latitudes by the existence of a hot coronal gas in pressure equilibrium with the clouds. As discussed by Spitzer (1956), direct observations of the hot phase were not possible at that time. In the Galactic disk, Field (1962), was the first to suggest the existence of pressure confined cold H I clouds in a more diffuse, thermally stable gas at a temperature of $\sim 10^4$ K. This served as the basis of the model developed later on by Field et al. (1969) (hereafter FGH). The latter authors argued that the inter-cloud medium unstable phase can not exist because it could be only a transient feature. They developed an analytical model with two thermally stable phases at $T = 10^4$ K and $T \sim 300$ K. In the model of FGH, the Warm phase, heated by cosmic rays, occupies a large fraction of the volume (see. Tab. 1.1), whereas cold clouds assemble under the effect of cooling and gravity. Thermal instability has been invoked in that context to explain the formation of molecular clouds from the diffuse

interstellar clouds. Though the model ignored the hot phase, it offered a good description for the CNM and WNM phases with the exception that it has overestimated the heating from cosmic rays and ignored photoelectric heating which is a more dominant heating mechanism (Wolfire et al. 1995; McKee 1995).

Observations of soft X-rays and UV radiation in the ISM (e.g., Gorenstein et al. 1974; Jenkins and Meloy 1974; York 1974) prompted the inclusion into the model of a third, hot ($T \sim 10^6$ K) component of the ISM. Cox and Smith (1974) and McKee and Ostriker (1977) (hereafter MO) suggested that the hot medium represents the interior of expanding supernova remnants, which sweep surrounding material away from the explosion site. In the model of MO, cold clouds are embedded in layers of WNM and WIM gas. These onion-skin like clouds are located in the non-swept up regions by the supernova remnants (see Fig. 1 in McKee and Ostriker 1977) and particularly at the compressed, outer rims of the expanding and cooling shells. With only minor differences, the three-phase model described in Scheffler and Elsaesser (1987) is globally very similar to the model of MO (see Tab. 1.1). The essential drawback of these analytical two- and three-phase models is that they are statical. They do not account for the spectrum of shocks that can be present in the ISM and its effects on the topology of the different phases and their volume filling factors nor do they take into account a realistic structure of the Galaxy. Thus, the MO model estimates the volume filling factor of the hot gas to be ~ 0.6 whereas it has been shown, later on, both theoretically and from observations that this value is in the range 0.25-0.40 (see Ferrière 1998b; Tenorio-Tagle and Bodenheimer 1988). The complex structure of filaments, sheets and shells of the H I gas, discussed in § 1.1.2, do not resemble the onion-skin structure suggested by the MO and SE models. Additionally, these models do not describe the molecular phase of the ISM which reside in the form of clouds or cloud complexes (§ 1.1.1).

Vázquez-Semadeni (2002) reviewed the most relevant numerical ISM models. The first two-dimensional numerical models of the ISM, mimicking the Galactic plane were calculated by Bania and Lyon (1980), Chiang and Prendergast (1985) and Chiang and Bregman (1988). In the model of Chiang and Bregman (1988), which contains a gaseous and a stellar component, a "star formation" instability can be identified. This self-propagating star formation can be seen in many models where star formation is based on a density criterion and non-random recipe coupled to the gas self-gravity (e.g., Vázquez-Semadeni and Gazol 1995) and eventually to other physical processes like magnetic fields and Galactic shear (e.g., Passot et al. 1995) or stellar feedback (e.g., Gerritsen and Icke 1997; Gazol-Patiño and Passot 1999; Wada and Norman 2001). Other properties of the star formation process, such as the slope of the two-point correlation function describing the clustering of newly formed stars, can also be explained in the frame of these numerical models (Scalo and Chappell 1999). two-dimensional numerical simulations of a multiphase medium which enable high spatial resolution are still performed to study in detail specific process such as thermal instability (Piontek and Ostriker 2004) or the fueling of the gas into the center of galaxies (Wada and Norman 1999). The trend however, in the last decade, is to resort to three-dimensional simulations. As these three-dimensional simulations become numerically very expensive, authors investigate specific processes while omitting (or simplifying) others. Brandenburg et al. (1995) studied the dynamo action in a Galactic sheared flow whereas global simulations performed by Wada and Norman (2001) focused on the global dynamics and turbulence generations in the disk. Most of the three-dimensional simulations including supernova feedback focused on the problem

of the disk halo interaction and the evolution of super-bubbles in a turbulent ISM (Korpi 1999; Korpi et al. 1999a; de Avillez 2000; de Avillez and Breitschwerdt 2004a). In Chap. 6 we will focus on the characterization of supernova turbulence in terms of the basic supernova explosion parameters, namely the supernova rate and the feedback efficiency and investigate several related issues.

1.4 Outline of this thesis

The previous sections of this chapter attempted to show how processes such as turbulence and star formation in the ISM of galaxies are central to modern astrophysics. Despite all theoretical and numerical efforts, the actual situation concerning our understanding of the structure and dynamics of the ISM remains poor in many aspects (see Cox 2004 for pointing out to this painful but still encouraging reality). In the ISM, the interplay between turbulence, gravity, thermal processes, magnetic fields and cosmic rays determines the modes of molecular cloud and star formation (clustered versus isolated, fast versus slow), which in turn defines the global galactic properties. It is still a very challenging task to disentangle the cumulative/competitive effects of all physical processes if included at once in numerical simulations. We have taken the option of adding the different physical processes into our local three-dimensional numerical simulations on a one by one basis in order to assess their contributions to the ISM structure and dynamics on different scales.

In the next chapter, we shall present the basic equations of hydrodynamics, the code we have used, an algorithm to isolate and study condensations in the simulation box and the algorithm to drive *artificial* turbulence. Chap. 3 deals with gas instabilities relevant to our models, namely the thermal and gravitational instability. In Chap. 4, local, three dimensional simulations of the ISM are presented. These simulations are for a *decaying* turbulence and aim at answering questions like : does thermal instability drive turbulence ? what is the structure of the gas that is inherited from thermal instability ?.

H I maps derived from more realistic simulations of driven turbulence in the ISM including also heating and cooling and the self-gravity of the gas will be used in Chap. 5 in order to study a scenario in which the observed H I holes in many dwarf irregular galaxies may be the result of turbulent *sweeping* aided by thermal and gravitational instabilities. We also show how this approach can help identify the driving length-scale of turbulence in these galaxies. Our results show that turbulence in the ISM of a particular galaxy we have studied (Holmberg II) is most likely driven on large scales ($\simeq$ 6 kpc).

Finally, in Chap. 6 we use three-dimensional numerical simulations of supernova driven turbulence (at different rates) in the ISM, in order to investigate how much does the energy injected by supernova explosions in the ISM can be held accountable for the velocity dispersion profiles observed in most spiral galaxies. In those models, we vary the supernova rate, supernova feedback efficiency and the gas average density.

Chapter 2

Equations and Analysis

2.1 The hydrodynamics equations

The hydrodynamical equations are based on the description of the macroscopic properties of the gas. Gas particles can be described by a distribution function $f(\mathbf{x}, \mathbf{v}, \mathbf{t})$ which contains information about the position $\mathbf{x}$ and velocity $\mathbf{v}$ of each particle at a given time t. The variations in the positions and velocity and in time of the ensemble of particles can be described by the Boltzmann equations (for a detailed derivation from first principles, see e.g., Shu 1992; Shore 1992)

$$\frac{\partial f}{\partial t} + v_j \frac{\partial f}{\partial x_j} + \frac{\partial v}{\partial t}\frac{\partial f}{\partial v_j} = \left(\frac{\partial f}{\partial t}\right)_c . \tag{2.1}$$

The right hand side term is the *collisional* term. It acts as a source-sink term which describes the ensembles of particles scattered into or away from the phase space of the system. If the system is in full equilibrium, the *collisional* term cancels out and the scattering process conserves the total mass, the total momentum, the total angular momentum and, assuming that there are no internal degrees of freedom for the individual gas particles, the total kinetic energy. One method to derive the equations governing the evolution of each of these quantities (i.e., mass, momentum, energy) is to expand the Boltzmann equation into its velocity moments by multiplying it with functions of different order in $\mathbf{v}$ (i.e., by 1, $\mathbf{v}$, $\mathbf{v^2}$, etc) and integrating over the $\mathbf{v}-$space. At the 0th, 1st and 2nd order velocity orders, this leads to the mass conservation, momentum conservation and energy conservation equations, respectively

$$\frac{\partial \rho}{\partial t} + \nabla(\rho \mathbf{v}) = 0, \tag{2.2}$$

$$\frac{\partial \mathbf{v}}{\partial t} + \nabla\left(\frac{1}{2}\mathbf{v}^2\right) + (\nabla \times \mathbf{v}) \times \mathbf{v} = -\frac{1}{\rho}\nabla P - \nabla\phi, \tag{2.3}$$

$$\rho\left(\frac{\partial E}{\partial t} + \mathbf{v}\nabla E\right) = -P\nabla\mathbf{v}, \tag{2.4}$$

where ρ, v, P and E are the gas density, velocity, pressure, and total energy (kinetic + thermal + gravitational) and ϕ is the gravitational potential of the gas which, if taken into account, has to be added to the momentum equations at this zero order of approximating the Boltzmann equation. The gravitational potential is given by the Poisson equation

$$\Delta\phi = 4\pi G\rho, \tag{2.5}$$

where G is the gravitational constant. The above system of four equations with five variables needs to be complemented with a fifth relation which couples the pressure of the gas to its density and temperature i.e., the equation of state. The interstellar medium gas can be assimilated to an ideal gas with an equation of state of the form

$$P = \frac{k_b T}{\mu m_u}\rho, \tag{2.6}$$

where k_b is the Boltzmann constant, μ the mean molecular weight, and $m_u = 1.66 \times 10^{-24}$ g the atomic mass unit. μ is of the order 2.36 for a molecular hydrogen gas, 1.24 for a neutral atomic gas of solar composition, 0.5 for a pure hydrogen ionized gas and 0.66 for a hydrogen ionized gas with solar composition. In the case of an ideal gas, the specific internal energy e is connected to the gas pressure

$$e = \frac{P}{(\gamma - 1)\rho}, \tag{2.7}$$

where γ is the adiabatic index which is defined as the ratio of the heat capacities at constant volume and constant pressure and is related to the degrees of freedom of the gas particles f by

$$\gamma = \frac{2}{f} + 1 \tag{2.8}$$

for a diatomic gas $f = 5$ and $\gamma = 7/5$ whereas for a monoatomic gas $f = 3$, and thus, $\gamma = 5/3$.

The system of Equations 2.2-2.4 is written in an *Eulerian* description, in which the system of coordinates remains unchanged in time (e.g., fluxes of physical quantities through unchanged lengths, surfaces or volumes). Another approach is to follow the individual motion of the gas elements e.g., the *Lagrangian* description. It is possible to represent Eqs. 2.2-2.4 in the Lagrangian formalism by introducing the Lagrangian substantial derivative $D/Dt = \delta/\delta t + \mathbf{v}\nabla$. Another relevant point we ought to mention in this section is that the Equations 2.2-2.4 have been derived by neglecting the collisional term in Eq. 2.1 and thus are a zero order derivation of the fundamental equation and are known as the Euler equations. Considering a higher moment in v in deriving the momentum and energy equation will lead to the appearance of higher order terms such as the viscosity tensor in the momentum equation to describe the effect of the viscous force $\rho^{-1}\bar{\pi}$, the minus of the divergence of the conductive flux ∇F_{cond}=$\nabla\kappa\nabla T$ and viscous dissipation $1/2\mu_v D^2$ where $\pi = \mu_v|D|^2$. The Euler equations with the additional terms are better known as the Navier-Stokes equations.

2.2 The code

ZEUS-3D (Stone and Norman 1992a,b) is a well tested Eulerian time-explicit code that adopts a finite-differences scheme. The code is three-dimensional but symmetries can be used to reduce the grids to two or one dimension(s). The code can solve on a Cartesian, cylindrical or spherical grid the following equations

$$\frac{\partial \rho}{\partial t} + \nabla(\rho \mathbf{v}) = 0, \tag{2.9}$$

$$\frac{\partial (\rho \mathbf{v})}{\partial t} + \nabla(\rho \mathbf{v}) = -\nabla P \tag{2.10}$$

$$\frac{\partial e}{\partial t} + \nabla(\rho \mathbf{v}) = -P \nabla \mathbf{v}. \tag{2.11}$$

In the magneto-hydrodynamical version, the code also solves, in the limit of the low resistivity regime, the Faraday induction equation which describes the evolution of the magnetic field :

$$\frac{\partial \mathbf{B}}{\partial t} = \nabla \times (\mathbf{v} \times \mathbf{B}). \tag{2.12}$$

With the above described set of equations, the code solves the temporal evolution of the pressure ρ, velocity $\mathbf{v}$, and the internal energy of the fluid (i.e., Eq. 2.7) for a single fluid on a defined grid. External forces can be added and additional terms have to be added accordingly to the equations. If the self-gravity of the gas is considered, a gravitational force term $-\rho \nabla \phi$ has to be added to Eq. 2.10 (right hand side, RHS) and in the case when Eq. 2.12 is explicitly solved, a Lorentz force term $\mathbf{j} \times \mathbf{B}$ need to be added to Eq. 2.10 (RHS), where $\mathbf{j}$ is the current density. The code, which does not include a natural viscosity term, incorporates an artificial von Neumann-Richtmyer viscosity (von Neumann and Richtmyer 1950) which helps smear out the discontinuity caused by shocks but on scales larger than those on which natural viscosity acts (i.e., on the grid scale). The artificial viscosity, described by the viscous stress tensor $\mathbf{Q}$, adds the terms $-\nabla \mathbf{Q}$ and $-\mathbf{Q}.\nabla \mathbf{v}$ to the momentum and energy equations (RHS), respectively.

Eqs. 2.9-2.12 are discretized in the code on a staggered mesh. The scalar quantities such as ρ, e, and the gravitational potential ϕ are defined at the center of each cell and the vector quantities are defined at the cells faces. This scheme guarantees global mass conservation up to the machine accuracy by computing the fluxes through each cell wall and then using these fluxes to update adjacent cells. The numerical diffusion, due to the discretization, which can affect the local conservation is treated by employing the Consistent Transport (CT) scheme (Norman et al. 1980) and the quantities that are advected are the density ρ, the specific energy e/ρ, and specific momenta p/ρ. The advection uses a van Leer second order scheme (van Leer 1977) with an upwind scheme (Godunov 1959). The code assures monotonicity (Hawley et al. 1984) which means that if a quantity $L = L(\mathbf{x}, t)$ is increasing (or decreasing) before the advection step, it has to maintain that trend after the advection. Otherwise new extremas are introduced into the flow.

In order to compute the gravitational potential, one needs to solve the Poisson equation

$$\Delta \phi = 4\pi G \rho. \tag{2.13}$$

An efficient method to solve Eq. 2.13 is to use an FFT solver. In the Fourier space, the convolution integral between the density and the grid Green's-function can then be written as a multiplication. We use a ZEUS adapted version of such solver following an implementation by Burkert and Bodenheimer (1993), which is derived from Press et al. (1992).

As ZEUS-3D is a time explicit code, it has to limit the time step used to evolve the dynamical equations in order to satisfy the Courant-Friedrichs-Lewy (CFL) stability condition. Physically, this condition corresponds to limiting the distance that information can travel in one time step (via a wave or fluid motions) to be smaller than one grid zone. The largest time step possible should be chosen such that every cell locally fulfills the CFL condition. In one dimension the condition should be

$$\Delta t \leq min(\Delta x)/(|v_x| + c_s), \tag{2.14}$$

where v_x is the one dimensional local fluid velocity, c_s the local adiabatic sound speed, and the minimum is taken over all grids. In ZEUS-3D, Stone and Norman (1992a) calculate the CFL time step with

$$\Delta t = C_0/[max(\delta t_1^{-2} + \delta t_2^{-2} + \delta t_3^{-2} + \delta t_4^{-2})]^{1/2}, \tag{2.15}$$

where the maximum is taken over all cells. C_0 is the *Courant number* and like all time-explicit codes is assigned a value of 0.5. δt_1 arises from the ratio of the maximum cell size to the sound speed, δt_2 from the artifical viscosity, δt_3 from comoving grids (if existent) and δt_4 from the Alfvén velocity $v_A = |\mathbf{B}|/\sqrt{\mu_0 \rho}$, where μ_0 is the magnetic resistivity.

ZEUS-3D has been mainly developed by Michael Norman and James Stone and is publicly available from the National Center for Supercomputer Applications (NCSA) at the University of Urbanna-Champaign, Illinois. We have performed our simulations with ZEUS-3D on an SGI Origin 2000 located at the Rechnenzentrum of the Max-Planck-Gesellschaft (RZG) in Garching, Germany.

2.3 Clump finding and Virial analysis

In some sections of this thesis, we shall discuss the structural and kinematical properties of condensations (i.e., clouds or clumps) that form when physical processes are added to the simulation such are self-gravity or the effect of a different parameterization of other processes such as cooling. For that purpose, an algorithm has to be used in order to isolate condensations in the medium. We use an IDL implementation of the CLUMPFIND algorithm described in Williams et al. (1994). The code is based on a density criterion. It selects the cells which have densities larger than a defined density threshold, performing a friends-of-friends test to search for geometrically connected cells which fulfill the selection criterion. The positions of the cells forming a single cloud are kept in a separate list and mathematical operations can then be performed on each ensemble of cells which form a condensation.

We developed this algoritm in order to calculate the following quantities : The surface S, the volume V, the mass M, the average density $\bar{\rho}$, the position of the center of mass (x_c, y_c, z_c), the three components of the center of mass velocity (v_{cx}, v_{cy}, v_{cz}) and center of mass velocity $v_c = \sqrt{v_{cx}^2 + v_{cy}^2 + v_{cz}^2}$, the kinetic energy of the condensation E_c, the velocity dispersion in the condensation $v_{rms} = \sqrt{(1/N_c)\sum_{i=1}^{N_c}(|v_i|^2 - \bar{v}^2)}$ where $\bar{v}$ is the average of the velocity modulus of the N_c cells found in the condensation, the internal energy E_{th}, the characteristic sound speed $c_s = \sqrt{2\ E_{th}/3\bar{\rho}}$, the characteristic Mach number $Ma = v_{rms}/c_s$, the angular

momentum $|\mathbf{J}|$ and the specific angular momentum $J_M = |\mathbf{J}|/M$ and the divergence of the velocity $\nabla\mathbf{v}$.

A negative velocity divergence associated with a condensation is only indicative of the existence of convergent flows and not of the existence of a gravitationally bound structure. A very useful tool for describing the balance between all the physical agents in a condensation is the virial theorem. Following McKee and Zweibel (1992), Ballesteros-Paredes et al. (1999b) and Shadmehri et al. (2002), we perform a virial analysis (in the Eulerian form) on each of the selected condensations. For that purpose we need to evaluate the terms which appear in the following equation

$$\frac{1}{2}\ddot{I}_E = 2\left(E_{th} + E_c + E_B - \mathcal{T}_{th} - \mathcal{T}_c - \mathcal{T}_B\right) + \mathcal{W} - \frac{1}{2}\frac{d\Phi}{dt}, \tag{2.16}$$

where $I_E = \int_V \rho r^2 dV$ is the moment of inertia of the cloud, where r represents the position of each cell; $E_{th} = \frac{3}{2}\int_V P dV$, the above mentioned thermal energy, with P being the thermal pressure (i.e., 2.7); $E_c = \int_V m_i v_i^2 dV$ is the above mentioned kinetic energy; $E_B = \frac{1}{8\pi}\int_V B^2 dV$ is the magnetic energy; $\mathcal{T}_{th} = \frac{1}{2}\oint_S x_i P \hat{n}_i dS$ is the thermal energy surface term; $\mathcal{T}_c = \frac{1}{2}\oint_S x_i \rho v_i v_j \hat{n}_j dS$ is the kinetic energy surface term; $\mathcal{T}_B = \oint_S x_i T_{ij} \hat{n}_j dS$ the magnetic energy surface term, where T_{ij} is the Maxwell stress tensor; $\mathcal{W} = \int_V \rho x_i g_i dV$ is the gravitational term (not equal to the volume gravitational energy), where g is the local gravitational potential gradient and $\Phi = \oint_S \rho x^2 u_i \hat{n}_i dS$ is the flux of moment of inertia through the surface of the cloud. In our algorithm, integrals are replaced by sums running over the N_c cells that define each condensation. The energy surface terms can be regarded as fluxes of energies across the surface. For example, in the case of the surface kinetic energy, it can be interpreted in terms of a combination of ram pressure plus kinetic stresses (Ballesteros-Paredes et al. 1999b). Shadmehri et al. (2002) showed, based on the analysis of three-dimensional isothermal MHD simulations, that the temporal terms (left hand term and last term on the right hand side) are equal. We have limited ourselves to a 'snapshot' evaluation of the virial theorem, thus assuming a non temporal dependence which is obviously a simplification despite the result of Shadmehri et al. (2002). Additionally, an evaluation of the temporal terms is only meaningful if the time lap dt is quite small in order to be sure that the analysis takes into account the same cloud. However it is justified to believe that if gas is in the process of condensing (or dispersing), the two temporal quantities will evolve with the same tendency (without being necessarily equal), thus unless a violent process takes place like a rebound of the matter on the condensation core, the comparison of the non temporal quantities (volume+surface energies versus gravity) would describe if a cloud is contracting or dispersing without any information about the acceleration of the contraction or dispersion process. We also drop the magnetic terms as we do not account for the magnetic field in our simulations. Eq. 2.16 is then reduced to (at the virial equilibrium)

$$\mathcal{W} = 2\left(E_{th} + E_c - \tau_{th} - \tau_c\right). \tag{2.17}$$

Another simplification we had to perform affects the calculation of the characteristic radius R of each condensation. As the condensations have complex geometrical structures, we have used the conservative approach of considering the characteristic radius of a condensation to be the cubic root of the volume V.

2.4 Generating artificial turbulence

In § 1.2.2, we have presented some of the most relevant energy injection mechanisms into the ISM. Including these physical processes into numerical simulations of the ISM is necessary to bring the simulations to better match the observations. However, this is a significant numerical challenge as these physical processes span over a large dynamical range. On the other hand, many of these physical processes which are responsible for energy injection into the ISM cannot be treated fully self-consistently and have to rely on parameterizations. The multiple parameters and the ad-hoc schemes used to treat physical processes such as star formation have lead astronomers to seek a simpler approach to the process of energy injection into the ISM. One way, which we have used in some of our simulations, makes abstraction on the nature of the energy driver and characterizes it with only two parameters, its energy injection scale L_{inj} which in Fourier space is represented by a wave vector $k_{inj} = 2\pi/L_{inj}$, and its energy injection rate. We follow the prescription of Mac Low (1999) for generating the initial velocity fields and for driving turbulence. We recall here some of the basic aspects of the method. The velocity perturbations are drawn from a Gaussian random field specified by its power spectrum in the Fourier space. In a narrow wave number band $k - 1 < \mathbf{k} < k$, we select an amplitude from a Gaussian distribution normalized to unity and a random phase between 0 and 2π. The components of the velocity field in real space, obtained after a Fourier transform, have to be multiplied by an amplitude in order to get the desired *rms* velocity (i.e., initial Mach number or *strength* of the turbulence). For maintaining this 'artificially' driven turbulence, the energy injection rate will be equal to the energy dissipation rate as to keep the kinetic energy at a pseudo constant value. We use a kinetic energy dissipation rate, following the estimate of Mac Low (1999), which writes

$$\dot{E}_c \simeq \frac{0.21}{\pi} M_{tot} k_{inj} v_{rms}^3, \tag{2.18}$$

where M_{tot} is the total mass of the considered system and v_{rms} the velocity field *rms* value at which the turbulence need to be maintained. With the energy injection rate defined in Eq. 2.18, the kinetic energy to be injected at each time step Δt is $\Delta E_c = \dot{E}_c \Delta t$. The amplitude of the velocity field and of the three velocity components is derived in the following way : One assumes that at the kinematical equilibrium, locally

$$E_c + \delta E_c \simeq \frac{1}{2} m_{ijk} (\mathbf{v_{ijk}} + \delta \mathbf{v_{ijk}})^{\mathbf{2}}, \tag{2.19}$$

where $\mathbf{v_{ijk}}$ is the local velocity field, $\delta \mathbf{v_{ijk}}$ the local perturbation to the velocity field chosen to be $A\mathbf{u_{ijk}}$ where A is the amplitude of the perturbation and $\mathbf{u_{ijk}}$ and m_{ijk} the unit vectors and the local mass value, respectively. Re-injecting the latter expression in Eq. 2.19, developing the right hand side, and summing up over the number of cells in each direction (assumed to be n in all three direction), one obtains a quadratic equation in the amplitude of the perturbations A

$$\delta E_c = \frac{1}{2} \sum_{i,j,k=1}^{n} m_{ijk} (A \mathbf{v_{ijk}} \mathbf{u_{ijk}} + A^2 \mathbf{u_{ijk}}^2). \tag{2.20}$$

The amplitude A is then assigned the value of the larger root of Eq. 2.20

2.5 Scalings

Solving the hydrodynamical equations in the astronomical context in physical units can lead to a loss of accuracy because of the large numbers that ought to be used. Some physical constants, particularly when used with large exponents can lead to over/underflows in the floating-point representation. An alternative is to use dimensionless units that implicitly represent the physical units via predefined conversion coefficients. The values of the most representative variables are sought to be of the order of 1 in the dimensionless units. We have chosen the building blocks of our scaling system to be the number density n, the temperature T and the gravitational constant G. The values assigned to each of those three dimensionless variable are

$$1\ \hat{T}_4\ [K] = 1, \tag{2.21}$$

$$1\ \hat{n}_4\ [m^{-3}] = 50, \tag{2.22}$$

$$G = 1, \tag{2.23}$$

where the scalings are defined in physical units of 10^4. All other physical quantities can be written in terms of the above defined variables. For example, using the definition of the sound speed, we can obtain a scaling for the velocity which is $1\ \hat{v}$ [m s^{-1}]$= \left(\frac{\gamma}{\mu}\right)^{-1/2} \left(\frac{k_b T_4}{m_H}\right)^{1/2}$, where k_b is the Boltzmann constant and m_H the hydrogen atom mass. The scaling for time can be obtained from the expression of the free fall time and a dimensionless time unit will carry a physical value of $1\ \hat{t}$ [s]$=\frac{1}{\mu^{1/2}} 0.2993 \times 10^{17} n_4^{-1/2}$. The rest of the relevant physical quantities are derived in a similar fashion and are listed in Appendix A.1.

Chapter 3

Gas instabilities in the interstellar medium

Interstellar gas can be affected by several instabilities and perturbations which cumulative and/or competitive effects shape the interstellar medium structure and dynamics. For a more complete review on the zoo of fluid instabilities, we refer the interested reader to the excellent textbooks of Chandrasekhar (1961) and Shu (1992). In this chapter we shall discuss in some detail two instabilities, namely the thermal and gravitational instabilities which play an important role in the interstellar medium. In each case the criterion for instability shall be derived and the effect of stabilizing forces briefly discussed. The reader who is familiar with these instabilities might decide to skip this chapter and move to the next chapter in which three-dimensional numerical simulations including turbulence, cooling, heating and the self-gravity of the gas are presented and discussed.

3.1 Thermal instability

Thermal instability is a process which takes place in a medium when the local balance of cooling and heating is perturbed such that the system is unable to return to it's equilibrium configuration. As an over-dense region cools faster than the surrounding medium, a pressure gradient is created which drives more matter onto the condensation, which in turn becomes more dense and cools even faster, thereby leading to a runaway situation. The linear theory of thermal instability (TI) has been developed by several authors, notably by Field (1965) and Field et al. (1969). Field (1965) derived the instability criterion for a uniform medium of initial density ρ and temperature T and which is perturbed around those values and is subject to cooling and heating processes quantified by the heat function term $\mathcal{L}= (\Lambda - \Gamma)/\rho$, where Γ and Λ are the heating and cooling rates, respectively. Field (1965) found a criterion which can be applied to isochoric (see also Parker 1953) and isobaric regimes. In the two different regimes, the criterion is, respectively

$$\left(\frac{\partial \mathcal{L}}{\partial T}\right)_{\rho} < 0, \tag{3.1}$$

$$\left(\frac{\partial \mathcal{L}}{\partial T}\right)_{P} = \left(\frac{\partial \mathcal{L}}{\partial T}\right)_{\rho} - \frac{\rho}{T}\left(\frac{\partial \mathcal{L}}{\partial \rho}\right)_{T} < 0. \tag{3.2}$$

Whereas the evolution of the instability in the isochoric regime is of little relevance for astronomical applications such as molecular cloud formation in the diffuse interstellar gas as the density enhancement due to the thermal instability remains in the linear regime (i.e., very small growth rate) by the time temperature has reached it's minimum value, and in that case the pressure gradient can be inverted, thus erasing the condensation (see Burkert and Lin 2000 for a time dependent one-dimensional investigation of the development of the thermal instability in the isochoric regime). More interesting, is the evolution of the thermal instability in the isobaric regime, in which small density perturbations can be enhanced to large values (Burkert and Lin 2000). In the following, we reproduce a derivation of the criterion for thermal instability. A more detailed description is presented in Field (1965) and Elmegreen (1992). In a first approach, the effects of magnetic fields, rotation, gravity, thermal conduction, viscosity and radiation (i.e., this assumes the medium is optically thin) are neglected. We start with the basic gas-dynamical equations of continuity, motion and energy

$$\frac{D\rho}{Dt} = -\rho \, \nabla \cdot \mathbf{v}, \tag{3.3}$$

$$\rho \, \frac{Dv}{Dt} = -\nabla P, \tag{3.4}$$

$$\frac{DP}{Dt} = \frac{\gamma \, P}{\rho} \, \frac{D\rho}{Dt} + (\gamma - 1)(\Gamma - \Lambda), \tag{3.5}$$

where $D/Dt = \partial/\partial t + \mathbf{v} \cdot \nabla$. We also assume an equation of state for a perfect gas which writes

$$P = \rho \, c_s^2, \tag{3.6}$$

where c_s is the thermal sound speed. Equilibrium values are $\mathbf{v}$=0, ρ=constant and P=constant. If the thermal equilibrium is perturbed, the new values near equilibrium of the velocity field, density, and pressure are $\mathbf{v} + \hat{\mathbf{v}}$, $\rho + \hat{\rho}$ and $P + \hat{P}$, respectively. It is a straight forward task to inject the near-equilibrium values in the system of equations 3.3-3.6 and separate the zero order, first order and second order terms. A system of equations with only first order quantities can be obtained. It writes

$$\frac{\partial \hat{\rho}}{\partial t} = -\rho \, \nabla \cdot \mathbf{v}, \tag{3.7}$$

$$\rho \, \frac{\partial \hat{v}}{\partial t} = -\nabla \hat{P}, \tag{3.8}$$

$$\frac{\partial \hat{P}}{\partial t} = \gamma c_s^2 \frac{\partial \hat{\rho}}{\partial t} + (\gamma - 1)(\hat{\Gamma} - \hat{\Lambda}), \tag{3.9}$$

$$\hat{P} = \hat{\rho} c_s^2 + 2\rho c_s \hat{c_s}. \tag{3.10}$$

These equations have constant coefficients and therefore exponential solutions in space and time of the form $e^{(wt + i\mathbf{kx})}$, where $\mathbf{k}$ is the wave number and w the growth rate. It is easy to differentiate the equations with the adopted solution in order to obtain a linear set of equations. Combining Eq. 3.7 and Eq. 3.8 yields the following dispersion relation

$$w^2 = -k^2 \frac{\hat{P}}{\hat{\rho}}. \tag{3.11}$$

The dispersion relation indicates that thermal instability takes place whenever $\hat{P}/\hat{\rho} < 0$. $\hat{P}/\hat{\rho}$ can be written in terms of the heat function coefficients. If the medium is in thermal equilibrium $\Lambda = \Gamma = \Lambda_c$. Once the thermal equilibrium is perturbed, these quantities will take slightly different value and can be described by $\Gamma \propto \rho^r c_s^s$ and $\Lambda \propto \rho^l c_s^m$ for the heating and cooling rates, respectively. The difference between cooling and heating near equilibrium is

$$\hat{\Gamma} - \hat{\Lambda} = \Lambda_c \left((r-l)\frac{\hat{\rho}}{\rho} + (s-m)\frac{\hat{c_s}}{c_s} \right). \tag{3.12}$$

One can use $\hat{c_s}/c_s = 1/2\ (\hat{P}/P - \hat{\rho}/\rho)$ (Eq. 3.10) and replace it in Eq. 3.12 in order to obtain $\hat{P}/\hat{\rho}$

$$\frac{\hat{P}}{\hat{\rho}} = \gamma c_s^2 \left(\frac{w - w_c(2l + s - m - 2r)}{w + \gamma w_c(m - s)} \right), \tag{3.13}$$

where $w_c = (\gamma - 1)\Lambda_c / 2\gamma P$ has the dimensions of a cooling rate. $\hat{P}/\hat{\rho}$ is negative either when $(2l + s - m - 2r) > 0$ or $(m - s) < 0$. The most important case is the first one which involves density variations at nearly constant pressure (isobaric regime). Therefore the instability criterion $\hat{P}/\hat{\rho}$ is reduced to the following criterion

$$2l - m > 2r - s. \tag{3.14}$$

One should keep in mind that the coefficients m, l, r and s are themselves functions of temperature and density and might change locally with time if realistic cooling/heating functions are considered. Therefore the TI proceeds locally until the criterion in Eq. 3.14 is not valid anymore. In numerical simulations, it is possible to force thermal equilibrium by fixing minimum and maximum values for the temperature, thus not allowing cold/warm gas to cool/heat any further.

3.1.1 The dynamical effect of thermal instability

Burkert and Lin (2000) derived the expression for the velocity perturbation v evolution in the linear phase in the one-dimensional analysis. Using a simple cooling curve of the form $\Lambda(T) = \Lambda_0 T^\beta$, the expression they found is

$$|v| = \left| \frac{2 - \beta}{\Gamma_g (1 - (1 - \tau))} \frac{\delta\rho}{\rho_0} \right|, \tag{3.15}$$

where Γ_g is the adiabatic index and τ represents the time variable in units of the crossing time, and $\delta\rho/\rho_0$ the ratio of the perturbed density to the initial density. The growth of the velocity perturbations in the linear regime as implied in Eq. 3.15 seems to be dictated principally by the growth of the density perturbations. Fig. 2 in the paper of Burkert and Lin (2000) show that v can grow within one crossing time by ~ 3 orders of magnitude. However, it is not clear from their analysis what is the physical value of the velocity after one crossing time nor how does it compare to the thermal sound speed. In their two-dimensional simulations, Piontek

and Ostriker (2004) focused on the evolution of a velocity field purely driven by thermal instability. They found the velocity dispersions to be all subsonic in the warm, unstable and cold phases of the ISM with values of 0.25 km s^{-1}, 0.35 km s^{-1} and 0.15 km s^{-1}, respectively. This is an order of magnitude or more below the observed values in the ISM. In Chap. 4, we will address this issue in the context of our three-dimensional numerical simulations.

3.1.2 The effect of thermal conduction

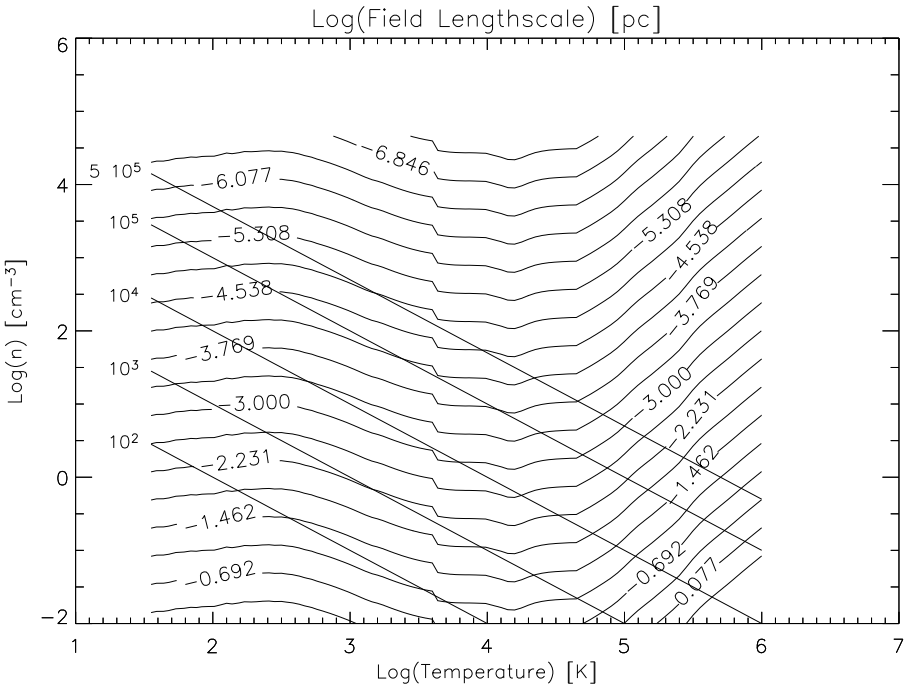

Figure 3.1: The Field length-scale λ_f (in pc) as a function of temperature and density. The diagonal lines represent isobars in units of the Boltzmann constant k_b. The values of the isobars are shown on the left side of the plot from $5 \times 10^5 k_b$ down to $10^2 k_b$. Details about the adopted cooling functions can be found in the text.

In the presence of a temperature gradient ∇T, a flow of heat will appear, transporting the heat from the hotter regions to the colder ones. Heat is transported by electrons characterized by a mean free path for electron energy exchange $\lambda_e(T/K)$ (cm$^{-3}/n$) cm (Cowie and McKee 1977) (n is the number density), and which has to be shorter than the temperature scale height $\sim \lambda/\delta T/T$, where λ is the size of the density perturbation for thermal conduction to be effective (Cowie and McKee 1977, Burkert and Lin 2000). Field (1965) was the first to point out that thermal instability can be stabilized by thermal conduction. The effects of thermal conduction on the fate of cold clouds embedded in a hot stable or unstable medium in steady state models (i.e., steady state evaporation of the cloud) has been discussed by several authors (Zel'dovich and Pikel'ner 1969; Penston and Brown 1970; Graham and Langer 1973; Cowie and McKee 1977; McKee and Cowie 1977; Balbus 1985 and McKee and Begelman 1990). The latter authors found that a density perturbation can only grow if its length-scale is larger

than the characteristic length-scale of thermal conduction, known as the Field length-scale λ_f (Field 1965). This result has been confirmed in one-dimensional time dependent models by Ferrara and Shchekinov (1993) and Burkert and Lin (2000). λ_f is defined by the condition that the cooling ($n^2\Lambda$) or heating rate ($n\Gamma$) be comparable to the conductive energy exchange rate ($\kappa(T)\ T/\lambda_f$) on this scale, where $\kappa(T)$ is the thermal conduction coefficient. Assuming cooling is dominant, λ_f writes

$$\lambda_f = \left(\frac{k(T)\ T}{n^2\Lambda}\right)^{1/2}. \tag{3.16}$$

Fig. 3.1 displays the dependence of λ_f on temperature and density. The value of λ_f is given in pc. We used $\kappa(T) = 2.5 \times 10^3 T^{1/2}$ ergs cm^{-1} K^{-1} s^{-1} for $T \leq 4.47 \times 10^4$ K and $\kappa(T) = 1.24 \times 10^{-6} T^{5/2}$ ergs cm^{-1} K^{-1} s^{-1} for $T > 4.47 \times 10^4$ K (Parker 1953; Spitzer 1962). The adopted cooling function combines the collisional equilibrium ionization cooling curve of Dalgarno and McCray (1972) and the H_2 molecule vibrational and rotational lines cooling (Lepp and Shull 1983; Smith and Rosen 2003) which starts to have a non-negligible contribution to the cooling rate for number densities $n \geq 10^4$ cm^{-3}. The values of λ_f in Fig. 3.1 show the resolution requirement numerical simulations have to afford if they were to accurately capture the effects of thermal conduction and its stabilizing effect on thermal instability. At low temperatures and high densities, this resolution requirement is severe. Already, for a number density of $\sim 10^3$ cm^{-3} and a temperature of $\sim T = 100$ K, the resolution requirement is $\sim 10^{-5}$ pc. Numerical simulations intended to study the large scale interstellar medium (~ 1 kpc) will need to have a spatial dynamical range of 10^8. This is extremely hard to achieve, even for the most competitive of the currently available hydrodynamical codes and computational hardware. The best resolutions achieved up to date are in the range $1024^3 - 4096^3$ (Kaneda et al. 2003; Haugen and Brandenburg 2004). Such extreme resolutions might be achieved by using Adaptative Mesh Refinement codes (AMR) such as FLASH (http://flash.uchicago.edu/website/home). However, most of the AMR codes which are currently publicly available have a density-refinement scheme implemented (i.e., refinement is performed in regions of increasing density). For studies of gas instabilities and turbulence, the refinement scheme must be more subtile, allowing for daughter grids to be created in regions of decreasing energy and/or increasing momentum.

In our simulations with the ZEUS code, calculating thermal conduction in simulations of the large scale ISM with medium resolutions of 128^3 (i.e., as in Chaps. 5 and 6) is not relevant for the global dynamics of the ISM. We have initiated a work (described briefly in the last chapter) in which we intend to study the detailed fragmentation in a post-shock region on scales of $0.1 - 1$ pc with high resolution two-dimensional numerical simulations, and in this particular problem thermal conduction will be included.

3.1.3 The effect of magnetic fields

Chandran and Cowley (1998) studied the effects of magnetic fields on thermal conduction. As the magnetically resistive scale at which magnetic fields vanish is smaller than the electron mean free path λ_e, tangled magnetic fields can develop in the medium on scales $l_B < \lambda_e$ (Chandran and Cowley 1998). When the gyroradius

$$a = \frac{v_T \; m_e \; c}{e \; B} \sim 2.2 \times 10^8 \sqrt{\frac{T}{10^8 K}} \left(\frac{\mu G}{B}\right) cm \tag{3.17}$$

of thermal electrons with typical velocities $v_T = \sqrt{k_b T/m_e}$ is much smaller than $l_B < \lambda_e$, the magnetic field controls the trajectory of individual electrons. This condition is satisfied in many astrophysical plasmas even if the magnetic pressure (i.e., $\propto B^2$) is too weak to influence the global dynamics. If a is small compared to the scale of the density perturbation λ, heat can still be conducted is a similar way when no magnetic fields are present, but with a reduced thermal conduction coefficient κ_B, which is a fraction of the classical value κ (Chandran and Cowley 1998)

$$\kappa_B \sim \frac{0.1}{ln(l_B/a)} \; \kappa. \tag{3.18}$$

Burkert and Lin (2000) derived an estimate for the value of $ln(l_B/a)$ and found the following relation

$$ln\left(\frac{l_B}{a}\right) = -3.1 + \left(\frac{B}{B_T}\right) + 2 \; ln\left(\frac{T}{K}\right) - 0.5 \; ln\left(\frac{n}{cm^{-3}}\right) + \left(\frac{l_B}{\lambda_e}\right), \tag{3.19}$$

where B_T is the value of the magnetic field at the equipartition of thermal and magnetic energies. For weak fields $B \sim 0.01 B_T$ and $l_B \sim \lambda_e$, Eq. 3.18 yields $ln(l_B/a) \geq 10$. This means that the thermal conduction coefficient κ_B would be reduced by two order of magnitudes from its classical value κ, and the length scale of thermal conduction by one order of magnitude. Hence, the presence of magnetic fields can suppress thermal conduction, enabling thermal instability to operate on smaller scales that would normally be inhibited by thermal conduction. The arguments presented in Burkert and Lin (2000) might be even more relevant if processes such as magnetic reconnection occur, which will assemble the small scale magnetic fields into larger ones and help lower the ratio B/B_T, thus reducing further more the value of κ_B. On the other hand, Eq. 3.17 and Eq. 3.18 give an estimate of κ_B for one value of the temperature and density. A more complete picture can only be obtained if the time variations of all the local variables is accounted for.

3.2 Gravitational instability

In a similar fashion to what have been presented in the previous section where we analyzed the stability of a gaseous system which is subject to energy perturbations, a usual method of describing the stability of a self-gravitating gas is to perturb the gravity field and investigate under which conditions the induced density perturbation might grow. Jeans (1902), derived the instability criterion for an isothermal, infinite, homogeneous, and self-gravitating medium. He did not consider any turbulent motion to be initially present in the medium. In this problem, the energy equation (Eq. 3.5) can be dropped (i.e., gas is isothermal) and the Poisson equation linking the gravitational potential to the density field (Eq. 3.20) has to be considered

$$\Delta\phi = 4\pi G\rho. \tag{3.20}$$

The equation of motion (Eq. 3.4) should be modified in order to include a gravitational force term $\nabla\phi$. We can again suppose that the equilibrium values are $\mathbf{v}$=0, ρ = *constant* and

$P = constant$. We also assume that $\phi = constant$. The perturbed quantities are, to first order, $\mathbf{v}+\hat{\mathbf{v}}$, $\rho+\hat{\rho}$, $\phi+\hat{\phi}$ and $P+\hat{P}$ where $\hat{P} = c_s^2\hat{\rho}$. It is possible to obtain a set of linearized equations including only first order terms. The continuity equation is the same as Eq. 3.7. The other equations are

$$\rho \frac{\delta\hat{v}}{\delta t} = -\nabla\hat{P} - \nabla\hat{\phi}, \tag{3.21}$$

$$\Delta\hat{\phi} = 4\pi G\hat{\rho}, \tag{3.22}$$

Eq. 3.21 which describes the relationship between the perturbed density and perturbed potential assumes that the initial value of the potential is $\phi = 0$ (Binney and Tremaine 1987). This is done to avoid the conflict between Eq. 3.15 and $\nabla\phi = 0$ with the assumed initial conditions. The other non desirable alternative is to consider that the initial density is $\rho = 0$. Taking the time derivative of Eq. 3.20, the divergence of Eq. 3.21, and using Eq. 3.7 leads to a wave equation for the density perturbation $\hat{\rho}$ (Binney and Tremaine 1987). Adopting the same family of solutions as in the previous section leads to the following dispersion relation

$$w^2 = c_s^2k^2 - 4\pi G\rho. \tag{3.23}$$

Hence, the system is unstable when the perturbation has a wave number k such that

$$k < k_J = \sqrt{\left(\frac{4\pi G\rho}{c_s^2}\right)}, \tag{3.24}$$

where k_J is the Jeans wave number. In terms of wavelength, a perturbation is unstable whenever it is larger than λ_J, where $\lambda_J = 2\pi/k_J$ is the Jeans wavelength. By introducing the geometry of the density perturbation, the Jeans criterion can be written in terms of a mass limit for instability to occur. Any mass M which is larger than the Jeans mass M_J

$$M > M_J = \left(\frac{\pi}{G}\right)^{3/2} \rho^{-1/2}c_s^2, \tag{3.25}$$

will collapse. M_J is the mass found inside the three-dimensional structure defined by the Jeans length scale, and in the case of Eq. 3.24 is the mass found initially inside a box of side λ_J. Alternatively M_J can be assumed to be the mass present inside a sphere of radius λ_J and easily calculated using that assumption (Binney and Tremaine 1987). It is worth keeping in mind that the Jeans criterion for gravitational instability sets an idealized picture of the gravitational collapse problem. There are other ways of assessing the question if a three-dimensional condensation of a given non-trivial geometrical structure is undergoing gravitational collapse. One of these methods is to look at the detailed virial balance of the considered objects in order to see if the gravitational energy term dominates the other energy terms which act to disperse the condensation. This has been presented in § 2.3 and will be applied to our three-dimensional numerical simulations. Once a runaway collapse sets in as it might be the case in a dense pre-stellar core, the effects of gravitational instability are very difficult to counter balance. The collapse is slowed down, but not stopped, when the opacity increases and the equation of state becomes adiabatic at densities of $n(H_2) \approx 10^{10}$ cm^{-3}. If temperature reaches values of ≈ 2000 K, the H_2 begin to dissociate leading to a second core contraction. If all H_2 molecules are dissociated, temperature rises sharply and the pressure gradient my become again able to halt the collapse (Masunaga et al. 1998; Masunaga and

Inutsuka 2000; Wuchterl and Klessen 2001; Wuchterl and Tscharnuter 2003), otherwise it would lead ultimately to the formation of (a) star(s) (i.e., start of nuclear fusion).

Chapter 4

A two phase model of the ISM

4.1 Introduction

Thermal instability has been traditionally considered as an important agent of structure formation in the ISM. Burkert and Lin (2000) performed a linear perturbation analysis of TI and studied numerically under which condition the transition from the linear to the non-linear regime occurs. Sánchez-Salcedo et al. (2002), used high resolution 1D simulations to study the behavior of TI in the presence of forced flows. Koyama and Inutsuka (2000, 2002) have investigated with 1D and 2D simulations which include detailed cooling, heating and chemistry, the propagation of shocks in the warm neutral medium (WNM) and cold neutral medium (CNM) and the development of TI in the post-shock region. Kritsuk and Norman (2002a,b) showed, using three-dimensional simulations, that a time fluctuating background heating supports turbulence in a multiphase ISM. Vázquez-Semadeni et al. (2000a) and Gazol et al. (2001) used local two-dimensional numerical simulations to investigate TI in the ISM on a scale similar to ours (1 kpc). They focused on the segregation of the medium into two distinct gaseous phases. A major success of their model is that they were able to reproduce a mass fraction of the unstable gas which is in good agreement with the observations (Heiles 2001). More recently, two-dimensional simulations where performed by Piontek and Ostriker (2004) which focused on the evolution of a velocity field purely driven by thermal instability. They found the velocity dispersions to be all subsonic in the warm, unstable and cold phases of the ISM with values of 0.25 km s^{-1}, 0.35 km s^{-1} and 0.15 km s^{-1}, respectively. This is an order of magnitude below the observed values in the ISM.

In this chapter, we investigate the role played by TI in the ISM and its contribution to the processes of molecular cloud formation and turbulence driving. We discuss the properties and the evolution of a two phase medium based on three-dimensional simulations we have performed in order to evaluate the TI's role on structure formation and the dynamics of the ISM. The set of simulations presented in this chapter are for a decaying turbulence, that is, the medium contains initially a certain amount of kinetic energy in the form of random motions and is allowed to evolve in time without any further injection of additional turbulence. The aim of such an approach is to analyze the development of TI directly in the non-linear regime to see if TI can generate a self-sustained turbulence in the ISM and be able to compare the structures and dynamics of a thermally unstable medium to more idealized simulations (e.g. isothermal simulations). Simulations with and without the effect of the gas self-gravity are

considered. We select a model with a particular set of parameters and where TI is found to be efficient and analyze in detail its global properties as well as the properties of the condensations which are formed as a result of TI. In contrast, the next chapter will deal with simulations where TI occurs in a medium characterized by a driven turbulence. These two chapters are therefore complementary. However, we have explicitly tried to keep both chapters independent at the cost of a limited amount of repetition in the description of the models.

4.2 A three-dimensional two-phase medium

We solve the equations of ideal gas dynamics (i.e., Eqs. 2.9-2.11) for a one component fluid on a 128^3 grid which represents a 1 kpc^3 volume of the ISM. We assume a polytropic equation of state with a specific heat ratio of 1.4 and impose periodic boundary conditions in the three directions. In a more consistent approach, the specific heat ratio γ would need to be determined by the local physical conditions. We assume that the value could not be 5/3 as we expect diatomic gas to appear in the denser regions leading to a local γ value of 7/5. Of course, it is clear that a constant $\gamma = 7/5$ to describe all phases of the gas is a simplification. Yet, here we are focusing just on some basic physics without including additional complications like a chemical network. A similar simplification has been adopted by Wada and Norman (2001). The initial conditions of all runs are identical and taken from a fully driven isothermal (T=10^4K) simulation evolved over one dynamical timescale $\tau_{dyn} = L_b/v_{rms0} \approx 10^8$ years, where $L_b = 1$ kpc and $v_{rms0} = 10$ km s^{-1} is the *rms* turbulent velocity. The average number density in the simulation box is $\bar{n} = 0.5$ cm^{-3}. The energy is injected in the isothermal simulations on large scales ($k_{inj} = 2$). The initial density distribution for the simulation with heating and cooling is inhomogeneous with $(\delta\rho/\rho)_{max} = 2.8$, and the velocity distribution corresponds to a Mach number $Ma_0 = 1$ turbulent medium. Turbulence driving is performed following the description given in §. 2.4. For a parametric study we assume the cooling and heating terms in the energy equation to be respectively $\Lambda(\rho, T) = \Lambda_0 \rho^\alpha T^\beta$ and $L(\rho) = q\Lambda_0\rho^\epsilon$. The latter is responsible for keeping a fraction of the gas in the unstable regime by restoring cold gas to the warmer phase. The minimum and maximum temperatures allowed in the simulations are 10 K and 12000 K, respectively. We use a simple prescription to account for the self-shielding of the clouds by nulling the heating term in the inner cells of a cloud and applying a shape dependent linear heating at the boundary cells of the cloud. This introduces a shielding density, n_{shield}, above which the shielding of the clouds becomes effective (the shielding density in physical units $\rho_{sh} = n_{sh}\ \mu\ m_H\ 5 \times 10^{-23}$ g cm^{-3}, where μ and m_H are the mean molecular weight and proton mass respectively). An inner cell is defined as a cell where all of its 26 neighboring cells have a density which is higher than the shielding density. A surface cell is defined as a cell where the number of neighboring cells with density larger than n_{shield} is greater than zero and less than 26 and the amount of heat it receives is proportional to $(q\Lambda_0 N_{open})/26$, where N_{open} is the number of cells in the surrounding of the considered cell which have a density lower than n_{shield}. Λ_0 can be related to the cooling timescale τ_{cool} by the relation displayed in Eq. 4.2. In physical units $\Lambda_0 \sim 5.5 \times 10^{-28}\ n^2\ T^\beta$ erg cm^{-3} s^{-1}.

$$\Lambda_0 = \frac{3}{2}\ \frac{(Ma_0 v_{rms0})^{1-\beta}}{\bar{\rho}^{\alpha-1}\tau_{cool}}. \tag{4.1}$$

To avoid the task of fixing an arbitrary cooling timescale, we parameterize the latter as a function of the dynamical timescale by introducing the parameter $\eta = \tau_{cool}/\tau_{dyn}$, in a similar fashion to what have been done by several authors (e.g., Sánchez-Salcedo et al. 2002). We are aware that the single power law we use to describe the cooling function for temperatures below 150-300 K and larger than 10^4 K is a simplification. The major reason for our choice is to avoid the many parameters that come into play when considering a parameterized, multi-polynomial cooling curve.

4.3 Parameter Study

In this study, α and ϵ have been fixed in all the simulations at the values of 2 (mimicking radiative cooling i.e., Spitzer 1978) and 1 (mimicking a constant background heating), respectively. We varied the three other parameters η (with $\beta = 0.25$, $q = 0.1$), β (with $\eta = 0.3$, $q = 0.1$) and q (with $\eta = 0.3$, $\beta = 0.25$) and analyzed the mass fractions of the cold (F_c) (< 150 K) and intermediate temperature gas (F_u) ($150 < T < 7500$) K. The simulations are evolved for 4 τ_{dyn} until the mass fractions reach, in a all simulations, stationary or pseudo-stationary values. Figs. 4.1-4.6 show the values of F_c and F_u in the simulations at different epochs. The latter figures show that F_u can reach high values of the order of 0.3, close to the value of 0.4-0.5 derived from observations in the Milky Way (Heiles 2001), but at a cost of an unrealistic small value for F_c. We ran simulations with other permutations of the parameters leading to $F_u \approx 0.3$-0.4, but it turned out that the outmost of what F_c can reach is a value of 0.1 (realistic value of $F_c \sim 0.4 - 0.5$). We conclude by stating that the maximal contribution of thermal processes of non-stellar origin to the mass fraction of the intermediate (e.g., unstable) is in the range of 10-20 %. The rest of the unstable gas must find its origin in the direct stellar heating of the gas by stellar outflows, winds or supernova explosions. The location of most of the unstable gas should be directly correlated with the location of star forming regions. A second conclusion we can draw from Figs. 4.1-4.6 is that the cooling rate Λ_0 is the most important parameter that determines the efficiency of TI. We find that TI always takes place for values of $\eta < 1$ (large Λ_0). For $\eta \geq 1$ (small Λ_0), the kinetic energy in the system is dissipated before TI comes into play and no significant over-densities can be produced. On the other hand for $\eta << 1$ (very large Λ_0), the available reservoir of thermal energy is radiated extremely fast and the medium achieves everywhere its minimum temperature, thus reducing the efficiency of TI.

4.4 Analysis of an efficient cooling medium

In this section, we select a model in which the TI is particularly efficient (model for which $\eta = 0.3, q = 1, n_{sh} = 25\ \bar{n}$, simulation A) and investigate in more detail the time evolution of the properties of the medium in this simulation. Fig. 4.7 displays snapshots of the three-dimensional structure of the medium at different epochs. The initial roundish condensations are replaced after a short nucleation phase (see also the discussion by Hennebelle and Pérault 1999) of 20-30 Myrs by a complex network of filaments and shells with the densest structures being located at the intersection of the filaments. The nucleation of dense cores requires that the compressions occur on scales larger than a critical scale l_{crit} which for the WNM is around $\simeq 15$ pc (Hennebelle and Pérault 1999) in order to assemble enough mass that enables the formation of dense structures. Since the medium initially contains compressions with a large

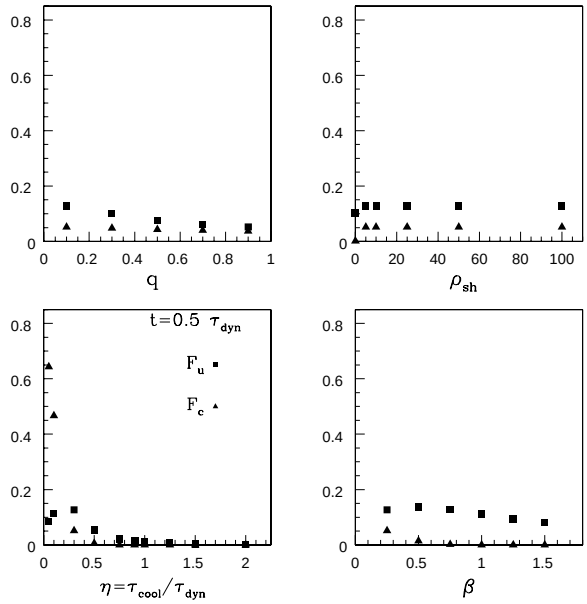

Figure 4.1: Mass fraction of the cold gas F_c ($T < 150$ K) and intermediate temperature gas F_u ($150 < T < 7500$ K) at t=0.5 τ_{dyn} as a function of the cooling-heating parameters. ρ_{sh} in all plots is in units of 5×10^{-24} g cm^{-3}.

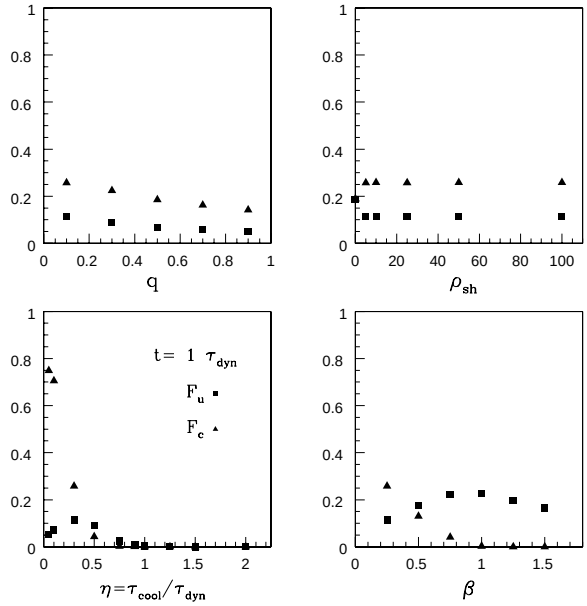

Figure 4.2: Mass fraction of the cold gas F_c ($T < 150$ K) and intermediate temperature gas F_u ($150 < T < 7500$ K) at t=1 τ_{dyn} as a function of the cooling-heating parameters.

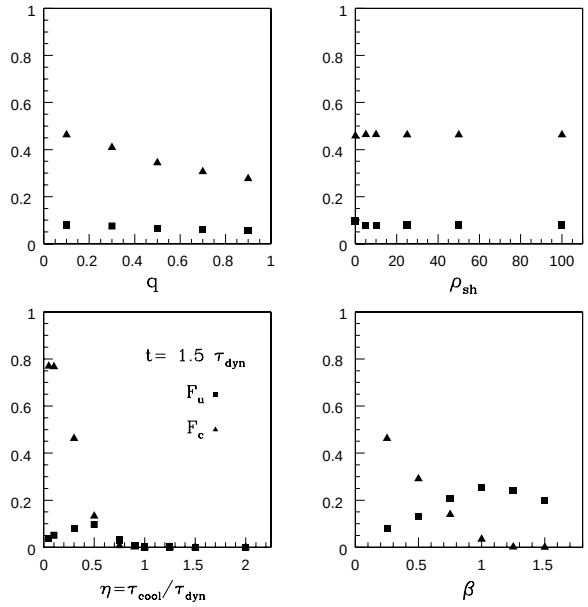

Figure 4.3: Mass fraction of the cold gas F_c ($T < 150$ K) and intermediate temperature gas F_u ($150 < T < 7500$ K) at t=1.5 τ_{dyn} as a function of the cooling-heating parameters.

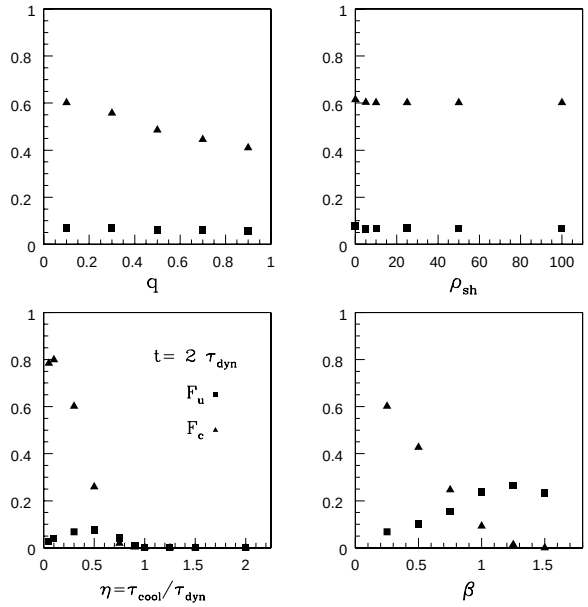

Figure 4.4: Mass fraction of the cold gas F_c ($T < 150$ K) and intermediate temperature gas F_u ($150 < T < 7500$ K) at t=2 τ_{dyn} as a function of the cooling-heating parameters.

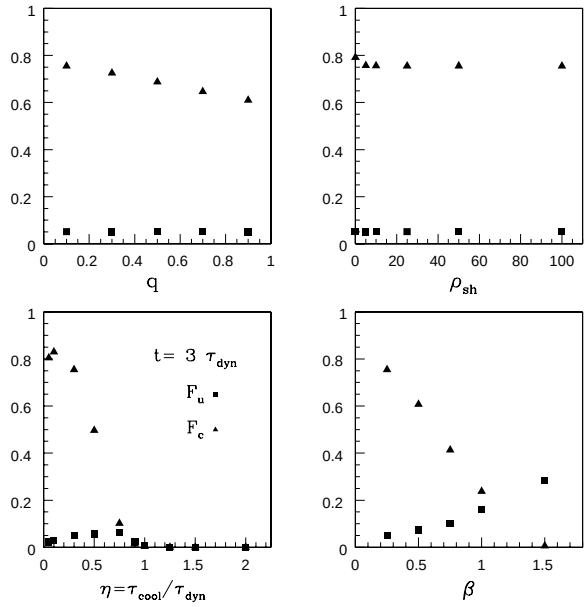

Figure 4.5: Mass fraction of the cold gas F_c ($T < 150$ K) and intermediate temperature gas F_u ($150 < T < 7500$ K) at t=3 τ_{dyn} as a function of the cooling-heating parameters.

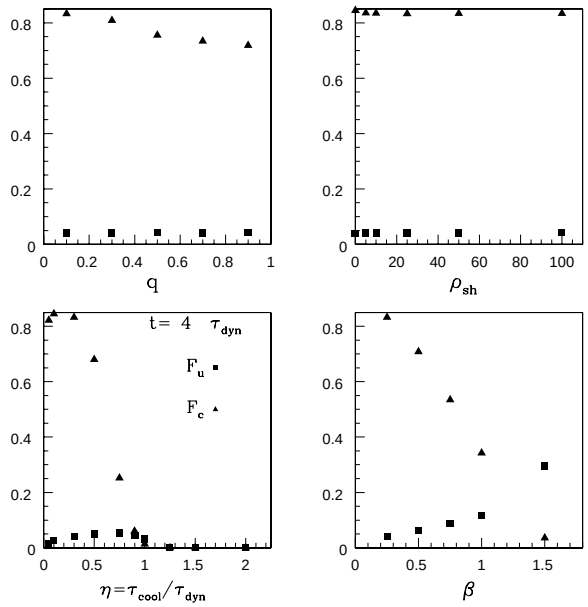

Figure 4.6: Mass fraction of the cold gas F_c ($T < 150$ K) and intermediate temperature gas F_u ($150 < T < 7500$ K) at t=4 τ_{dyn} as a function of the cooling-heating parameters.

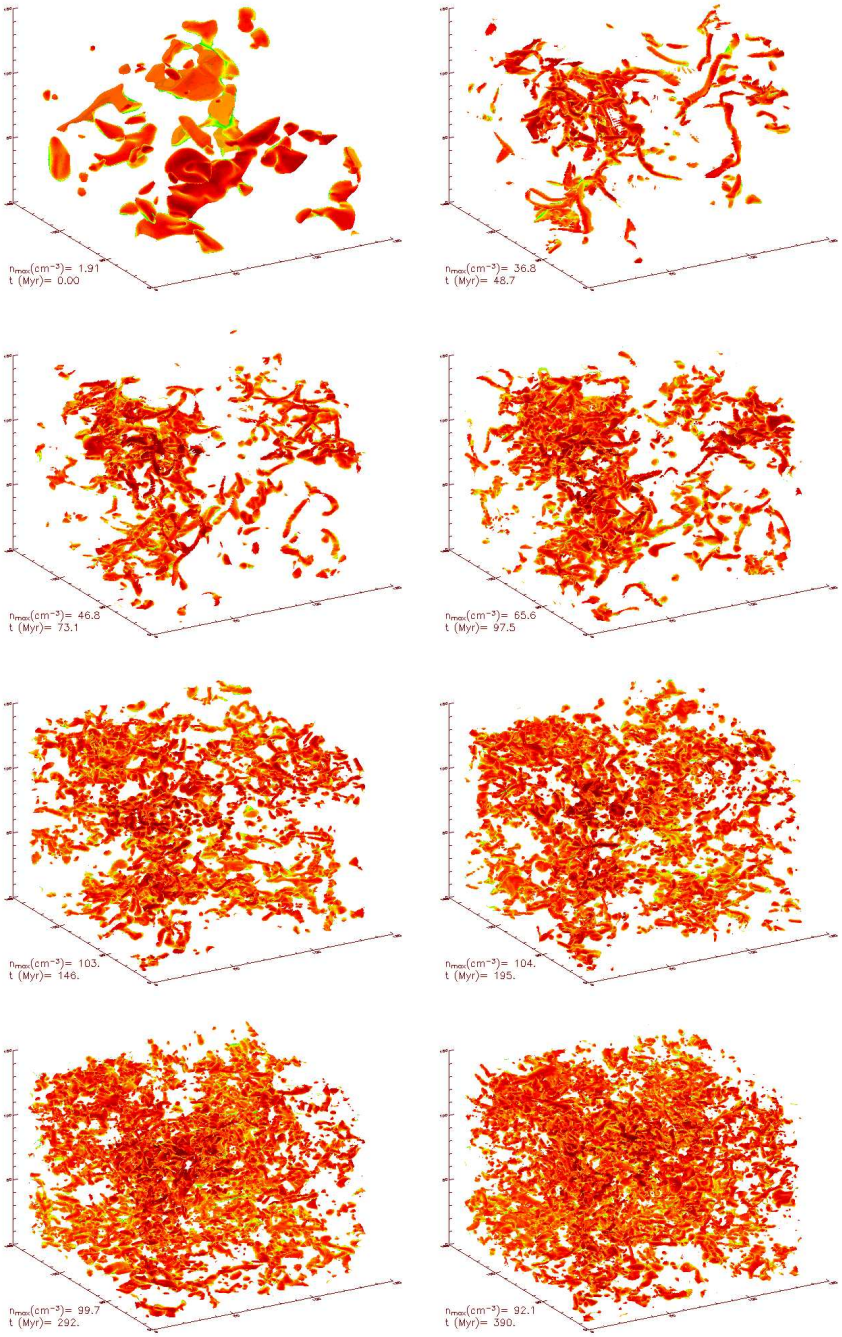

Figure 4.7: Snapshots of the density structure at different epochs in a medium subject to thermal instability, here without self-gravity. Iso-density contours correspond to $n \geq 3\ \bar{n}$, except for the initial frame where $n \geq 0.5\ \bar{n}$. Time (in Myrs) and the maximum density (in cm^{-3}) are shown at the lower left corner of each box.

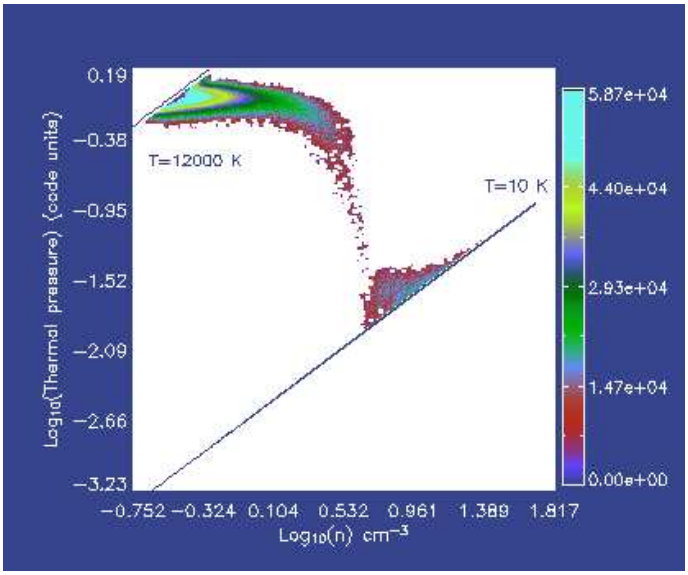

Figure 4.8: Phase diagram of the medium at $t = 1\ \tau_{dyn}$ (Log-Log plot). The color-bar shows the number of cells in each pressure-density bin. Diagonal lines show the temperature limits of 10 K and 12000 K.

spectrum of dimensions (from 500 pc down to 7.8 pc, i.e. 1 cell size), structure formation can begin on large scales which become denser with time until they start to fragment. In our three dimensional simulations, the large condensations/clouds also fragment under the effect of the existing (though decaying) turbulence, whereas the small condensations can either merge to form bigger ones or disperse under the effect of the background heating which erodes their surface particularly if they are made of a relatively low density gas and if they are not gravitationally bound. This first rapid phase of condensation is driven by the dynamical forcing and the condensations that are formed are far from pressure equilibrium. After the dynamical forcing has vanished (i.e., turbulence substantially decayed, see § 4.5) the pressure in the clouds relaxes back to values close to the values in the diffuse medium and the clouds begin a stationary growth phase until $t \simeq 1\ \tau_{dyn} = 97.5$ Myrs, which is the time at which the dense condensations have reached temperatures equal to T_{min} and the pressure gradients vanish. Fig. 4.8 shows a phase diagram (not mass weighted) of the medium at $t = 1\ \tau_{dyn}$. One can clearly see the existence of two stable phases at $T = 10$ K and $T = 12000$ K and unstable gas with $dP_{th}/d\rho < 0$ (see Eqs. 3.13-3.14). The medium evolves afterwards in a statistical temporal steady state. In this medium characterized by a low level of turbulence, small clouds can still form, merge in order to form larger ones, or be dispersed by cloud-cloud scattering and eventually the background heating. After $t = 1\ \tau_{dyn}$, the statistical properties of the medium are roughly unchanged (see fig. 4.7). Fig. 4.9 shows the evolution of the probability distribution function (PDF) of the gas number density, which initially possessed a unimodal distribution characteristic of a turbulent isothermal medium, and which finally settles into a stationary bimodal distribution.

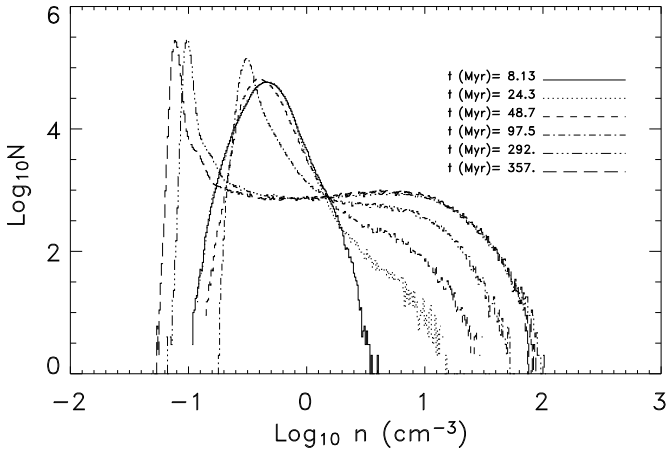

Figure 4.9: Density probability distribution function (PDF) of the medium at different epochs of the medium subject to thermal instability (without gravity; i.e. simulation A). After $\simeq$ 100 Myrs a bimodal distribution is observed.

4.5 Does thermal instability drive turbulence ?

In the previous section, we have focused on the effects of TI on structure formation in the ISM. Another interesting aspect to study is : to which level the potential contribution of kinetic energy from thermal instability can slow down the fast energy decay ($\simeq$ over one dynamical timescale) that is observed in the idealized case of isothermal simulations of decaying turbulence ? (see § 1.2.1), and thereby provide a source of turbulent support for molecular clouds. Fig. 4.10 displays the kinetic energy power spectrum at different epochs (for simulation A, described in § 4.4). The spectrum shows that kinetic energy injection into the medium due to thermal instability takes place exclusively on the smallest scales (up to a scale of the order of 60 pc), thereby changing the spectrum slope in the inertial range (i.e., range between the energy injection scale and energy dissipation scale). The initial spectrum at $t = 0$ follows an $E(k) = k^{-1.46\pm0.04}$ law, in good agreement with the predicted decay law for a weakly compressible turbulence (Ruzmaikin et al. 1988, see also §. 1.2). The spectral index for the medium when cooling is effective is shallower. At $t = 0.5\ \tau_{dyn} = 48.79$ Myrs, the spectral index is $\simeq -1.17 \pm 0.024$. However, the further time evolution of the spectrum shows that kinetic energy is lost thereafter on all scales, particularly faster on the larger scales. Fig. 4.11 shows the temporal evolution of the total kinetic energy in the system (kinetic energy is here in code units, for a conversion to physical units, the conversion factor in A.1 should be used). A rapid power law decay of kinetic energy with time was uncovered in the isothermal case, $E_c \propto t^{\xi}$, with ξ being in the range $[-1, -0.8]$, depending on the Mach number (Stone et al. 1998; Mac Low et al. 1998; Smith et al. 2000). Similarly to isothermal simulations of decaying turbulence, turbulence in the simulation with efficient cooling is observed to decay rapidly over a timescale of the order of the dynamical timescale, even faster than in the isothermal case (see fig. 4.11). A fit to the decay rate between $t = 0.5\ \tau_{dyn}$ and $t = 4\ \tau_{dyn}$ shows that turbulence decays as $E(k) = t^{-1.537\pm0.003}$. This result is very similar to the one obtained

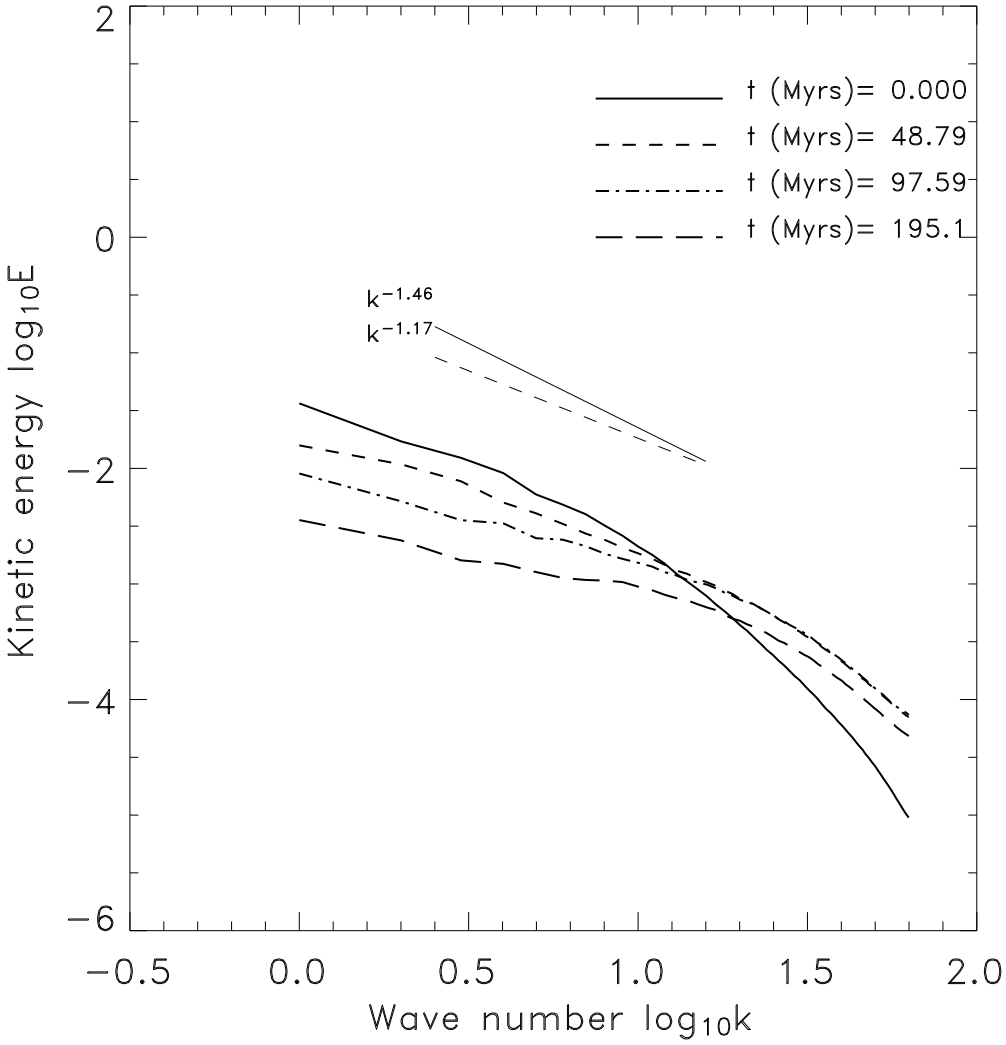

Figure 4.10: Kinetic energy power spectrum at different epochs. For a better visibility, the fits for the spectra at $t = 0$ and $t = 0.5\tau_{dyn} = 48.79$ Myrs in the inertial range are artificially shifted up by one order of magnitude. At $t = 0$, the spectrum follows an $E(k) = k^{-1.46}$ law which is in good agreement with the predictions for a weakly compressible turbulence (Ruzmaikin et al. 1988, see §. 1.2). The '*cooling medium* spectra shows a shallower slope of $\simeq -1.17$.

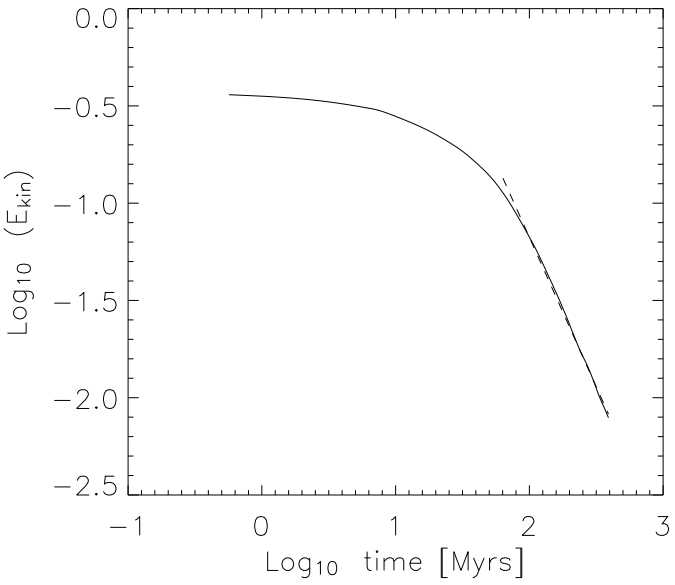

Figure 4.11: Time evolution of the total kinetic energy ins simulation A (given here in code units). Log-Log plot. Dashed line is a fit to the data for t/τ_{dyn} in the range [0.5,4].

by Pavlovski et al. (2002), which investigated decaying turbulence in a medium where the chemistry of the H_2 molecule has been taken into account.

4.6 The role of gravity

We describe in this section the evolution of a simulation (simulation B) with similar cooling-heating parameters than those used in simulation A, additionally accounting for the self-gravity of the gas. The Poisson equation describing the evolution of the gravitational potential is solved using the algorithm discussed in § 2.2. The medium is initially globally stable against gravitational collapse. Fig. 4.12 displays snapshots of the density structure at different epochs. The evolution of the medium in the first phase $t \lesssim 20 - 25$ Myrs is very similar to the case of simulation A. Beyond that point, the first condensations that form in the medium are affected by self-gravity, causing them to contract faster and accrete more material until $t \sim 70$ Myrs. Strong accretion onto the massive condensations follows until, at $t \sim 1\ \tau_{dyn}$, the largest and densest condensations become jeans unstable and undergo gravitational collapse. This causes the maximum density in the medium to rise sharply and reach values of the order of a few 10^4 cm^{-3}, which is at least two order of magnitude larger than the over-densities produced by the thermal instability alone which can lead to the formation of over-densities of a factor $\sim 1 - 2 \times 10^2$ (see Fig. 4.13 which compares the time evolution of the maximum density in the system for simulations A and B). The further evolution of the system is purely dictated by gravity. Self-gravitating clouds accrete all the surrounding gas until the system reaches the stage of cloud-cloud accretion. Ultimately, this process will lead all the gas to collapse into one cell. We are not particularly interested in studying the further development of the

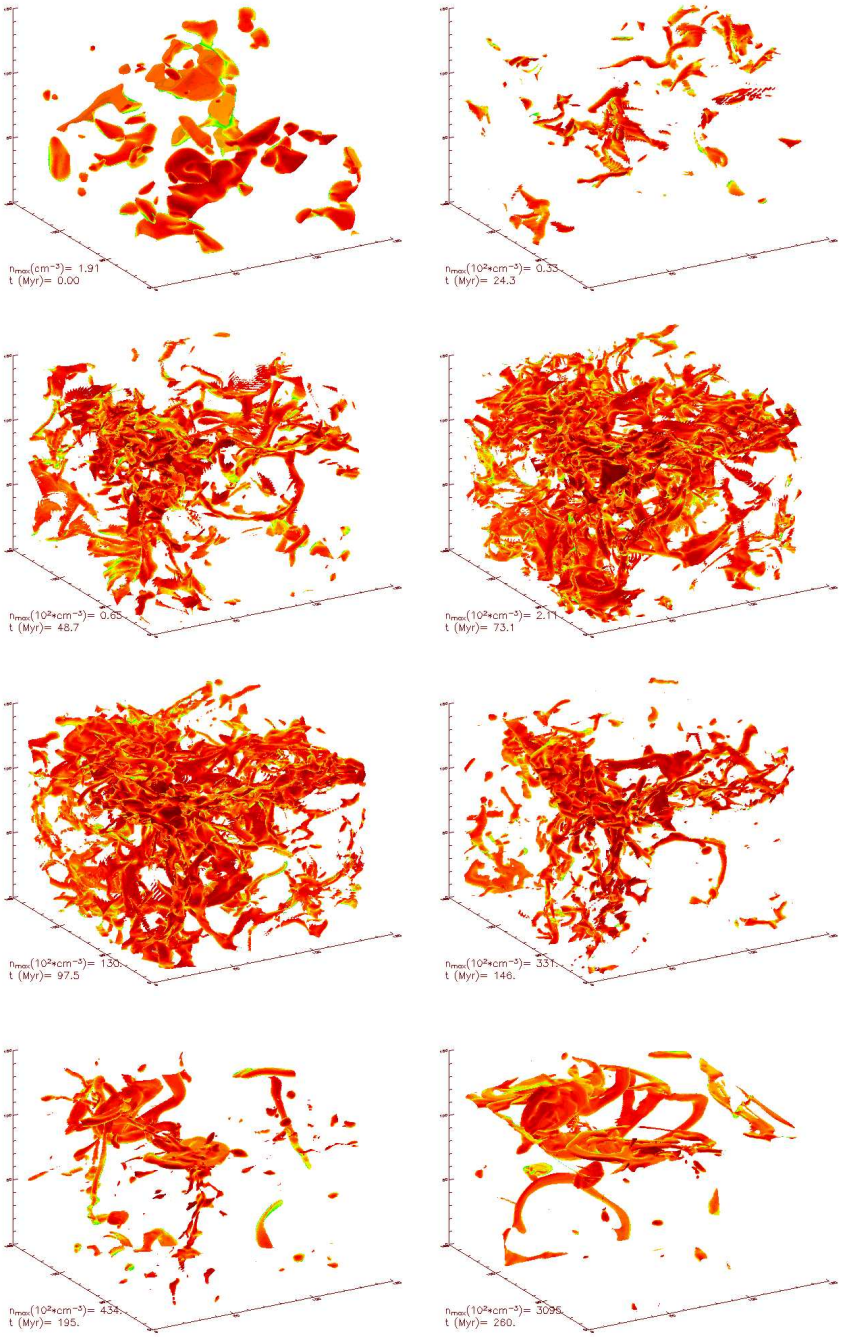

Figure 4.12: Snapshots of the density structure at different epochs in a medium subject to thermal instability with self-gravity included. Iso-density contours correspond to $n \geq 3\ \bar{n}$, except for the initial frame where $n \geq 0.5\ \bar{n}$. Time (in Myrs) and the maximum density (in cm^{-3}) are shown at the lower left corner of each box.

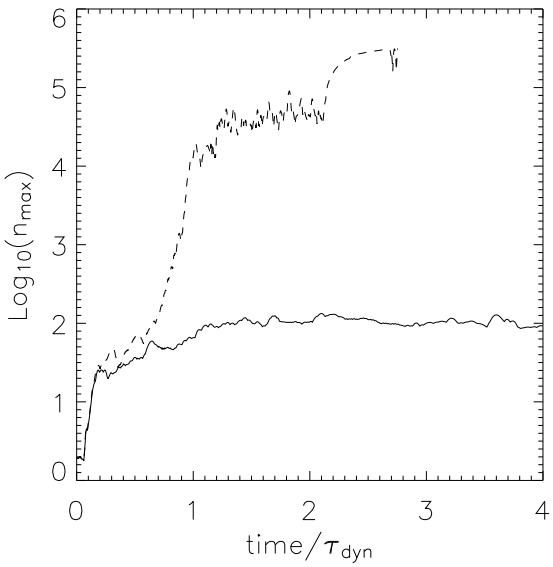

Figure 4.13: Time evolution of the maximum of the number density in the medium subject to thermal instability with and and without the effect of self-gravity, dashed and full line, respectively. Time is shown in units of the dynamical time.

gravitational instability, mainly because of numerical resolution problems and the absence of star formation and stellar feedback in the present simulations. However, the point we intend to stress here, is that thermal instability plays the role of a transition agent which is able to compress diffuse interstellar matter by a factor of $\sim 1 - 2 \times 10^2$ until bound gravitational structures can eventually form. Fig. 4.14 shows that there is no substantial increase in the total kinetic energy of the system when self-gravity is accounted for as compared to the medium affected by thermal instability alone. Only after gravitational collapse occurs (at $t \sim 0.8\, \tau_{dyn}$), gravitational energy is released into the system and partially converted into kinetic energy. However, this kinetic energy generation process by gravitational collapse can not account for the turbulence observed in quiescent regions of the ISM (diffuse ISM and quiescent clouds), where gravity is only playing a negligible role. We therefore conclude that from a dynamical point of view, the presence of gravity does not help thermal instability be more efficient in producing a self-sustained turbulence in the medium in the stages preceding gravitational collapse. In the next chapter we will perform a virial analysis of the condensations in a medium subject to thermal instability and where self-gravity is accounted for, but in the more realistic context of thermal instability operating in a turbulent ISM.

4.7 Larson relations

The interstellar medium structure and dynamics are often described with scaling laws known as the Larson relations (Larson 1981), and later confirmed by other observational studies. The Larson relations have the form

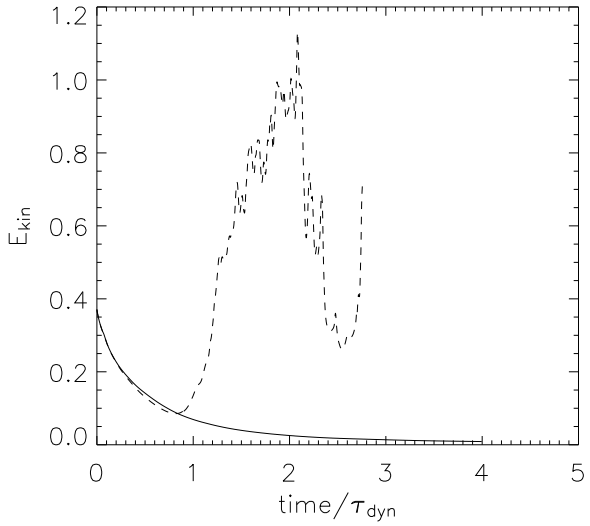

Figure 4.14: Time evolution of the total kinetic energy (given here in code units). Full line is for a simulation without self-gravity (simulation A, similar to data in Fig. 4.10) and dashed-dotted line for a simulation with self-gravity (simulation B).

$$< n > \sim R^{\alpha}, \tag{4.2}$$

$$\sigma \sim R^{\beta}, \tag{4.3}$$

where R is the cloud size (could be a molecular cloud, a giant molecular cloud or a neutral H I cloud), n is the gas average number density, and σ the velocity dispersion in the cloud. α and β are constant scaling exponents. Clouds are also found to exhibit a mass spectrum

$$\frac{dN_c(M)}{dM} \sim M^m, \tag{4.4}$$

where m is also a constant scaling exponent and N_c is the number of clouds in each mass bin. The most quoted values of α, β and m in the literature are $\alpha \sim -1.0 \pm 0.15$, $\beta \sim 0.4 \pm 0.1$ and $m \sim -1.55 \pm 0.15$ (Larson 1981; Dame et al. 1986; Myers and Goodman 1988; Falgarone et al. 1992; Fuller and Myers 1992; Miesch and Bally 1994; Wood et al. 1994; Caselli and Myers 1995; see also the review by Scalo 1985). However, discrepant values of the exponents α, β and m have also been reported (e.g., Carr 1987; Loren 1989). The existence of these scaling relations and particularly the mean density-size relation (i.e., Eq. 4.2) are still matter of debate in the community. Vázquez-Semadeni et al. (1997) searched for Larson-type relations in two-dimensional numerical simulations of the ISM which include cooling, background heating, gravity and magnetic fields and with and without an additional stellar-wind like heating whereas Ballesteros-Paredes and Mac Low (2002) searched for these relations in two-dimensional line-of-sight integrated density maps obtained from three-dimensional MHD isothermal simulations. The latter authors were able to recover relations 4.3 and 4.4 from

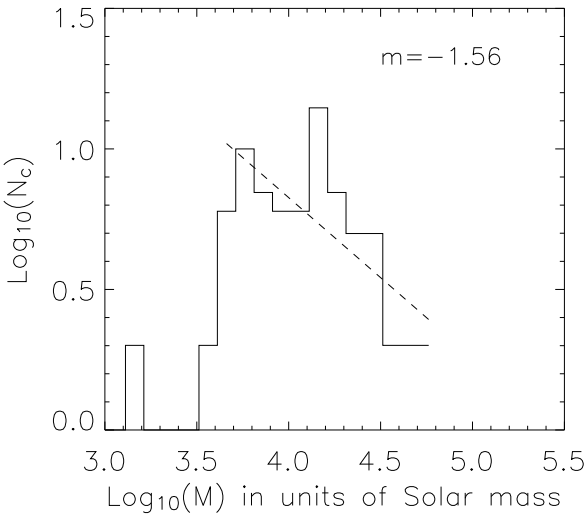

Figure 4.15: Mass spectrum of the condensations found in the medium at $t = 1\ \tau_{dyn} = 97.5$ Myrs. The adopted density threshold is 8 $\bar{n}$. The fit (over-plotted to the data) yields a slope of the spectrum of -0.56 ± 0.15. Thus, the value of the exponent m in Eq. 4.4 is -1.56 ± 0.15. The cutoff at lower masses is artificial and due to the selection of the 80 densest condensations only.

the numerical simulations (see Figs 3, 4 in Vázquez-Semadeni et al. 1997), but they found the average density to be independent of the cloud's size (Fig. 5 in Vázquez-Semadeni et al. 1997). Both this result and the fact that clouds need not to be in virial equilibrium in order to explain the observed relations (see below) have led them to speculate that the average density-size relation might be merely originating from an (unspecified) observational artefact (see also Scalo 1990).

The above described values of the exponents have been interpreted by several authors in the frame of the virial theorem (Larson 1981; Myers and Goodman 1988; Caselli and Myers 1995). In fact, for $\alpha = 1$, virial balance between the self-gravity of the gas and the internal velocity dispersion in the condensation (i.e., turbulent support) would imply a value of $\beta = 0.5$. However, as already pointed out by Vázquez-Semadeni and Gazol (1995), a virial balance can be found for arbitrary combinations of α and β. Thus, virial equilibrium can not explain the observed Larson relations.

In this section, we apply our clump finding algorithm described in § 2.3 and search for Larson-type relations in simulation A at a time where clouds have already formed, namely at $t = 1\ \tau_{dyn} = 97.5$ Myrs. We have searched for the 80 most massive condensations using a density threshold of 8 $\bar{n}$. The mass M, characteristic scale R and characteristic velocity dispersion σ of the condensations have been calculated following the description given in § 2.3. The mass spectrum of the condensations is displayed in Fig. 4.15 (Log-Log plot). The fit to the spectrum for masses larger than $10^{3.6}$ $M_\odot$ yields a slope of -0.56 ± 0.15. Thus the value

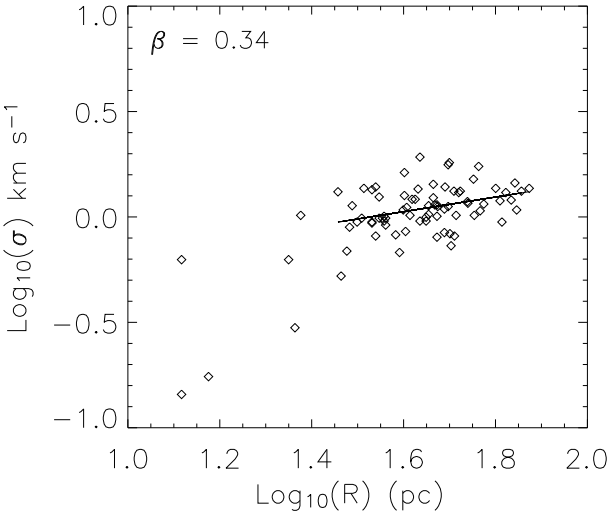

Figure 4.16: Velocity dispersion versus size at $t = 1\ \tau_{dyn} = 97.5$ Myrs in simulation A. We fit clouds only clouds which have a one-dimensional characteristic size larger than 4 pixels ~ 28 pc. For condensations with less than 4^3 pixels, the velocity dispersion loses its meaning due to the low statistics. The linear fit, over-plotted to the data, has a slope of $\beta = 0.34 \pm 0.10$.

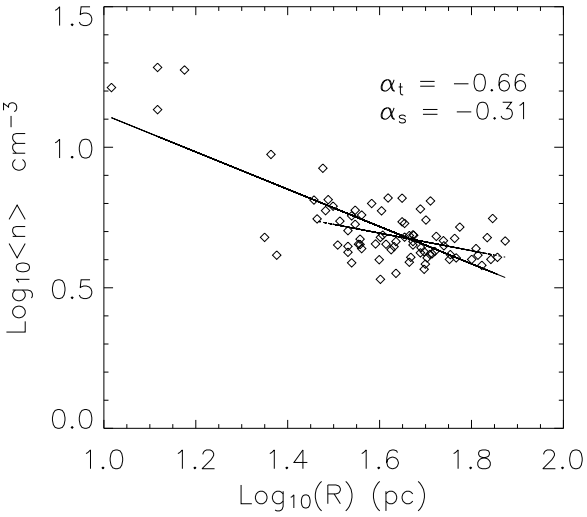

Figure 4.17: Average number density versus size at $t = 1\ \tau_{dyn} = 97.5$ Myrs in simulation A. We fit for all cloud sizes and for clouds with a minimum one-dimensional characteristic size of 4 pixels (~ 28 pc). The linear fits have slopes of $\alpha_t = -0.66 \pm 0.06$ and $\alpha_s = -0.31 \pm 0.07$, respectively.

of the exponent m in Eq. 4.4 is -1.56 ± 0.15, in excellent agreement with the observations. The velocity dispersion-size relation and the average density-size relation are displayed in Fig. 4.16 and Fig. 4.17, respectively. For the $\sigma - R$ relation, we fit only for clouds which have a one-dimensional characteristic size R larger than 4 cells (~ 28 pc). For condensations with less than 4^3 cells the velocity dispersion of the condensation is poorly defined. In the case of the $< n > -R$ relation, we fit for all cloud sizes and for clouds with $R > 28$ pc. The linear fits to the data yield values of $\alpha = -0.66 \pm 0.06$ and -0.31 ± 0.07, respectively. Considering the scatter we have in our data points, especially for the smaller condensations, the agreement to the observational values is particularly encouraging. We find, in contrast to Vázquez-Semadeni et al. (1997) and Ballesteros-Paredes and Mac Low (2002), and in agreement with the observations, that the $< n > -R$ is an intrinsic property of the three-dimensional structure of the condensations in the ISM. However, we have searched for this relation directly in the three-dimensional data and not in the two-dimensional observational space as an observer would do. We also searched for the Larson-type relations in other simulations where thermal instability is efficient (for $\eta = \tau_{cool}/\tau_{dyn} < 0.3$), and found, with some scatter, the relations to be satisfied. The discrepancy of our results with the results of Ballesteros-Paredes and Mac Low (2002), as far as the $< n > -R$ relation is concerned, might be simply due to the low density contrasts (n_{max}/n_{min}) reached in their isothermal simulations and thus, the nearly constant density they obtain. However, this can not explain the discrepancy between our results and the results of Vázquez-Semadeni et al. (1997), as the density contrasts (n_{max}/n_{min}) reached in our and their simulations are similar and of the order of a few 10^3. The difference might be an effect of dimensionality due to the difficulty they have in defining properly the surface and volume of each condensation in their two-dimensional simulation.

We conclude this section by stating that thermal instability imprints the basic scaling relations of the condensations in the ISM. An analysis of the condensations found in one of our simulations where thermal instability is efficient leads to a very good agreement between the exponents of the Larson relations derived from the observations and those derived from our numerical model. In a future work, we intend to search for Larson-type relations in improved models, namely for models with chemistry, an improved description of cooling and heating processes and with higher numerical resolution. Additionally, the two-dimensional versus three-dimensional relations should be compared from the same simulations in order to better understand the effects of the integration along the line of sight.

Chapter 5

The origin of the H I holes in dwarf irregular galaxies

5.1 Introduction

The question of which physical processes produce the holes observed in the 21 cm H I line in the interstellar medium (ISM) of many galaxies such as in the Large Magellanic Cloud (LMC) (Kim et al. 1999), Holmberg II (Ho II, DDO 50, UGC 4305) (Puche et al. 1992), the Small Magellanic Cloud (SMC) (Staveley-Smith et al. 1997; Stanimirovic et al. 1999) and the Western Magellanic Bridge (Muller et al. 2003) has been a controversial and puzzling issue in the past. On the observational side, there are evidences that many of the shell and void-like structures observed in the ISM of different galaxies, especially in the outer parts of their galactic disks are unlikely to be the result of supernova explosions. Kim et al. (1999) came to this conclusion for the LMC in view of the weak correlation that exists between the positions of some of the H I shells and the H II regions. Using a multicolor BVR imaging approach, a careful study by Rhode et al. (1999) of the 51 H I holes in Ho II, previously selected by Puche et al. (1992), shows no signs of the presence of remnant stellar clusters inside 86 percent of these holes (see Fig. 5.1 and Fig. 1.2). Additionally, using Hα photometry, they could not confirm the presence of any ongoing star formation process inside the holes (i.e., Fig. 5.2). Based on these observations, they concluded that those holes can not be supernova driven expanding shells. Furthermore, Stewart et al. (2000) observed the far-ultraviolet (FUV) emission of Ho II. The FUV emission is sensitive to massive star formation on a timescale which is comparable to the lifetime of the largest holes in Ho II ($\sim$ 100 Myrs). Only 3 out of the 51 H I holes selected by Puche et al. (1992) have associated FUV emission whereas in the rest of the holes the emission is concentrated at their edges. Furthermore, only very little FUV emission is detected outside the $2'$-$3'$ radii inner region, indicating that star formation has played only a little role in the outer region. X-ray observations of Ho II using ROSAT PSPC by Zezas et al. (1999) and Kerp et al. (2002) have shown that most of the H I holes are devoid from hot gas. However, Kerp et al. (2002) showed that a few X-ray sources (sources 2 and 4 in Fig. 1 in their article), located outside the Stellar Disk but within the H I distribution of Ho II have emission that might be associated with thermal plasma radiation which is characteristic of supernova remnants. This suggests that, the supernova scenario can not be entirely ruled out in the case of those few holes.

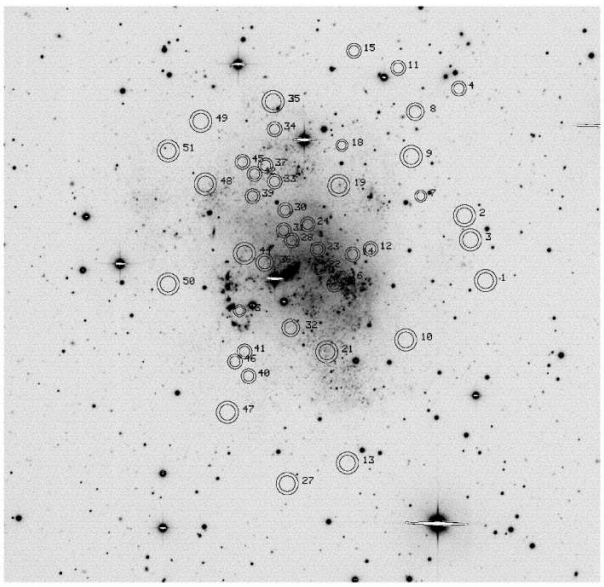

Figure 5.1: Composite *BVR* image shown on the same scale as the H I map in Fig. 1.2. The locations of the H I holes are indicated by concentric circles identical to those in Fig. 1.2. The figure is adapted from Rhode et al. (1999).

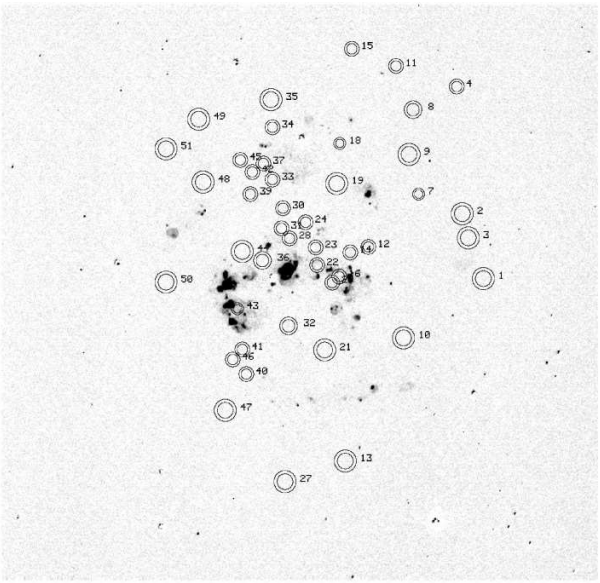

Figure 5.2: Continuum-subtracted Hα image, shown on the same scale as Fig. 1.2 and Fig. 5.1 with the locations of the H I holes marked. Note that, with the exception of holes 16, 20 and 43, none of the H I holes are coincident with H II regions. In addition, none of the holes that are not associated with H II regions contain any detectable diffuse Hα emission. The figure is adapted from Rhode et al. (1999).

Alternative mechanisms which could lead to the creation of the H I holes in Ho II have been discussed by several authors (Rhode et al. 1999; Bureau and Carignan 2002). Some of the proposed scenarios are related to the supernova scenario, like invoking a non standard initial mass function and modifying the holes energetics which helps to reduce the number of supernovae needed to create them. The latter scenario was pointed out by Rhode et al. (1999). However, it would require a reduction of the supernova rate by a factor of ~ 5 in order to have a remnant stellar cluster with a luminosity that falls below their detection limit. This in turn would require that the expansion velocities in the case of the largest holes have been overestimated by a factor ~ 3 by Puche et al. (1992), which seems unlikely. The scenario of an extremely top-heavy IMF in Ho II is also not supported by any observations of significant variations in the IMF measured in different environments like the Milky Way or other nearby galaxies (Leitherer 1999) and thus, seems also very unlikely. H I holes could also be created by the impact of High-Velocity Clouds (HVCs) on the gaseous disk. In the case of the Milky Way and other galaxies it has been shown that some holes are associated with high velocity gas (Heiles 1984 for the Milky Way; van der Hulst and Sancisi 1988 for M101). In the case of Ho II, only one object has been identified by Rhode et al. (1999) as a possible HVC. This object has an estimated mass of $1.2{\times}10^7$ $M_\odot$ and a total kinetic energy of $\approx 5 \times 10^{53}$ ergs. This amount of energy is enough to create any of the observed H I holes in Ho II. Aside from being statistically not very significant, this cloud has been detected on only one pixel in the whole data set. As already pointed out by Rhode et al. (1999), the signal detected from that pixel could also be assimilated to noise under the assumption that the noise in the data set is Gaussian. Only a more sensitive study of the H I structure around Ho II can shed more light on the existence and role of HVCs. By re-processing the low resolution map of Puche et al. (1992), Bureau and Carignan (2002) have unveiled the large scale structure of the H I in Ho II to be comet-like. They interpret this as gas in Ho II experiencing ram-pressure stripping under the effect of the intra-group medium (IGM) and that this process might lead to the formation of some holes or to the enlargement of existing ones. This scenario would only work if the IGM density is $n_{IGM} \gtrsim 4.0 \times 10^{-6}$ cm^{-3}. Bureau and Carignan (2002) pointed out to the fact that tidal interactions on the scale of the subgroup of galaxies containing Ho II, Kar 52 and UGC 4483 could also affect the H I morphology of Ho II. However, a preliminary analysis of the H I structure on the subgroup scale by Bureau et al. (2004) does not support the scenario of gas being tidally stripped from the disk of Ho II in the direction of Kar 52 and vice versa. It is also inconclusive with regard to the role played by ram pressure stripping.

In this work, we investigate whether the H I morphology could also emerge as the result of internal gas dynamics as earlier suggested by Elmegreen (1997). Our aim is to explore the role played by turbulence and by thermal (Field 1965; Field et al. 1969) and gravitational instabilities (Kolesnik 1991) (TI and GI, respectively) on the formation of large scale structure in the ISM. We use three-dimensional hydrodynamical isothermal simulations of driven turbulence to investigate if holes like those in Ho II are formed as a natural consequence of the turbulence present in the medium. We then study the effect of heating and cooling and take the self-gravity of the gas into account. In a post-process approach, we build two dimensional emission maps in the 21 cm H I hyperfine structure line and compare them to observations.

In §. 4.1, we have discussed some of the numerical investigations related to TI. However none of the previous authors have performed a quantitative comparison of the resulting H I structure in their models to the observations. Vázquez-Semadeni et al. (2000a) and Gazol

et al. (2001) performed local two-dimensional numerical simulations to investigate TI in the ISM on a scale similar to ours (1 kpc) focusing on the segregation of the medium into two distinct gaseous phases. However, they did not build emission maps that can be compared with observations. Wada and Norman (1999, 2001) and Wada et al. (2000) have shown that the combined effect of TI and GI with turbulence can lead to the formation of H I holes. They performed global two-dimensional numerical simulations of an LMC-type galactic disk and constructed from their hydrodynamical data emission maps in the 21 cm H I and the CO(1-0) lines. They transformed their two-dimensional grid into a three-dimensional one by assuming a constant scale height for the disk, divided in a number of grid cells. Though they used a rather sophisticated approach to solve the radiation equation in each of the newly created cells, the local densities in all cells along a given line of sight were assumed to be the same, which is a major simplification. Additionally, although a similarity in the complex network of holes and shells is observed between their simulated H I map and observations of the structure in the 21 cm line of the LMC, they did not quantify the hole and shell-like structures. This contrasts with our simulations which take into account the complexity of the three-dimensional structure, which arises self-consistently. The H I holes formation process by TI and GI in the ISM of dwarf irregular galaxies is critically reviewed by Sánchez-Salcedo (2001). This chapter is organized as follows. In § 5.2 we describe our set of simulations. The radiative transfer approach we use to construct the emission maps is described in § 5.3. In § 5.4, we define the observable quantity which we use to compare our models with observations. In § 5.5, we present the observational data and in § 5.6 we evaluate the autocorrelation length in our simulated H I maps and compare it with the observations. In § 5.7, we summarize our results.

5.2 The simulations

We use the ZEUS-3D code (Stone and Norman 1992a,b, § 2.2) to solve the equations (mass, momentum and internal energy conservation) of ideal gas dynamics. In addition, we solve the Poisson equation to account for the self-gravity of the gas in some of the simulations. The Poisson equation is solved as described in § 2.2. The grid represents a 1 kpc^3 volume of the ISM, and the calculations are performed with a resolution of 128^3 grid cells. A polytropic equation of state with a specific heat ratio of 1.4 is used. Periodic boundary conditions are imposed in all three directions. The medium is originally uniform in density with an average density $\bar{n} = 0.5$ cm^{-3}, which is the typical value for the warm interstellar medium.

We first performed a number of isothermal simulations (runs ISOimj in Tab. 5.1) in which the turbulence is driven on different length scales and with different Mach numbers (i indicates the driving wave number and j the Mach number). The initial density fluctuations for the isothermal runs are generated following the description given in Klessen (1998) and Klessen & Burkert (2000). The density fluctuations are described by a power spectrum $P(k) = k^m$. We have chosen $m = 0$, which implies that the energy is distributed equally on all scales. We should however mention that since the medium is constantly driven, its evolution is rather independent of the initial conditions. We mimick the turbulence driving by compensating for the energy lost through dissipation by injecting random motions to the gas such that the total injected energy is equal to the energy-dissipation rate following the description given in § 2.4. The medium is evolved over two dynamical timescales. The dynamical timescale is defined

Model	k	Ma	Gravity	η
ISO2m1	2	1	no	0
ISO4m1	4	1	no	0
ISO2m05	2	0.5	no	0
ISO2m2	2	2	no	0
ISO2m3	2	3	no	0
ISO2m5	2	5	no	0
CO03G2	2	-	yes	0.3
CO03T2	2	-	no	0.3
CO06G2	2	-	yes	0.6
CO09G2	2	-	yes	0.9

Table 5.1: Model runs. k is the driving wave number, Ma the driving Mach number and $\eta = \tau_{cool}/\tau_{dyn}$ the cooling efficiency parameter.

as the ratio of the box size L_b to the initial *rms* turbulent velocity $\tau_{dyn} = L_b/v_{rms,0} \sim 10^8$ years, where L_b=1 kpc and $v_{rms0} = 10$ km sec^{-1}. The value of 10 km s^{-1} has been chosen as being a typical value of the warm phase in the ISM. In these isothermal simulations, the medium reaches a statistical steady state (similar probability distribution functions) after one dynamical timescale with the largest over-densities being of the order of $\delta\rho/\rho \sim 2.8$.

The density and velocity distributions inherited after evolving the medium for one dynamical timescale in the isothermal regime (with $k = 2$ and $Ma = 1$) are used as initial conditions for simulations of driven turbulence including cooling and heating (Runs CO0jGi in Tab. 5.1). G stands for runs where self-gravity is included (T otherwise), j describes the cooling efficiency (see below) and i the above mentioned wave number value. The simulations are evolved for two dynamical times after heating and cooling are turned on. An initial *rms* Mach number of 1 is reasonable given the observed H I velocities of a few km s^{-1} with temperatures of a few 1000 K. The initial density distribution for the simulations with cooling is inhomogeneous with $(\delta\rho/\rho)_{max} = 2.8$ and temperature is set initially everywhere to 10^4 K. We assume the cooling and heating terms in the energy equation to be, like in Chap. 4, respectively, $\Lambda(\rho, T) = \Lambda_0\rho^\alpha T^\beta$ and $L(\rho) = q\Lambda_0\rho^\epsilon$. The later term is responsible for keeping a non-zero fraction of the gas in the intermediate temperature regime by heating up the envelopes of dense clouds and restoring cold gas to the diffuse phase. The temperature is allowed to vary between 10 K and 12000 K. We set $\alpha = 2$ mimicking the density squared dependence in the cooling function describing radiative cooling (Spitzer, 1972) and $\epsilon = 1$, thus mimicking a constant background heating. Shielding is also taken into account and treated in a similar fashion to what has been described in § 4.2.

In this chapter, we shall analyze a number of models for which the combination of free parameters leads to TI (see Chap. 4), with $\beta = 0.25$, $q = 0.1$ and $n_{shield} = 25\bar{n}$ where $\bar{n}$ is the mean particle density of the gas. This choice of parameters leads to TI where the thermal-equilibrium pressure decreases when density increases (See Eq. 3.14 and Eq. 9 in Vázquez-Semadeni et al. 2000a). We vary the cooling rate Λ_0 in the different simulations. The cooling rate is inversely proportional to the cooling timescale τ_{cool} (Dib et al. 2004, Chap. 4) which

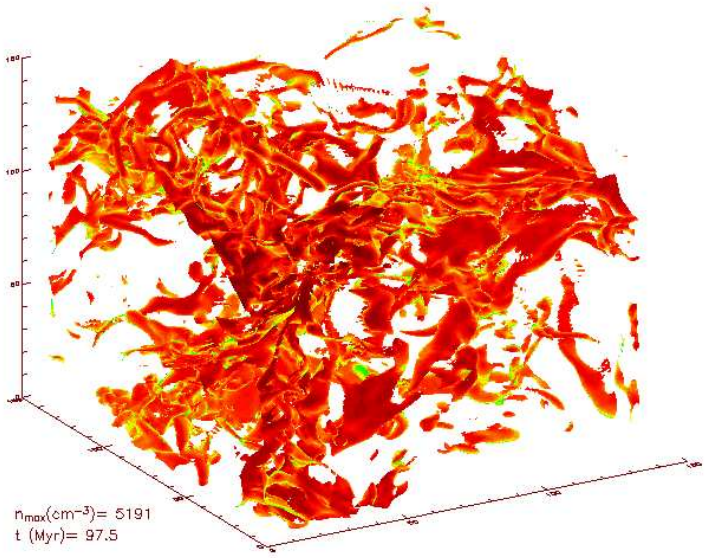

Figure 5.3: Three-dimensional density structure of the medium at t=τ_{dyn} = 97.5 Myrs in model CO03G2. The iso-density surface corresponds to a value of 10 $\bar{n}$ ($\bar{n}$ = 0.5 cm^{-3}).

can be parameterized as a fraction η of the dynamical time : $\tau_{cool} = \eta\ \tau_{dyn}$. Dib et al. (2004) (also Chap 4) have run a large number of simulations similar to those presented here, but for decaying turbulence. In those simulations the mass fractions of cold ($T < 150$ K) and intermediate ($150 < T < 7500$ K) are checked after they have reached stationary (or pseudo-stationary) values. We found that TI always takes place for values of $\eta < 1$. For $\eta \geq 1$ (corresponding to small values of Λ_0) the kinetic energy is dissipated before TI comes into play and no significant over-densities can be produced. On the other hand, for very small values of η (large Λ_0) the available reservoir of thermal energy is radiated extremely fast and the medium achieves everywhere its minimum temperature. The simulation then resembles an isothermal simulation of decaying turbulence with a initial *rms* Mach number close to unity. Sánchez-Salcedo et al. (2002) discussed the development of TI in 1D numerical simulations as a function of the parameter η in the presence of forced flows. They showed that TI always takes place when $\eta < 1$ regardless of the forcing strength. In our simulations involving cooling, the driving occurs on large scales and η is smaller than one, thus enabling the development of TI.

The turbulent medium initially fulfills everywhere the Jeans stability criterion. After cooling is turned on, the gas cools preferentially inside the high-density fluctuations which become even more dense due to the large induced pressure gradients (particularly in the case of the smaller values of η). Thus, perturbations evolve in a highly dynamical way. The first significant over-densities (a factor of a few 100) are produced by means of TI. Small condensations disappear either by merging or under the effect of background heating. In the case of a weak cooling (large value of η), the condensations that form do not reach the stage of gravitational collapse, but they continue to cool and condense in order to achieve pressure equilibrium with

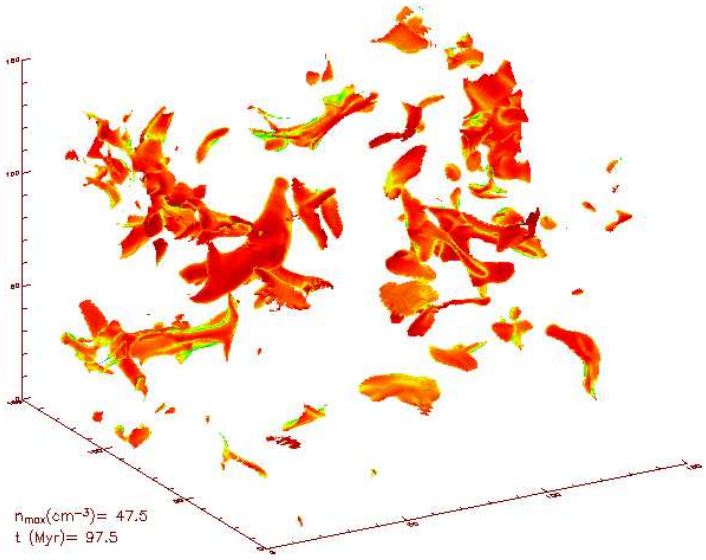

Figure 5.4: Three-dimensional density structure of the medium at t=τ_{dyn} = 97.5 Myrs in model CO09G2. The iso-density surface corresponds to a value of 2 $\bar{n}$. A smaller density threshold has been used in this model because of the lower over-densities reached in this model compared to model CO03G2.

the warmer phase. In the models where TI is efficient (small value of η), some of the most massive clumps become gravitationally bound and begin to contract under the effect of gravity, leading to even denser structures with central densities of a few 10^3cm^{-3}. In a later stage, condensations start merging and form larger condensations which ultimately will end up into a unique dense object. In order to understand the separate effects of TI and GI, we have performed a simulation with $\eta = 0.3$ but without self-gravity (model CO03T2). This simulation evolves in a similar way to model CO03G2 until the point where condensations with central densities of a few 100 cm^{-3} are formed, but these condensations do not merge together. The implications on how these different behaviors could be interpreted from H I observations will be detailed in Section § 5.6. Fig. 5.3 and Fig. 5.4 show snapshots of the density structure at $t = \tau_{dyn} = 97.5$ Myrs after cooling is turned on for models with a strong (CO03G2) and weak (CO09G2) cooling, respectively. Whereas the highest density at $t = \tau_{dyn}$ in model CO09G2 is ~ 50 cm^{-3}, in model CO03G2, the peak density has already reached a value of $\sim 5\times10^3$ cm^{-3}.

We have performed a virial theorem analysis of the condensations at $t = 1$ τ_{dyn} for models CO03G2 and CO09G2. We identified the 40 densest condensations in the simulation box (density thresholds of 15 $\bar{n}$ & 5 $\bar{n}$ have been used for models CO03G2 and CO09G2, respectively) and calculated the virial balance of the clouds following the description given §. 2.3. Fig. 5.5, drawn for model CO03G2, is shown in order to appreciate the importance of including surface energy terms into the virial analysis, as in the specific case of some condensations, they become comparable or even larger than the volume terms. Unless they are bound by gravity, this a clear indication that some of the condensations could be only transient features. Thus our results could be a confirmation of the ideas of Ballesteros-Paredes et al. (1999b) and

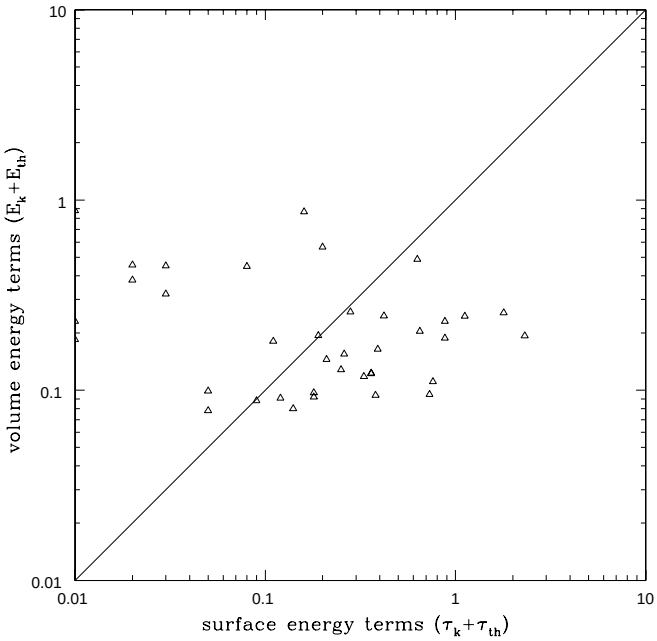

Figure 5.5: Surface versus volume terms entering the virial theorem in the case of simulation CO03G2 at $t = 1\ \tau_{dyn} = 97.5$ Myrs. The 40 densest condensations are considered. The density threshold used is 15 $\bar{n}$.

Ballesteros-Paredes et al. (2003) about the transient nature of some molecular clouds, but for many cloud where the surface terms are dominant, this result could also be interpreted as clouds being in the process of accreating the surrouding gas. In Fig. 5.6 and Fig. 5.7 the gravitational term is compared to the thermal and kinetic energy volume and surface terms. The plots show that at $t = \tau_{dyn}$, most of the condensations in model CO03G2 are dominated by gravity which is not the case in model CO09G2.

5.3 From physical data to observations

The detailed structure in the three-dimensional space can not be compared directly to observations. Rather, observations of large scale structures of the ISM are presented as emission maps in different atomic or molecular lines. The relatively low average density of our simulated medium (0.5 cm^{-3}) will not show up in emission maps of the high density tracers such as CO, CS and N_2H^+ and despite the fact that we have some detectable emission in the CO(1-0) line, the number of cells where this signal can be registered is very small. To make a direct comparison with observations possible, we calculate emission maps in the hyperfine structure line of the neutral hydrogen. This transition occurs for relatively low densities in the range of 0.1-1 cm^{-3}. We assume the number density fraction of hydrogen atoms to be $X = 0.90$. Emission maps in the 21 cm H I line are built by solving the radiation transfer equation along each line of sight,

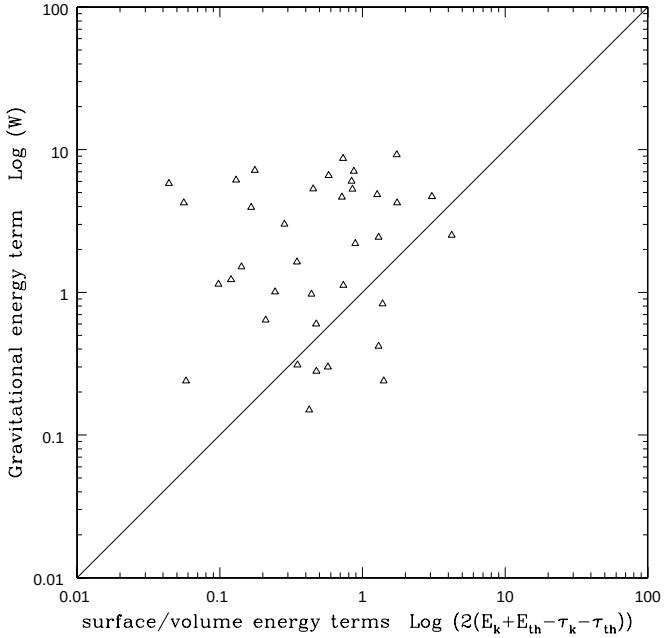

Figure 5.6: Virial theorem analysis for simulation CO03G2 at $t = 1\tau_{dyn} = 97.5$ Myrs for the 40 densest condensations in the box. The density threshold used is 15 $\bar{n}$.

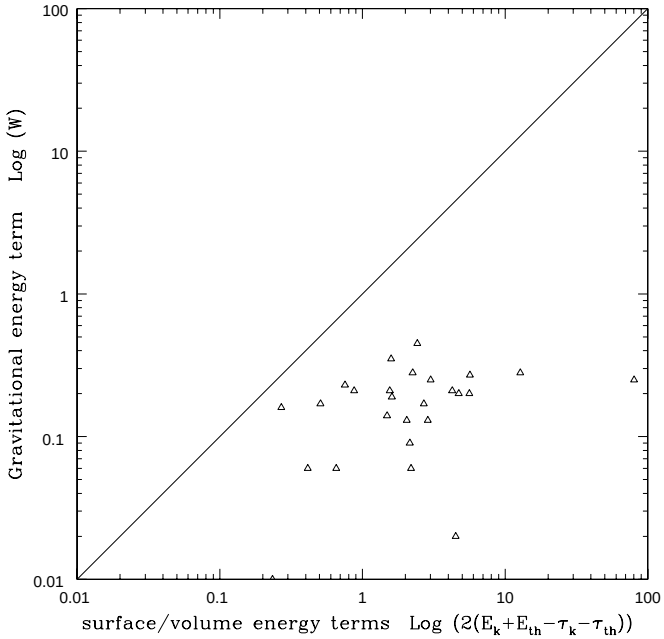

Figure 5.7: Virial theorem analysis for simulation CO09G2 at $t = 1\tau_{dyn} = 97.5$ Myrs for the 40 densest condensations in the box. The density threshold used is 5 $\bar{n}$.

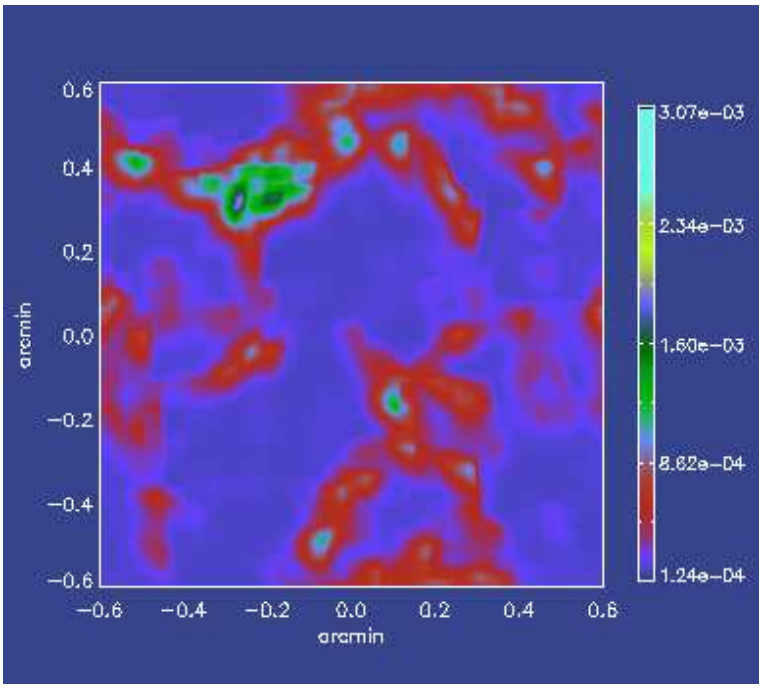

Figure 5.8: 21 cm H I map of the medium at $t = \tau_{dyn} = 97.5$ Myrs for model CO03G2. The value of the intensity is given in Jansky.

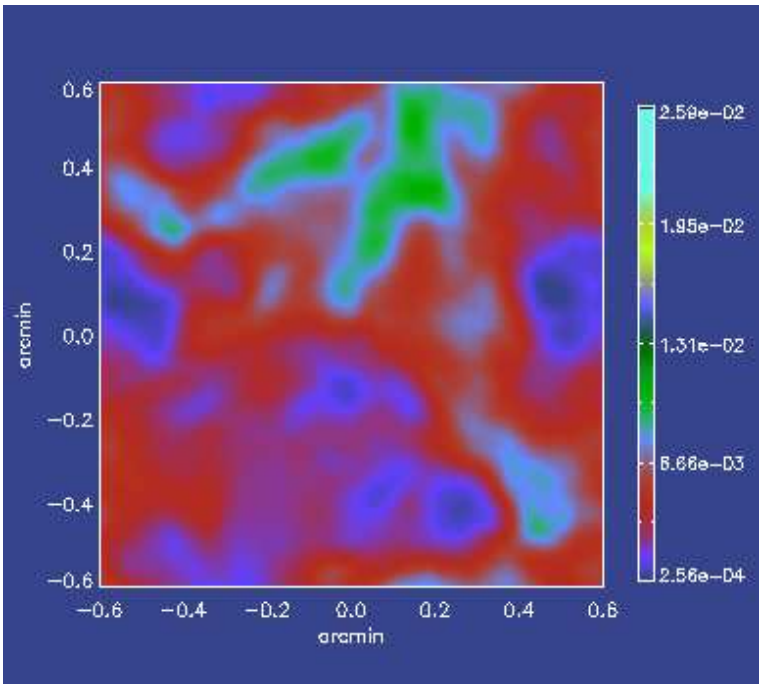

Figure 5.9: 21 cm H I map of the medium at $t = \tau_{dyn} = 97.5$ Myrs for model CO09G2. The value of the intensity is given in Jansky.

$$\frac{dI_\nu}{ds} = \kappa_\nu (S_\nu - I_\nu), \tag{5.1}$$

where I_ν is the intensity at the considered wavelength, S_ν is the source function which is assumed to be a blackbody radiation function with a temperature defined by the local temperature of each cell, and ds is the differential distance element along the line of sight. κ_ν stands for the absorption coefficient of the line. I_ν is determined by :

$$I_\nu = I_0 e^{-\tau_{\nu,tot}} + \int_0^{\tau_{\nu,tot}} B_\nu e^{-\tau_\nu} d\tau_\nu, \tag{5.2}$$

and

$$\tau_\nu = \int_s^\infty \kappa_\nu ds \tag{5.3}$$

where τ_ν is the value of the local optical depth for the considered frequency and $\tau_{\nu,tot}$ is the total optical depth integrated along the box length. On our discrete grid, the integration in Eq. 5.2 is replaced by a summation, running over all the cells along the line of sight. In the general case, the absorption coefficient, κ_ν can be described by

$$\kappa_\nu = \frac{A_{ij} c^2}{8\pi\nu^2} \frac{g_i}{g_j} \left[1 - exp\left(-\frac{h\nu}{k_B T}\right)\right] n_j \phi(v), \tag{5.4}$$

where A_{ij} is the Einstein transition coefficient when the local density exceeds the threshold density for excitation and which is zero if the density is less then this threshold. We choose a value for this threshold density[1] of 0.5 cm^{-3}. n_j is the number density of the atoms in the upper level j. $\phi(v)$ is the line profile, which is assumed to be thermal. In the particular case of the 21 cm H I line, Eq. 5.4 can be simplified by replacing the exponential term by the first two terms of the Taylor expansion (Rohlfs & Wilson 1996) such that

$$\kappa_\nu = \frac{3c^2}{32\pi} \frac{1}{\nu_{10}} A_{10} n_H \frac{h}{k_B T} \phi(v), \tag{5.5}$$

where n_H is the neutral hydrogen number density and is given by $n_H = X n_{tot}$ where n_{tot} is the total number density of the gas. The Einstein transition coefficient and the frequency of the 21 cm H I line are given by A_{10}=2.86888 $\times$ 10^{-15} s^{-1} and ν_{10}=1.420405751786 $\times$ 10^9 Hz, respectively. $\phi(v)$ is given by

$$\phi(v) = \frac{c}{\nu_{10}} \left(\frac{m_H}{2\pi k_B T}\right)^{1/2} exp\left[-\frac{m_H v^2}{2k_B T}\right] \tag{5.6}$$

where m_H is the mass of the hydrogen atom. The two-dimensional intensity obtained after solving for Eq. 5.2 is the intensity at the surface of the data cube. In order to mimick observational 21 cm H I line maps, we still need to apply two corrections. The first one consists in convolving the result obtained by means of Eq. 5.2 with a function G which represents the radio telescope response. For simplicity, we mimick observations with a single

[1]The value of the critical density in Rohlfs and Wilson (1996) is 1 cm^{-3}, but observations in the H I 21 cm line suggest that this value could be smaller (Muller et al. 2003), as they could infer densities of 0.06 cm^{-3}. Thus, the value of 0.5 cm^{-3} should be regarded as a characteristic value.

dish radio telescope and we describe G by a two dimensional Gaussian function as displayed in Eq. 5.7 and Eq. 5.8.

$$I_{\nu,o} = I_\nu \otimes G \tag{5.7}$$

and

$$G = \frac{1}{2\pi\sigma^2} exp\left[-\frac{N_x^2 + N_y^2}{2\sigma^2}\right], \tag{5.8}$$

The standard deviation σ of G is linked to the beam size BS through the relation $BS = 2\sqrt{2 \times ln2}\sigma$. The beam size is in turn fixed by the radio telescope's resolution R and the angle Φ under which each cell is viewed such that $BS = R/\Phi$. Φ is given by the relation $\Phi = L_b/(ND)$ where L_b is the physical size of the simulation box and N the number of cells in one dimension. D is the distance to the box (i.e., to Ho II). D is fixed at a value of 3.38 Mpc (Karachentsev et al. 2002). We also set R such that it represents a resolution of $4.5''$/pixel which is the resolution of the high resolution H I map of Puche et al. (1992) to which we intend to compare our results. N_x and N_y are defined as the number of grid cells present in the beam in each direction. They are obtained by dividing the beam size BS by the angular size of one cell and in our case they are equal. The number of cells we have in the beam in each direction is $N_x = N_y = 9$ which corresponds to a smoothing length value of 9×7.8=70.2 pc. The smoothing length in the high resolution map of Puche et al. (1992) is ~ 73 pc. Hence the beam size values in our simulations and in the observational map are quite similar. The second effect is the geometrical dilution of the intensity. The intensity at the distance D is equal to the intensity at the surface, multiplied by a dilution factor $w = \Omega/2\pi \approx L_b^2/(2N^2D^2)$, where Ω is the solid angle which sustains one cell. One should also mention that because of the convolution, the smoothing of pixels which lie at the edges of the intensity map can be incorrect as they have no counterparts in all directions. We solve this problem by duplicating our map nine times and aligning the copies such that they form a $3N \times 3N$ map on which we perform the convolution. Afterwards, we truncate $N \times N$ pixels inside the actual map to recover a smoothed complete $N \times N$ pixels map.

5.4 The observable quantity

The algorithm described in § 5.3 has been applied to our simulations to compute the corresponding 21 cm H I intensity maps. Examples of maps from two snapshots in two different models (i.e., Fig. 5.3 and Fig. 5.4) are displayed in Fig. 5.8 and Fig. 5.9, respectively. The value of the intensity is given in Jansky and a background intensity I_0 of 10^4 Jansky is assumed. The maps at $t = \tau_{dyn} = 97.5$ Myrs show a structured distribution in the 21 cm line in the form of shells and holes similar to the observations (e.g., Fig. 1.3 and Fig. 1.2). The stronger pressure gradients at the interfaces of the dense clouds in models with more efficient cooling (smaller values of η) lead to more compact filaments and shells in the three dimensional structure which is also seen in the 21 cm H I maps. In order to quantify the comparison between the models and the observations, we calculate the autocorrelation function, which is defined as follow,

$$S_2(\Delta x, \Delta y) = \frac{\sum_{i,j}^{L}(I_{\nu,o}(i,j) - \overline{I_{\nu,o}})(I_{\nu,o}(i+\Delta x, j+\Delta y) - \overline{I_{\nu,o}})}{\sum_{i,j}^{L}(I_{\nu,o}(i,j) - \overline{I_{\nu,o}})^2} \tag{5.9}$$

where $\overline{I_{\nu,o}}$ is the average value of the intensity and Δx and Δy represents the distance of cells in both directions. There are different ways to deal with the cases when the distance $\Delta L = \sqrt{\Delta x^2 + \Delta y^2}$ extends beyond the box (or sub-box) edges in either directions. One could assume, at every scale, a self-periodicity of the H I map in every direction. However, this is not physically justified. The ideal treatment would be to use for each box (or sub-box) its natural neighbors for the calculation of the autocorrelation length. Such an approach would be favorable to small scales where natural boundary pixels are available but would still imply a self-periodicity for the large scales. We took the option of treating all scales equally, by using in the calculation of S_2 only those pixels which reside inside the box at the given scale. The price of such an approach, though it yields more consistent results, is to increase the statistical error bars since a smaller number of pixels is involved in the calculation of S_2 at the larger scales. S_2 has a maximum of $S_2 = 1$ for $\Delta L = 0$ and drops for larger scales. The characteristic value of the autocorrelation length L_{cr} can be reasonably defined as being the physical scale for which the autocorrelation function has dropped substantially below 1. We choose L_{cr} to be the value of the length scale when S_2=0.2. The autocorrelation length is then defined as the average of the three autocorrelation length values derived from H I maps calculated for the three projections of the simulation box. Houlahan and Scalo (1990) pointed out to the fact that the estimate of S_2 on small scales might be affected by structures with characteristic scales that are larger than the box size. this indeed may happen for some of the smaller boxes, if a box with the smallest size we consider (125 pc) is centered on a condensation which is larger. In that case the estimate of L_{cr} might be dominated by the self terms and would not be accurate. However, on those small scales (125 pc), we calculate, at each time step, the value of L_{cr} $8 \times 8 \times 3 = 92$ times on independent sub-boxes and many of those sub-boxes are not centered on dense condensations which happen to be larger than them. So due to the large statistics, we are confident that we pick up the signature of cross terms (undoubtedly always affected by the self terms) even on the smallest scales we consider.

5.5 The physical size-correlation length relation in Ho II

In order to check the validity of the comparison of L_{cr} on a particular scale between the observations and the synthetic maps, the dependence of L_{cr} on the size L of the analyzed region must be checked in Ho II. For a given scale L, we subdivide the observed H I map of Ho II in side by side boxes, each of size L, excluding pixels within a distance L from the edges of the map to avoid contamination by the outer pixels which might not belong to Ho II. For larger scales, we additionally consider squared regions that are shifted by a third of the box size in order to increase the number of boxes on which we evaluate L_{cr}. The characteristic autocorrelation length at a given scale is calculated by averaging the individual values. The error is simply assumed to be the standard deviation with respect to the average value at the considered scale. The $L - L_{cr}$ relation we find for Ho II is displayed in Fig. 5.10. It shows a linear growth of L_{cr} with L up to a scale of ~ 6 kpc and, for larger scales, a nearly constant value, independent of the physical scale. The shape of the $L - L_{cr}$ relation suggests that the structure is correlated for scales less than ~ 6 kpc. On larger scales, structures in different regions seem to form independently. The relationship between the position of the turnover

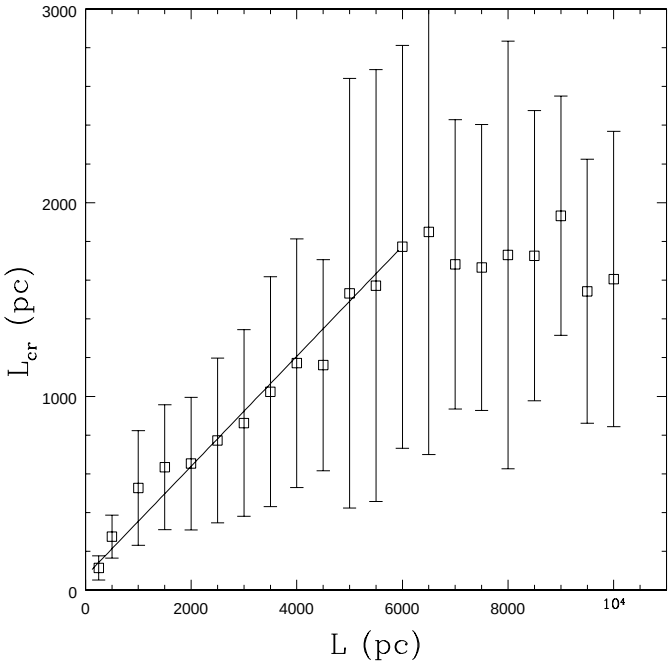

Figure 5.10: Physical size-correlation length relation in Holmberg II.

point in the $L - L_{cr}$ relation and the length scale of the driving mechanism as well as the value of the slope in the linear regime is what we attempt to explore in the next section using comparisons between the observed and simulated H I maps of Ho II. For the $L - L_{cr}$ relation in Ho II, a linear fit to the data points for scales ranging between 0.25 kpc and 6 kpc yields a slope of 0.284 ± 0.061 (i.e., fit over-plotted to the data in Fig. 5.10).

5.6 Comparing the models with the observations

5.6.1 Comparison to the isothermal models

We first analyze the set of isothermal models in which the turbulence is driven at different length-scales and at different Mach numbers. These are labeled ISOimj in Table. 1, where i stands for the wavenumber on which the energy is injected and j the Mach number. The purpose of these simulations is to check if the observed H I hole- and shell like structure can emerge as a result of turbulence alone. Fig. 5.11 shows the $L - L_{cr}$ relations derived for models ISO2m1 and ISO4m1. The over-densities $\delta\rho/\rho$ created locally by converging flows do not exceed the value of 3 in these simulations which are characterized by a Mach number $Ma = 1$. The values of L_{cr} are obtained by averaging over time for time dumps between τ_{dyn} and $2 \times \tau_{dyn}$ (after a steady statistical status of the system is obtained; i.e. similar probability distribution functions) and the three dimensions of the simulation box. In these simulations the turbulence is driven with a wave number of $k = 2$ and 4, respectively (i.e., L_{driv} of 0.5 kpc and 0.25 kpc, respectively). In both models, the $L - L_{cr}$ relation shows a linear increase of L_{cr} with L up to a scale which is equal to L_{driv}. For scales larger then L_{driv} the $L - L_{cr}$ relation nearly flattens. The turnover point in the $L - L_{cr}$ relation seems to be associated

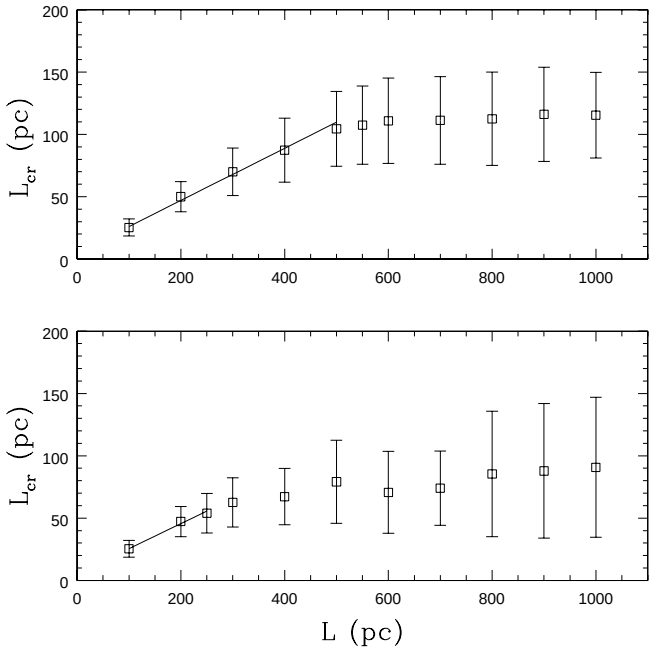

Figure 5.11: $L - L_{cr}$ relation in models ISO2m1 (top) where the driving length-scale is 0.5 kpc and ISO4m1 (bottom) with a driving length-scale of 0.25 kpc.

with the scale of the driving mechanism. Therefore, it can only show up if L_{cr} is calculated from small scales up to scales that are larger than L_{driv}. A comparison of the models and the observations at a given scale is meaningful, only if that scale lies below the turning point of the $L - L_{cr}$ relation both in the models and the observations (unless the position of the turning point in the simulations and the observations is equal). In practice, this is equivalent to comparing the slopes of the $L - L_{cr}$ relations below the turning point. A small increase in L_{cr} is still visible with increasing scale. This is probably due to the presence of a non zero upward energy cascade which distributes some of the injected energy on scales larger than L_{driv}. The direct comparison of Fig. 5.10 to Fig. 5.11 implies that energy is injected into the ISM of Ho II on a scale of the order of ~ 6 kpc. This clearly favors a large-scale driving rather than a driving by supernova explosions. The kinetic energy power spectrum drawn by Stanimirović and Lazarian (2001) for the Small Magellanic Cloud (SMC) speaks for a large scale driver operating in the SMC as well. The spectrum shows no signs of energy injection up to the largest scale they have considered (4 kpc). The linear regime below the turning point is governed by the energy decay of the turbulence from large to small scales. Thus, the slope of the $L - L_{cr}$ relation in that regime is indication of the gas equation of state. A linear fit to the $L - L_{cr}$ data for scales smaller or equal to L_{driv} in models ISO2m1 and ISO4m1 yields a slope of 0.209 ± 0.052 and 0.201 ± 0.096, respectively. This is a factor ~ 1.4 smaller than the value yielded by the observations and is probably an indication that the hypothesis of isothermal gas is not entirely valid.

We now check if these conclusions still hold when turbulence is driven at different *rms* Mach

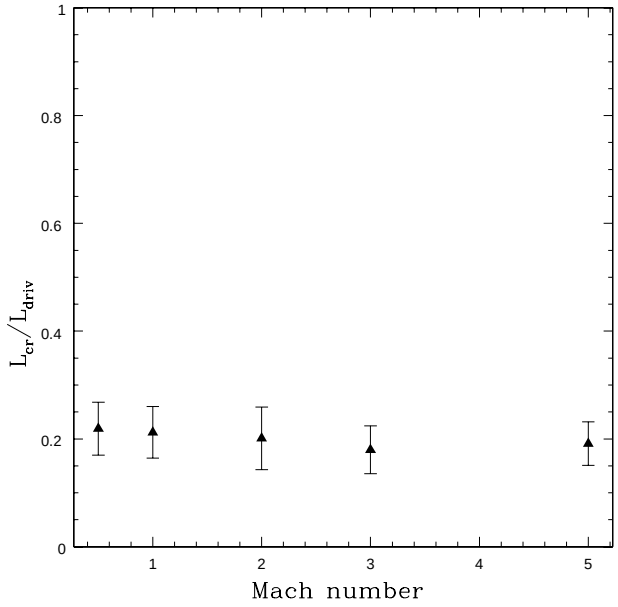

Figure 5.12: Dependence of the autocorrelation length on the *rms* Mach number in the isothermal simulations. The driving wave number in these simulations is $k = 2$ ($L_{driv} = 0.5$ kpc).

numbers. We compare the observations to models ISO2m05, ISO2m1, ISO2m2, ISO2m3 and ISO2m5 where turbulence is driven with Mach numbers of 0.5, 1, 2, 3 and 5, respectively. In these simulations turbulence is driven with a wave number $k = 2$ ($L_{driv} = 0.5$ kpc) and thus, a comparison of these models to the observations is performed at the 0.5 kpc scale. Fig. 5.12 shows that the autocorrelation length remains independent of the strength with which turbulence is driven.

5.6.2 Comparison to the models with cooling and heating

We now turn to more realistic models where the cooling and the heating of the gas are present, as well as self-gravity. We should mention that the purpose of this section is not to recover the precise structure of the gas in Ho II, but rather to show qualitatively the importance of the combined effects of turbulence and the gas thermodynamics in generating the observed structures. The models have the ratios of the cooling time to the dynamical time of $\eta = 0.3, 0.6$ and 0.9 (strong, intermediate and weak cooling). In these simulations turbulence is driven with $k = 2$ ($L_{driv} = 0.5$ kpc) and the comparisons to the observations are performed at the scale of 0.5 kpc. The advantage of comparing the autocorrelation length on the 0.5 kpc scale is that a large number of independent 0.5 kpc^2 squares can be selected from the H I map of Ho II (we select 80×80 0.5 kpc^2 squares), thus enhancing the accuracy of the observed value at this scale. Though the observed value is only an estimate of the characteristic autocorrelation length at the time of the observations and although the holes and shells are continuously interacting, the selected sample is large enough to consider the observed value at the 0.5 kpc scale $L_{cr,0.5} \sim 142$ pc as a realistic stable value. Due to the non-

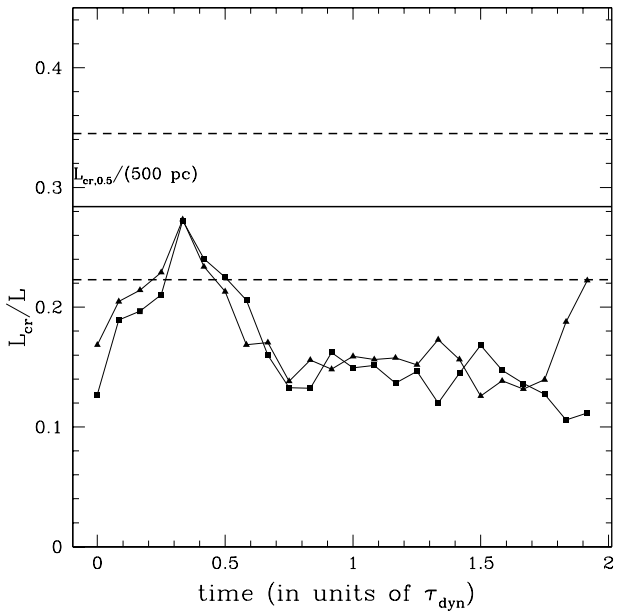

Figure 5.13: A comparison of the time evolution of the autocorrelation length at the scale of 0.5 kpc between two models with self gravity (model CO03G2, full triangles) and without self-gravity (model CO03T2, full squares).

linear evolution of structures under cooling and gravity, a time average for the value of L_{cr} is not meaningful, as it could smear out the true behavior of the gas. In order to distinguish the effects of TI and GI on the large scale structure as it would appear in the H I map, we compare two models with the same cooling rate ($\eta = 0.3$) but with and without self-gravity (models CO03G2 and CO03T2, respectively). Fig. 5.13 shows that the evolution of L_{cr}/L_{driv} is nearly similar in both models until $t \sim 1.7\ \tau_{dyn}$, despite the fact that in the case of the run with gravity, the condensations that form following the early condensation process by TI are a few order of magnitude denser than in the case without self-gravity. Only when the larger and denser condensations start accreting the smaller ones, L_{cr}/L_{driv} rises again. This indicates that the observed plateau in L_{cr}/L_{driv} between $t \sim 0.7\ \tau_{dyn}$ and $t \sim 1.7\ \tau_{dyn}$ is a signature of TI alone.

Fig. 5.14.a compares the time evolution of the ratio L_{cr}/L_{driv} in models with different values of η, with all these models having self-gravity included. In contrast to the above discussed high efficiency cooling case, the autocorrelation length derived from the model with $\eta = 0.9$ (weak cooling, model CO09G2) is in good agreement with the observational value within the 1 σ error bars, and this over a span of time which is $\sim 1.5\ \tau_{dyn} \sim 150$ Myrs. This is comparable to the age of the oldest ($\sim$ 135 Myrs) holes observed in Ho II when considering the sample of Rhode et al. (1999) of holes that do not host any remnant stellar cluster. Fig. 5.14.b shows the $L - L_{cr}$ relation for model CO09G2 at $t = 1.5\ \tau_{dyn}$. The slope in the linear regime is 0.243 ± 0.045. In this model, the density in the densest clumps is only a few times larger than the average density. Here cooling is complementary to turbulence. When holes are created by turbulence, TI tends to enlarge them under the effect of the local pressure gradients at their

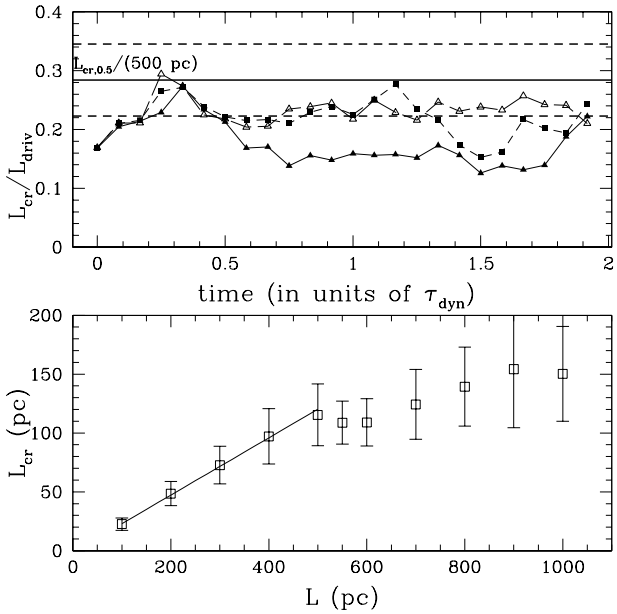

Figure 5.14: a) (top) Time evolution of the autocorrelation length in models with cooling and gravity. the models are CO03G2 (full triangles), CO06G2 (full squares) and CO09G2 (open triangles). b) (bottom) $L - L_{cr}$ relation in model CO09G2 plotted at $t = 1.5\ \tau_{dyn}$.

boundaries. The curve corresponding to $\eta = 0.6$ (model CO06G2) shows a good agreement with the observations for a time span of 0.8 $\tau_{dyn} \sim 80$ Myrs. The system condenses further and L_{cr}/L_{driv} drops to intermediate values between those of the high efficiency and week efficiency cooling until it reaches the stage of condensation-condensation accretion and the L_{cr}/L_{driv} value increases again. Yet, the evolution of the H I morphology if star formation occurs can not be followed with our models. However, the low star formation rate (SFR) of Ho II estimated to be in the range 0.00084-0.049 $M_\odot$ yr^{-1} (Hunter and Gallagher 1985; Stewart et al. 2000) suggests that many of the condensations that form due to TI are probably destroyed before they can form stars, possibly by the galactic shear[2] or other processes. This argues against strong cooling which tends to forms stars more efficiently and which imprints a smaller L_{cr} value to the H I morphology.

5.7 Conclusions and discussion

In this work we have compared 21 cm H I simulated maps to the high resolution H I map of Puche et al. (1992) of the dwarf irregular, gas rich galaxy Holmberg II (Ho II). The maps are built by using a post processing of the radiative transfer equations on different models of 1 kpc scale local three-dimensional hydrodynamical simulations. After mimicking the same spatial resolution in the simulated maps than the one used in the observations, we perform a

[2]The galactic shear is however not very strong in Ho II. Using the velocity curve of Bureau and Carignan (2002) we could estimate that, at the radii of 15 kpc, galactic shear acts on a timescale of $\sim 2 \times 10^9$ which is larger than the age of the observed H I holes.

quantitative comparison between the models and the observations using the autocorrelation length. The autocorrelation length-physical scale relation ($L - L_{cr}$ relation) shows, both in the observations and simulations, two regimes. For scales smaller than the scale of the energy injection L_{driv}, L_{cr} shows a linear increase with L and flattens for scales larger than L_{driv}. This is confirmed by a comparison of the observations to maps derived from the simulations driven at different length scales. The $L - L_{cr}$ relation of Ho II implies that energy is injected into the ISM of the galaxy on a scale of $\sim$ 6 kpc. This clearly favors a large-scale driving rather than a driving by supernova explosions. The kinetic energy power spectrum drawn by Stanimirović and Lazarian (2001) for the Small Magellanic Cloud (SMC) speaks for a large scale driver operating in the SMC as well. The spectrum shows no signs of energy injection up to the largest scale they have considered (4 kpc). The slope of the $L - L_{cr}$ relation seems to be related to the gas physics and the mode of energy decay from L_{driv} down to the smaller scales. Our results show that the slope of the $L - L_{cr}$ relation in the linear regime can be reproduced when turbulence is coupled to a weak cooling of the gas.

Wada et al. (2000) have shown, in the case of the LMC, that thermal and gravitational instabilities lead to the formation of a network of shell and hole-like structures in the ISM, however, they did not perform a quantitative comparison between their models and the observations in terms of the H I structure. Our new approach can be applied to the ISM in different galaxies in order to 1) constrain the global cooling rate of the galaxy which is connected to the slope of the $L - L_{cr}$ relation in the linear regime and most important, 2) to estimate the physical scale on which the energy is injected into the medium by the position of the turning point in the $L - L_{cr}$ curve. In a subsequent work, using a three-dimensional global model for dwarf irregular galaxies, the relationship that might exist between the $L - L_{cr}$ relation slope in the linear regime and the metallicity of the gas shall be explored.

Regarding the energy requirement of the driver, we have injected into our simulation box $\sim 1.1 \times 10^{50}$ ergs Myrs^{-1} kpc^{-3}. Summing the kinetic energy derived by Puche et al. (1992) (based on kinetic energy input estimates using the model of Chevalier 1974), normalizing that energy input to the age of the oldest hole in Ho II (in time units of Myrs) and dividing by the volume of the galaxy yields a value of $\sim 7.3 \times 10^{48}$ ergs Myrs^{-1} kpc^{-3}. This implies that the supernova scenario applied to Ho II underestimates by a factor of $\sim$ 15 the required energy for the holes formation. The estimates of Puche et al. (1992) might underestimate the number of supernova explosions in each hole. This would lead to larger remnant stellar clusters than those already expected, but not found, in the H I holes of Ho II (Rhode et al. 1999). The energy balance argument tends to confirm our conclusions that supernova explosions are not responsible for the formation of all of the observed H I holes in Ho II.

The natural continuation of this work is to investigate what are the eventual large scale drivers operating in Ho II. In the absence of large scale supernova driving, spiral density waves could constitute a plausible driving candidate. However, Ho II does not show any developed spiral pattern. Another possibility is that Ho II, by infalling to the center of the M81 group and weakly interacting with its neighboring galaxies, might be undergoing a process of ram pressure stripping in the intra-group medium of this group (Bureau and Carignan 2002) and/or tidal stripping by it's closest neighbors. These scenarios could be confirmed by running combined N-Body/SPH simulations of interacting galaxies while including the intergalactic medium gas. Such simulations should be made possible by using new hybrid

N-Body/SPH codes like VINE which is currently under development (Wetzstein et al., in preparation). Another possibility to drive turbulence on large scales could be offered by the magneto-rotational instabilities (MRI) that could take place in the outer parts of the galactic disk of Ho II (Balbus and Hawley 1991, Selwood and Balbus 1999). However, first simulations of the MRI in the galactic context as a plausible turbulence driver are not very encouraging (see § 1.2.2). We should finally mention that the scenario discussed in this paper does not necessarily rule out that H I holes can also be formed, in other dwarf galaxies, as a result of multiple supernova explosions as discussed by Sánchez-Salcedo (2002) in the case of the nearby dwarf galaxy IC 2574 (Walter and Brinks 1999).

Chapter 6

Supernova driven turbulence

6.1 Introduction

As already discussed in Chap. 1, it is now a well established fact that the interstellar medium (ISM) in galactic disks is turbulent (Larson 1981; Scalo 1987; Dickey and Lockman 1990). In most spiral galaxies, and after correcting for instrumental effects, the vertical velocity dispersion is observed to vary radially from $\sim 12 - 15$ km s^{-1} in the central parts to $\sim 4 - 6$ km s^{-1} in the outer parts (van der Kruit and Shostak 1982 for NGC 3938; Shostak and van der Kruit 1984 for NGC 628; Dickey et al. 1990 for NGC 1058; Kamphuis and Sancisi 1993 for NGC 6964; Rownd et al. 1994, for NGC 5474 and Meurer et al. 1996, 1994 for NGC 2915). In most cases, the latter values exceed the values expected by the thermal broadening effect of the emission and absorption lines. As an example, the radial dependence of the velocity dispersion in NGC 1058 is shown in Fig. 6.1. Fig. 6.2 shows the behavior of the characteristic velocity dispersion of a galaxy when plotted versus its star formation rate. The galaxies shown in Fig. 6.2 correspond to a sample where both the velocity dispersion and star formation rate were available in the literature. These velocity dispersions correspond to transonic to subsonic random motions in the cold and warm neutral medium and to supersonic random motions in dense and cold molecular clouds. As discussed in Chap. 1, many physical processes might contribute to the driving of the turbulence in the ISM. These processes include magneto-rotational instability (MRI) (Balbus and Hawley 1991) and gravitational and thermal instabilities (Wada and Norman 1999, 2001, Wada et al. 2000) or a combination of large scale perturbations coupled to local thermal and gravitational instabilities (Dib and Burkert 2004b; Dib and Burkert 2004a; Chap. 5). Wada et al. (2002) showed, using high resolution two-dimensional simulations of a galactic disc, that the turbulent energy spectra can be maintained in a quasi-stationary state even in the absence of stellar feedback. In the simulations of Wada et al. (2002) the kinetic energy decay and radiative cooling are compensated by the interaction of the galactic shear with the gas self-gravity.

Another major source of energy input into the ISM is the stellar energy feedback, particularly from massive stars. The latter can be delivered to the ISM in the form of ionizing radiation and stellar winds from O and B stars and from clustered or field supernova (SN) explosions (Kessel-Deynet and Burkert 2003; Mac Low and Klessen 2004). On one hand, Mac Low and Klessen (2004) showed, using simple analytical arguments, that the global energy input into the ISM from SN explosions is at least two orders of magnitude larger than from any

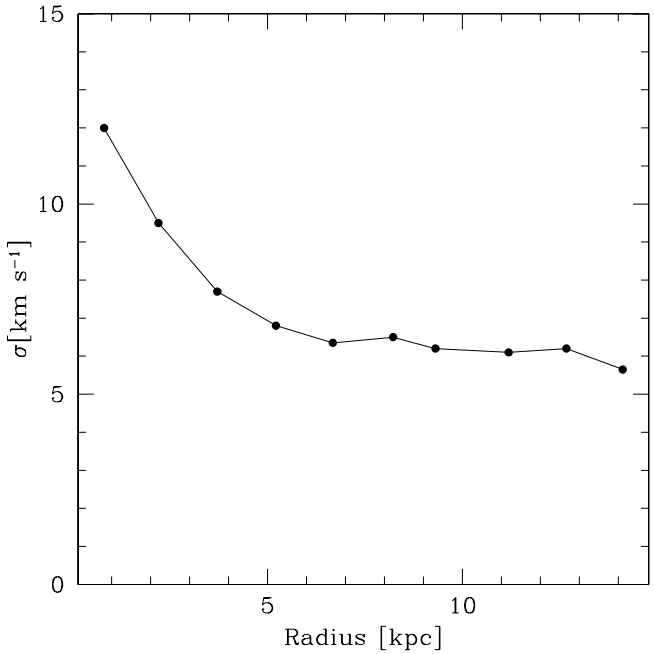

Figure 6.1: Radial dependence of the velocity dispersion in NGC 1058. Adapted from Dickey et al. (1990) (Fig. 3 in their paper), assuming a distance of 10.2 Mpc (Boroson 1981).

other process (see Chap. 1 for details). On the other hand, the observations of Rhode et al. (1999) and the numerical models of Dib and Burkert (2004a,b) (Chap. 5) show that the SN explosions based scenario can not explain the large scale structures observed in the 21 cm H I line in galaxies where star formation does not play a significant role such as the Small Magellanic Cloud (SMC) and Holmberg II (Ho II). In the case of Ho II, we have identified that the energy is injected into the ISM on a scale of $\sim$ 6 kpc, which is much larger than the scale implied by SN driving. Furthermore, Sellwood and Balbus (1999) (hereafter SB99) argue that, in contrast to the inner parts of galactic disks where driving of turbulence by SN explosions is likely to prevail, the constancy of the velocity dispersion in the outer H I layer of galaxies such as NGC 1058 can also be the result of a driving mechanism in which energy is extracted from differential rotation by ways of the MRI (Balbus and Hawley 1991) or from the $T_{R\Phi}$ Maxwell stress in the case of strong magnetic fields. In the scenario described in SB99, a velocity dispersion of $\sim$ 6 km s^{-1} is obtained when the value of the magnetic field is $\sim 3\mu$G (Eq. 18 in their paper). The main argument of SB99 against a SN-driven ISM, at least in the extended H I layer of NGC 1058, in addition to the fact that column densities are low and star formation is inefficient in the external parts of the galaxy, is the observed uniformity of the H I velocity dispersions (Dickey et al. 1990) whereas H II regions in NGC 1058 are primarily observed in narrow spiral arms (Ferguson et al. 1998). Simulations by Dziourkevitch et al. (2004) show that some amount of turbulent motions can be created by the MRI in galactic disks. However, the MRI turbulence is mostly located in the inner parts of the disk (in their simulations in the inner 1 kpc of the disk) where galactic shear is stronger and the velocity dispersion does not exceed a value of 3.5 km s^{-1} dropping quickly to very

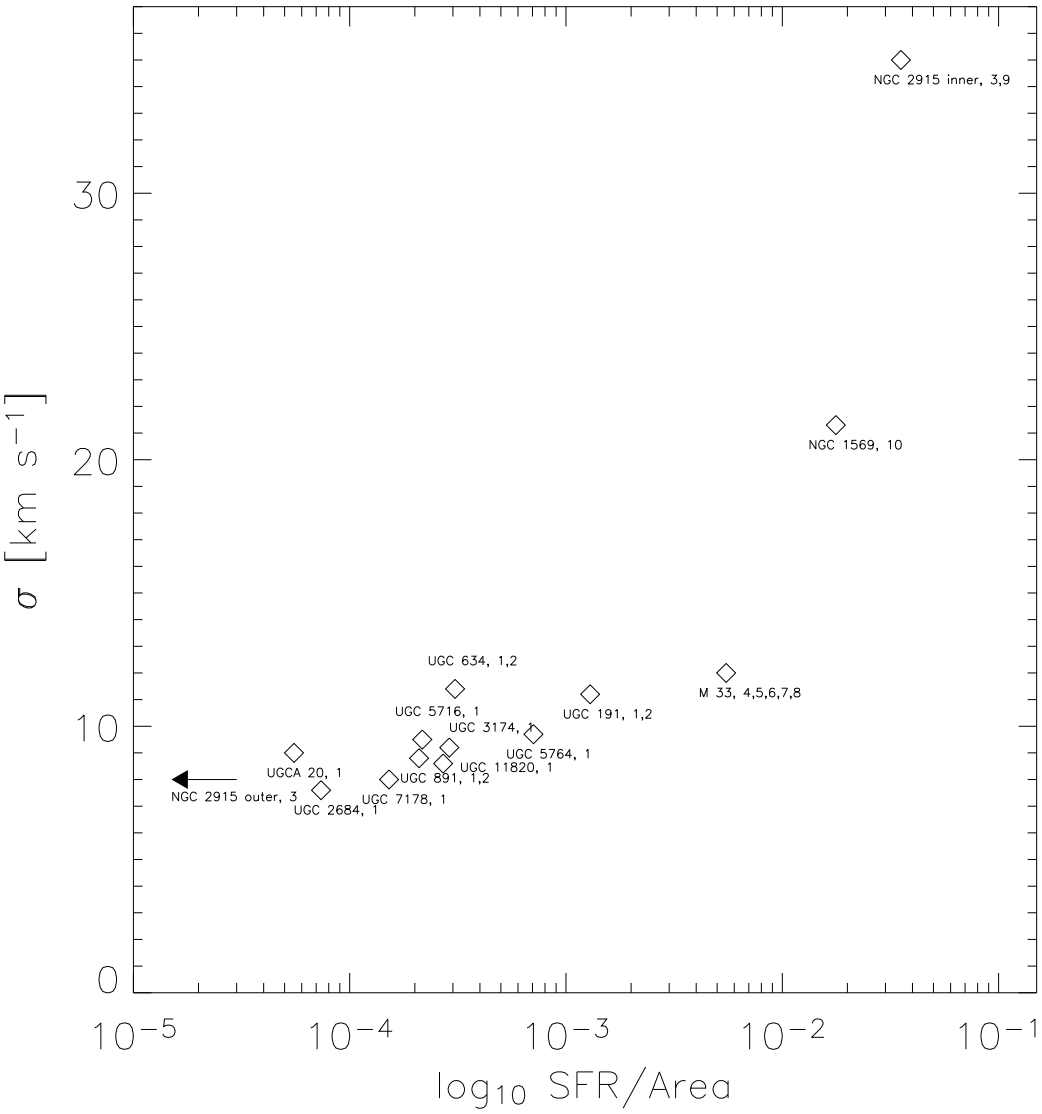

Figure 6.2: Characteristic velocity dispersion σ of a sample of galaxies as a function of the surface averaged star formation rate (units of $M_\odot$ yr^{-1} kpc^{-2}). The galactic surface is calculated as being π $(3\ r_d)^2$, where r_d is the radial length scale of each galaxy. References are (1) van Zee et al. (1997) (2) van Zee (2001) (3) Meurer et al. (1996) (4) Huchtmeier (1973) (5) Gordon (1971) (6) de Jager and Davies (1971) (7) Hippelein et al. (2003) (8) Elmegreen and Elmegreen (1984) (9) Meurer et al. (1994) (10) Stil and Israel (2002).

small values at larger radii. Furthermore, recent simulations show that the MRI might be completely suppressed/overwhelmed by star formation in galactic disks (M. Korpi, private communication).

The aim of the work presented in this chapter is to assess how much of the velocity dispersion observed in the ISM of galaxies is due to SN feedback for various values of the SN rate and feedback efficiency. A particular point of interest is to understand the constancy of the velocity dispersion in spiral galaxies at different radii where the star formation rate is expected to decrease with increasing radius from the galactic center (Schmidt 1959; Kennicutt 1998; Dopita and Ryder 1994; Prantzos and Silk 1998). Over the past decade, two and three-dimensional numerical models of SN explosions models in the ISM have been presented in the literature (Rosen and Bregman 1995; Korpi et al. 1999a,b; de Avillez 2000 and Kim et al. 2001). In these models, the authors have focused on problems like the evolution of SNe bubbles and their outburst through the galactic disk, the halo-disc interaction, the vertical scale height, volume filling factors of the different gaseous phases and the effects of supernova explosions on the Galactic dynamo (Ferrière 1992a,b, 1998a,b; Ferrière and Schmitt 2000). However, the existence of a correlation between the SN rate and the velocity dispersion of the gas has not been investigated so far and this is what we investigate in this work. This chapter is organized as follows. In § 6.2, we describe our models and the relevant parameters. In § 6.3, we describe how synthetic observations are derived. The velocity dispersion dependence on the feedback efficiency and supernova rate is presented and discussed in § 6.4 and § 6.5, respectively. in § 6.6 the need for improved numerical models is critically reviewed and in § 6.7, we summarize our results and conclude.

6.2 The model

In order to understand how the SN rate and energy feedback efficiency affect the velocity dispersion of the gas, we resort to a simple numerical model in which the vertical stratification, galactic rotation, magnetic fields and the gas self-gravity are not included. Using the ZEUS-3D code (Stone and Norman 1992a,b; § 2.2) we simulate a 1 kpc^3 volume of the ISM with a grid resolution of 128^3. Periodic boundary conditions are imposed in the three directions. In most simulations and if not specified otherwise, the initial density field is homogeneous with a number density of $\bar{n} = 0.5$ cm^{-3}. The velocity and temperature are everywhere zero and 10^4 K, respectively. A polytropic equation of state with a specific heat ratio of 5/3 is used. This proves to be justified by the fact that over-densities only of the order of a few tens of cm^{-3} are able to form in most of the simulations; therefore the gas remains mostly monoatomic. We include radiative cooling of the gas using the solar metallicity cooling curves of Dalgarno and McCray (1972) in the temperature range of [100 K,10^4 K] and of Sutherland and Dopita (1993) for the temperature range of [10^4 K-$10^{8.5}$ K]. The gas is not allowed to cool below the minimum temperature $T_{min} = 100$ K. The maximum temperatures at the explosion sites reach values of $\simeq 60 - 70 \times 10^6$ K which makes the hot gas fall in the hot stable regime. The adopted cooling curve is displayed in Fig. 6.3.

Stellar feedback is modeled as resulting from type II SN explosions only and the energy is injected into the ISM instantaneously. The total energy of each explosion is taken to be $E_{SN} = 10^{51}$ erg (Chevalier 1977; Abbott 1982; Woosley and Weaver 1986; Heiles 1987). Only

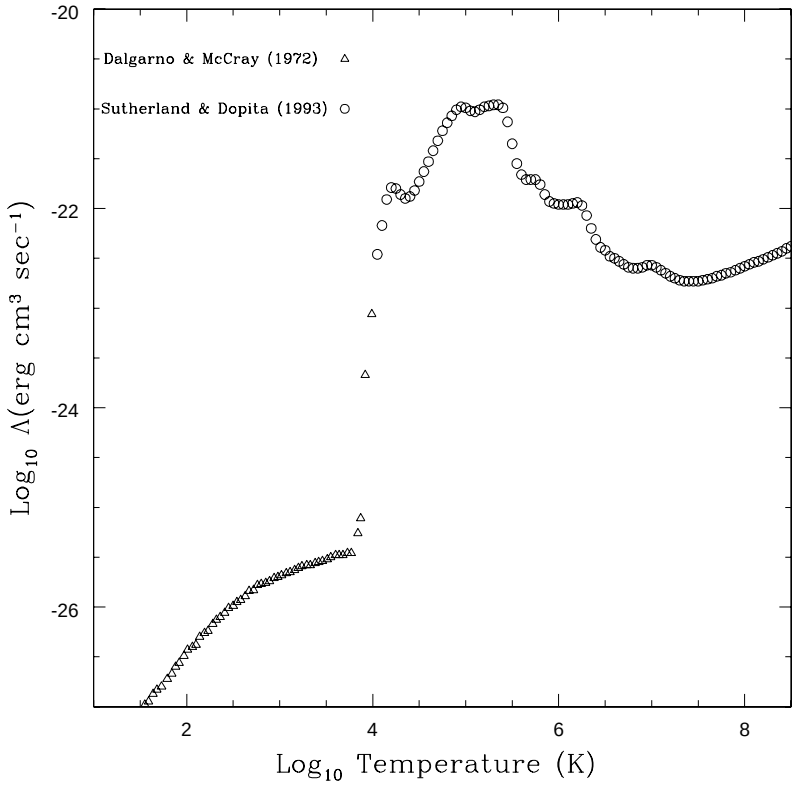

Figure 6.3: Equilibrium cooling curve for a solar metallicity gas.

a fraction of the total energy is transferred to the ISM in the form of thermal energy. This defines the feedback efficiency parameter ϵ. The energy is injected into 3^3 cells around the central explosion cell following a Gaussian profile. The energy each neighboring cell receives is weighted by the square of its distance to the central cell in order to assure a better isotropy of the explosion. The site where a new SN explosion occurs is chosen randomly under the condition that the local density n is such that $n \geq \bar{n}$. This assumption leads to a more realistic fraction of clustered SN explosions. The time interval between two consecutive SN explosions is given by $\Delta t_{SN} = 1/\eta$, where η is the SN explosion rate. However, when the time interval between two consecutive SN explosions become shorter than the CFL (Courant-Friedrisch-Levy) time step, more than one SNe are detonated simultaneously at different locations of the grid. The number of SNe detonated in that case is taken to be the closest integer to the ratio $dt/\Delta t_{SN}$, where dt is the CFL time step. We assume a Galactic SN rate (η_G) of 2.58 $\times 10^{-4}$ yr^{-1} kpc^{-3} assuming a Galactic radius of 15.5 kpc and a scale height for type II SN of 90 pc (Miller and Scalo 1979). We use a frequency of 1/57 yr^{-1} (Cappellaro et al. 1999) which is smaller than earlier estimates of 1/50 yr^{-1} by van den Bergh and McClure (1990) and 1/37 yr^{-1} by Tammann et al. (1994).

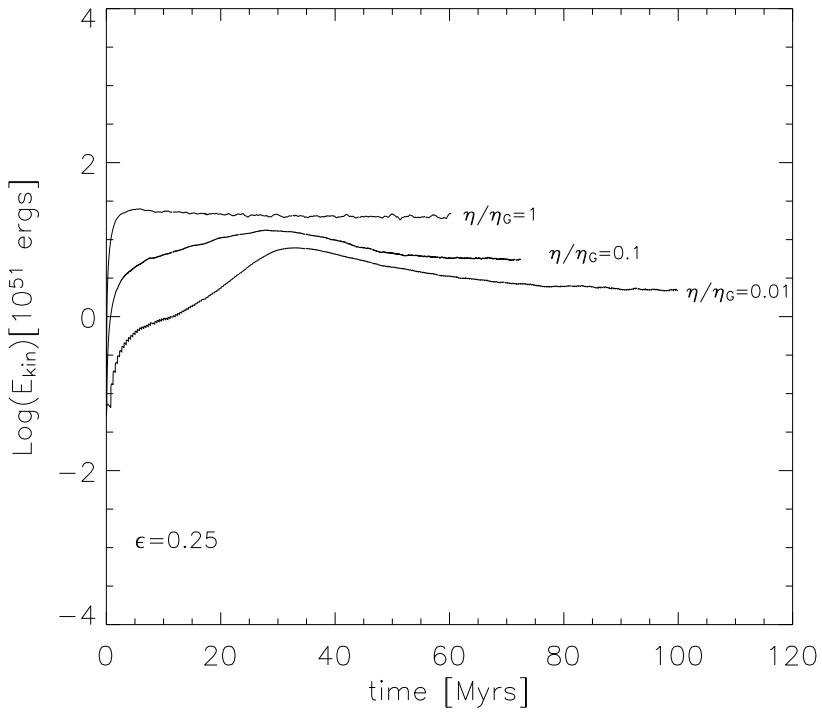

Figure 6.4: Time evolution of the kinetic energy in a number of selected simulations. The supernova rate, normalized to the Galactic value is shown for each curve. The feedback efficiency for all three models is $\epsilon = 0.25$.

6.3 Analysis and derivation of the observables

The simulations are evolved until kinetic energy reaches a stationary value. Fig. 6.4 shows the evolution of kinetic energy in a number of simulations with various set of parameters. The equilibrium value for the kinetic energy is reached when the dissipation equals the amount of injected kinetic energy. The medium acquires kinetic energy from the SNe explosion-induced thermal pressure gradients, and the thermal pressure gradients associated with thermal instability (TI) which occurs in the dense expanding shells. In most simulations, the equilibrium of thermal energy is also reached except for the simulations with a high supernova rate ($\geq 2.5\ \eta_G$). In the latter simulations, the overlap radii between supernova remnants is very small, and all the gas continues to heat up as more and more energy is injected into the system. It is worth mentioning that, due to the high Mach numbers involved in these simulations, they are extremely demanding in terms of CPU time. Runs on 8 processors on the SGI Origin 2000 at the Max-Planck Rechnenzentrum in Garching require, on average, three weeks before convergence is reached.

Fig. 6.5 and Fig. 6.6 show snapshot two-dimensional cuts for models with $(\eta/\eta_G, \epsilon) = (0.1, 0.25)$ and $(1, 0.25)$, respectively. In the simulations with the lower rates, larger and denser clouds are able to form under the effect of thermal instability, before being dispersed by a local SN

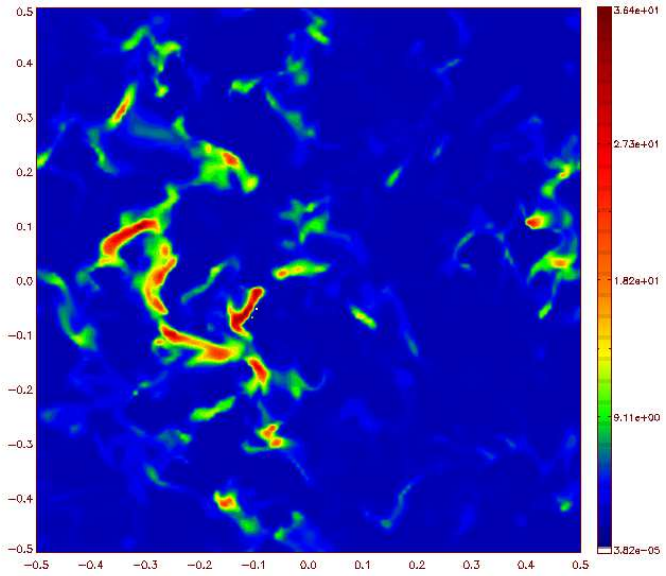

Figure 6.5: Density cut in the data cube at time=72 Myrs for a model with $(\eta/\eta_G, \epsilon) = (0.1, 0.25)$.

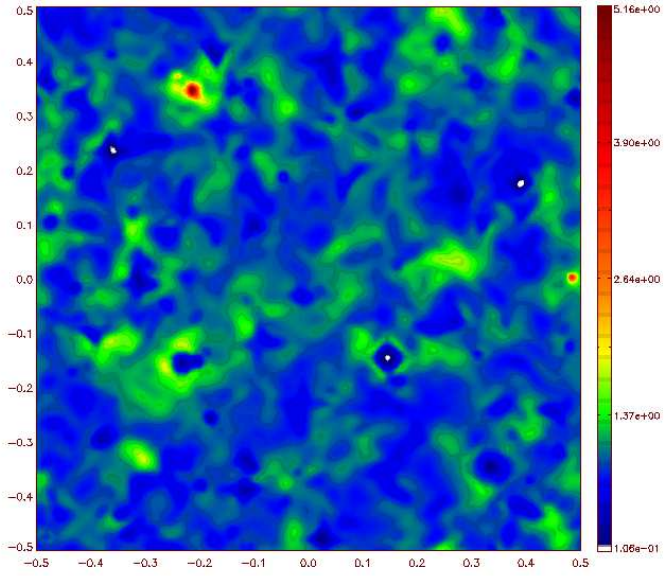

Figure 6.6: Density cut in the data cube at time=60 Myrs for a model with $(\eta/\eta_G, \epsilon) = (1, 0.25)$.

explosion.

We calculate the velocity dispersion of the gas in two complementary ways. In the first method, we calculate the *characteristic* mass weighted velocity v_c from the three-dimensional data as

$$v_c = \sqrt{\frac{\Sigma_{i=1}^{n_{cells}} m_i |v_i|^2}{\Sigma_{i=1}^{n_{cells}} m_i}}, \tag{6.1}$$

where the index i runs over the number of cells in the simulation box. An average is made over the last 5 Myrs (5 values) in each simulations in order to smooth for time fluctuations which is particularly useful for the low SN rate simulations. On the other hand, following a more *observational* approach, the one-dimensional velocity dispersion σ is obtained by fitting the mass-weighted line of sight velocity profile. Intensity is assumed to be proportional to the mass along the line of sight. This is particularly true in the case of the H I line (see Eqs. 5.2-5.5). The velocity profile is then normalized to its maximum value. A second velocity dispersion which we call $\sigma_{\rm H\,I}$ is obtained by fitting a velocity profile where only cells which have temperatures ≤ 12000 K and number densities $n \geq 0.25$ cm^{-3} have been accounted for, thus mimicking the velocity profile of an H I emission line. We have tested the dependence of the fit parameters on the size of the adopted velocity bin. The relevant parameter (i.e., width of the velocity profile) is practically unchanged as we vary the velocity bin size from 0.1 km s^{-1} up to 2.5 km s^{-1}, only the fit-error on the parameters changes. The results we will show correspond to bin sizes of 0.1 and 1 km s^{-1}. The latter value is characteristic of the bin size of single-dish radio telescope (e.g., Effelsberg radio telescope, Green Bank radio telescope) and nears the spectral resolutions obtained with the VLA (Very Large Array) $\simeq 2.5$ km s^{-1} which will be enhanced when the EVLA (Extended Very Large Array) becomes operational. Here also, an averaging over the last 5 Myrs has been performed (5 estimates). Errors on σ and $\sigma_{\rm H\,I}$ are average values of the individual errors derived from the parameters of the fit functions whereas the error on v_c is simply a statistical error over the 5 estimates.

We have attempted to fit the line of sight velocity profiles with several functional distributions, namely, a Gaussian, a Lorentzian, a Moffat profile (modified Gaussian) and a Voigt profile which is the result of the convolution of a Gaussian with a Lorentzian (see Lang 1980 for the mathematical definition of each profile). In all cases, the Gaussian, Lorentzian and Moffat function fits yield the same *dispersion*, but which have a slight different meaning in each case (see Lang 1980 for details). Only a few profiles could be fitted with a Voigt function, however, as unjustified as it is, the fit with a Voigt function, when successful, proved to be an excellent match to the simulated profiles. Fig. 6.7 and Fig. 6.8 show the 1 km s^{-1} binned total gas and H I gas line profiles for the model with $(\eta/\eta_G, \epsilon) = (1, 0.25)$, respectively, whereas Fig. 6.9 and Fig. 6.10 show the same profiles for the model with $(\eta/\eta_G, \epsilon) = (0.1, 0.25)$. Fig. 6.11 and Fig. 6.12 display the total gas velocity profiles corresponding to models with $(\eta/\eta_G, \epsilon) = (1, 0.25)$ and $(0.05, 0.25)$, respectively, with a spectral bin size of 0.1 km s^{-1}. In the latter case, the profile could be perfectly fit with a Voigt profile (blue line). Though Gaussian fitting proves to be quite satisfactory, it is worth mentioning at this stage that our simulated velocity profile have wings that are slightly broader than those associated to Gaussian functions. In a realistic and turbulent ISM, one expects that the turbulent contribution to the line broadening would be described with a Lorentzian and the thermal

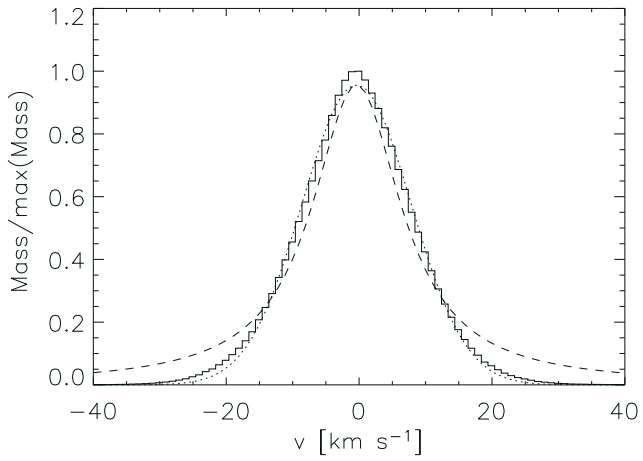

Figure 6.7: Mass weighted velocity profile for the model with $(\eta/\eta_G, \epsilon)$=(1,0.25) and a spectral bin size of 1 km s^{-1}. The profile samples all gas elements in the simulation box. Over-plotted are a Gaussian fit (dotted line) and Lorentzian fit (dashed line).

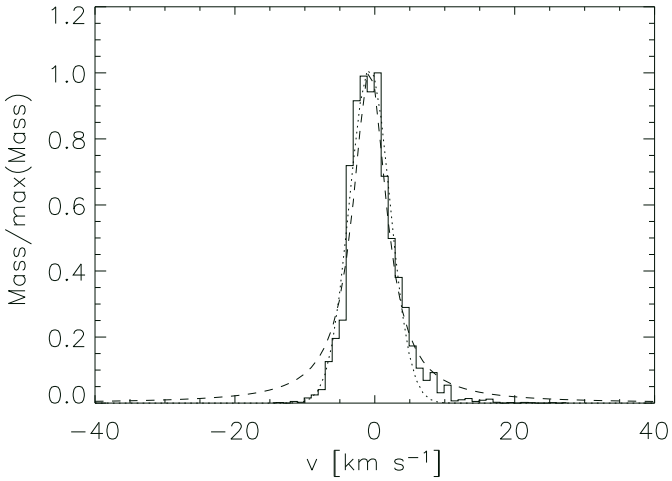

Figure 6.8: Mass weighted velocity profile for the model with $(\eta/\eta_G, \epsilon)$=(1,0.25) and a spectral bin size of 1 km s^{-1}. The profile samples only gas elements with $T \leq 12000$ K and $n \geq 0.25$ cm^{-3}. Over-plotted are a Gaussian fit (dotted line) and Lorentzian fit (dashed line).

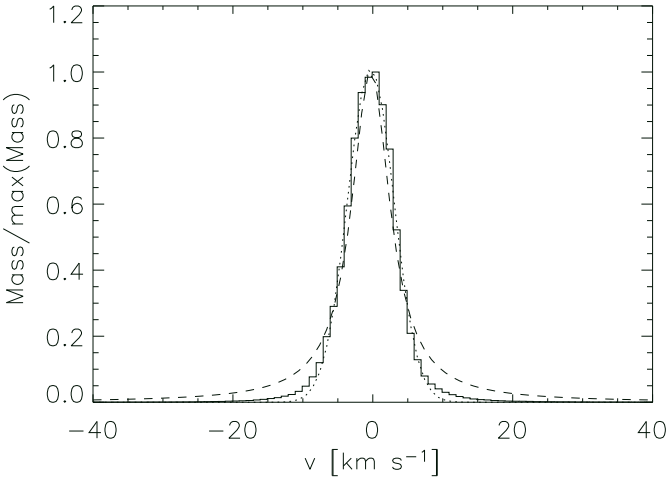

Figure 6.9: Mass weighted velocity profile for the model with $(\eta/\eta_G, \epsilon)$=(0.1,0.25) and a spectral bin size of 1 km s^{-1}. The profile samples all gas elements in the simulation box. Over-plotted are a Gaussian fit (dotted line) and Lorentzian fit (dashed line).

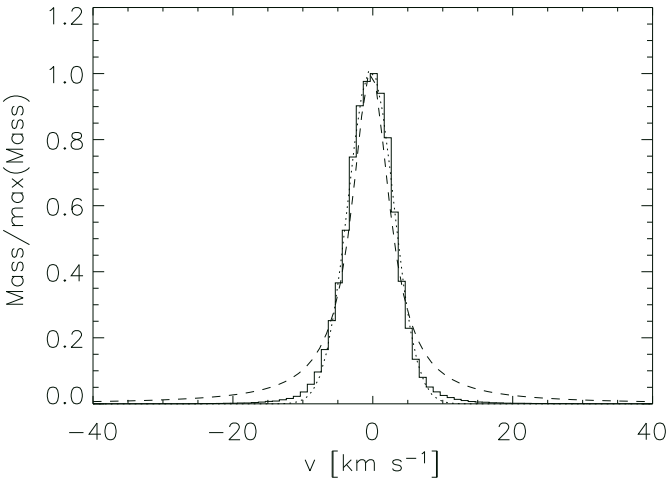

Figure 6.10: Mass weighted velocity profile for the model with $(\eta/\eta_G, \epsilon)$=(0.1,0.25) and a spectral bin size of 1 km s^{-3}. The profile samples only gas elements with $T \leq 12000$ K and $n \geq 0.25$ cm^{-3}. Over-plotted are a Gaussian fit (dotted line) and Lorentzian fit (dashed line).

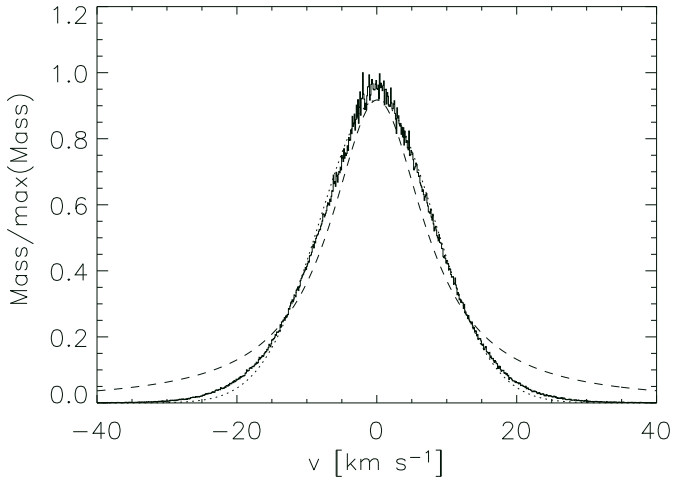

Figure 6.11: Mass weighted velocity profile for the model with $(\eta/\eta_G, \epsilon)$=(1,0.25) and a spectral bin size of 0.1 km s^{-1}. The profile samples all gas elements in the simulation box. Over-plotted are a Gaussian fit (dotted line) and Lorentzian fit (dashed line).

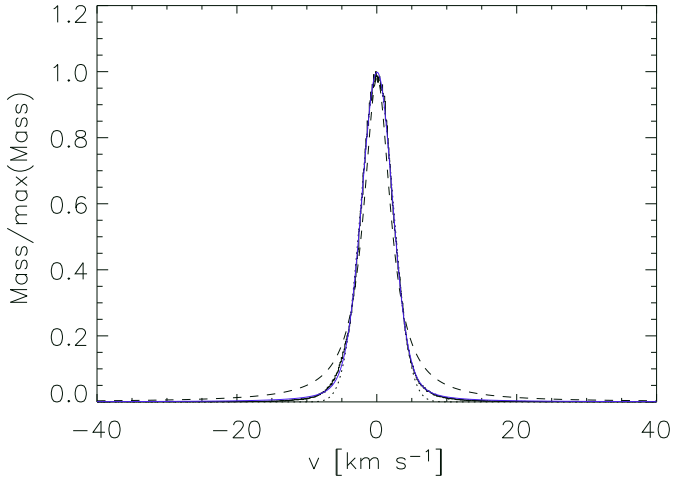

Figure 6.12: Mass weighted velocity profile for the model with $(\eta/\eta_G, \epsilon)$=(0.05,0.25) and a spectral bin size of 0.1 km s^{-1}. The profile samples all gas elements in the simulation box. Over-plotted are a Gaussian fit (dotted line) and Lorentzian fit (dashed line). The full blue line corresponds to a fit with a Voigt profile.

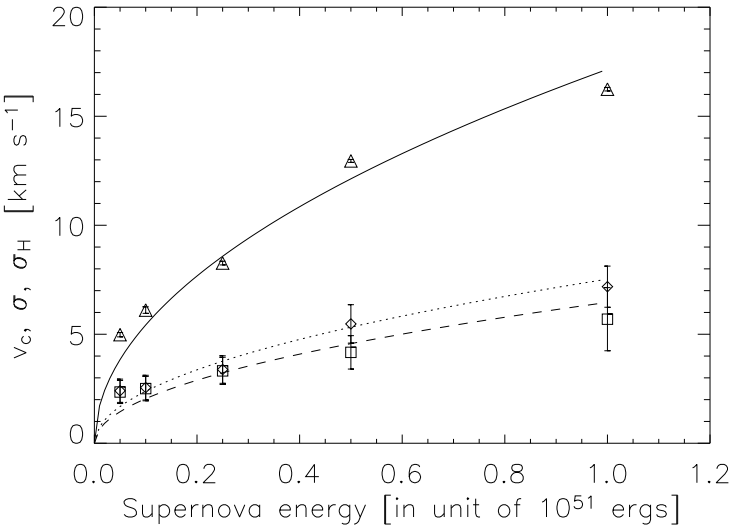

Figure 6.13: Characteristic velocity v_c (Eq. 6.1) (triangles), mass-weighted line of sight velocity σ (diamonds) and H I gas mass-weighted line of sight velocity $\sigma_{\rm H\,I}$ (squares) (both have spectral bin size of 0.1 km s^{-1}) as a function of the supernova feedback energy equal to $\epsilon \times 10^{51}$ ergs.

broadening of the line by a Gaussian. The convolution of the Gaussian and Lorentzian function results in a Voigt profile. However, even when we introduce a thermal broadening component to the line profile (in § 6.5.1), the Voigt profile fails to systematically fit the different line profiles of the different models.

6.4 The effect of the feedback efficiency

Since energy injection in our simulations is discrete, a similar value $\eta \times \epsilon$ with different permutations of η and ϵ does not yield similar results because of the differences in the interactions of the expanding shells and non-linear development of TI. Ideally, a full investigation of the two-dimensional parameter space would be necessary, however, this would lead us beyond our current computational capabilities. At this stage, we have taken an intermediate approach and have explored the effects of η and ϵ independently by fixing one parameter and varying the other.

We performed a first set of simulations where we have varied the supernova feedback efficiency between 0.05 and 1 for a constant value of the supernova rate $\eta = 0.1\ \eta_G$. Fig. 6.13 shows the dependence of the characteristic velocity v_c, line of sight velocity dispersion σ and H I line of sight velocity dispersion $\sigma_{\rm H\,I}$ (latter two values obtained with a spectral bin size of 0.1 km s^{-1}) on ϵ. Assuming that all of the three values would be zero if the feedback efficiency is zero, this would mean that v_c, σ and $\sigma_{\rm H\,I}$ would rapidly increase, followed thereafter by a slower increase at larger values of ϵ. As a velocity has the dimensions of the square root of an energy, we have attempted to fit v_c, σ and $\sigma_{\rm H\,I}$ by functions of the form $A\sqrt{\epsilon}$. Fits with these

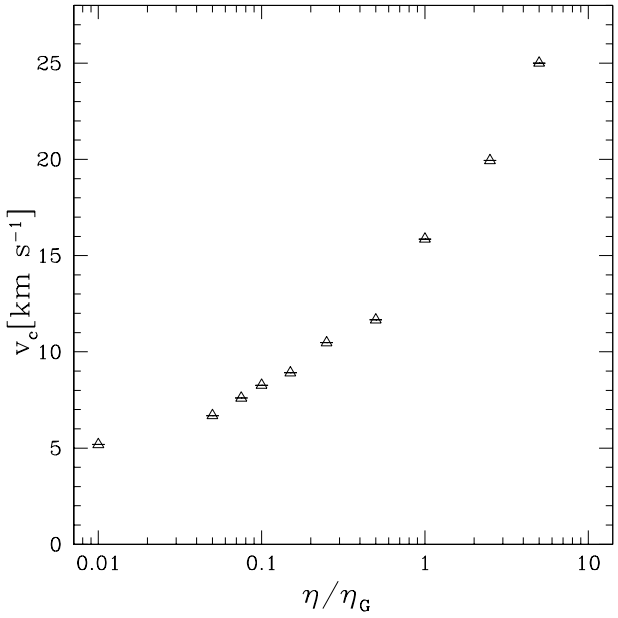

Figure 6.14: Characteristic velocity v_c as a function of supernova rate η (normalized to the Galactic value η_G).

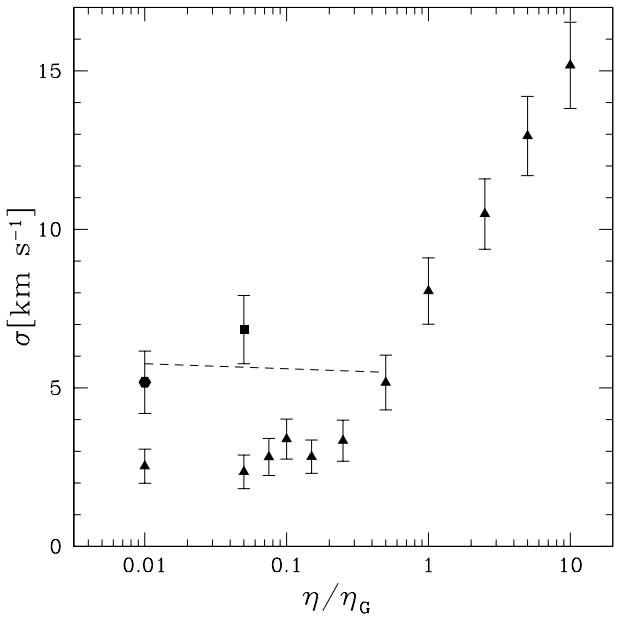

Figure 6.15: Velocity dispersion of the gas σ as a function of the supernova rate η (normalized to the Galactic value η_G, filled triangles). Filled square and filled hexagon correspond to simulations where the average density has been reduced by factors of 5 and 10, respectively. The displayed data has been obtained using a spectral bin size of 0.1 km s^{-1}.

functional forms are over-plotted to the data in Fig. 6.13. The values of the fit parameter A are 17.15 ± 0.59, 7.53 ± 0.46 and 6.64 ± 0.64 for v_c, σ and $\sigma_{\rm H\,I}$, respectively. In all three curves the data is noticeably slightly higher than the estimate of the fit functions for small values of ϵ. This is plausibly an indication that a second mechanism is responsible for generating kinetic energy in the medium on top of the direct supernova driving. We will particularly focus on that point in the next section in which we investigate the dependence of the velocity dispersion on the SN rate.

The feedback efficiency of a type II SN in a medium of average density 1 cm^{-3} and solar metallicity was estimated by Thornton et al. (1998) to be around 0.20, roughly equally distributed in thermal and kinetic energy. However, this estimate was based on a one-dimensional model in which the gas has little degrees of freedom, and thus, should be regarded with caution. For the investigation of the supernova rate effect on the velocity dispersion, we shall adopt a value of $\epsilon = 0.25$.

6.5 The supernova rate-velocity dispersion relation

The most relevant parameter in our simulations is the supernova rate η. Fixing ϵ at a value of 0.25, we performed a set of simulations with different values of η ranging from 0.01 to 10 times the Galactic value. Fig. 6.14 and Fig. 6.15 show the dependence of v_c and σ on η. For $\eta/\eta_G \gtrsim 0.5$, Fig. 6.14 and Fig. 6.15 show that v_c and σ increase rapidly with an increasing supernova rate, thus mimicking a *starburst regime* similar to the one observed in Fig. 6.2. For $\eta/\eta_G \lesssim 0.5$, the velocity dispersion shows a slow decrease with a decreasing η. This transition at $\eta/\eta_G \simeq 0.5$ is probably an indication that the velocity dispersion of the medium in the low rate regime is not fixed by SN driving alone. SNe explosions will cause a certain fraction of the gas to be maintained in the thermally unstable regime (150 K $\lesssim T \lesssim$ 7500 K) when cold gas is restored to the warm phase. Thermal instability occurs in the cooling expanding shells, but also everywhere in the inter-supernova remnants medium where the criterion for thermal instability (Eq. 3.14) is satisfied, thus adding an extra component to the kinetic energy injected into the medium.

We interpret the flatness of the $\sigma - \eta$ relation for $\eta/\eta_G \lesssim 0.5$ as resulting from the interplay between direct supernova driving and thermal instability. Fig. 6.16 and Fig. 6.17 show, after convergence is reached, the dependence of the volume filling factor and mass fraction of the thermally-unstable gas (150 K $\lesssim T \lesssim$ 7500 K) on the normalized SN rate, respectively whereas Fig. 6.18 displays, as an example, the evolution of the volume filling factor and mass fraction of the unstable, cold ($T <$ 150 K) and warm phase ($T >$ 7500 K) in the model with $(\eta/\eta_G, \epsilon = (0.1, 0.25)$. In Fig. 6.16, the mass fraction of the unstable gas shows a peak at $\eta/\eta_G \simeq 0.5$ which roughly corresponds to the position of the transition observed in the $\eta - \sigma$ relation, and a non-zero value at smaller values of η. More relevant is the dependence of the volume filling fraction of the unstable gas F_v which is a more reliable description of the *spatial distribution* of the effects of thermal instability. At the high rate values, the gas is predominantly hot and becoming increasingly hotter over time. Therefore the volume filling factor of the unstable gas in that regime is close to zero. At the low rate values, the volume filling factor of the unstable gas starts decreasing again, simply because less and less cold gas is heated and restored into the warmer phase by SN explosions. Clearly, if very small

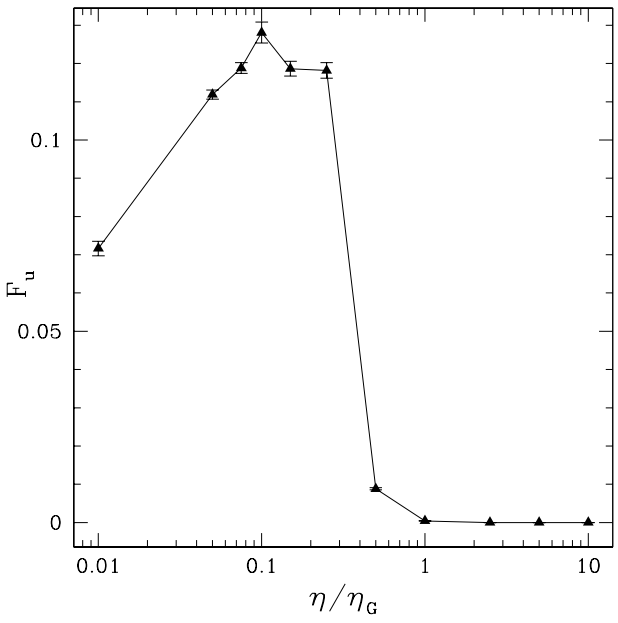

Figure 6.16: Volume filling factor of the unstable gas (150 K $\lesssim$ T $\lesssim$ 7500 K) as a function of the supernova rate η (normalized to the Galactic value η_G). The error bars represent the statistical errors for 5 estimates of each value (last 5 Myrs in each simulation).

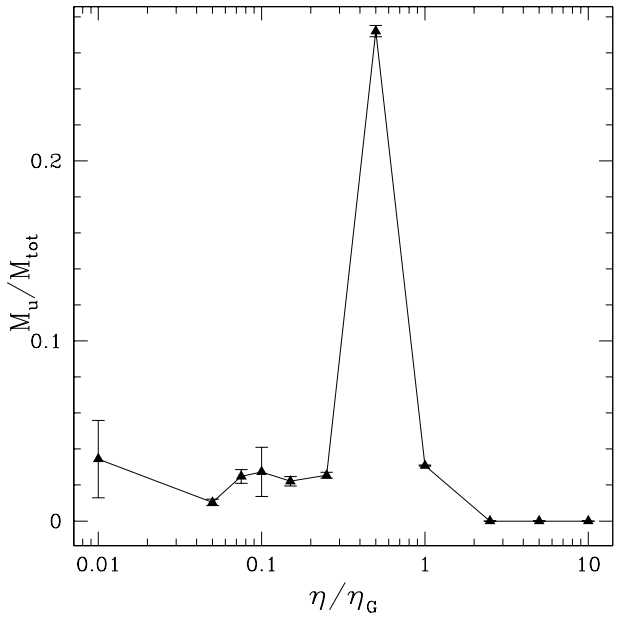

Figure 6.17: Mass fraction of the unstable gas (150 K $\lesssim$ T $\lesssim$ 7500 K) as a function of the supernova rate η (normalized to the Galactic value η_G). The error bars represent the statistical error for 5 estimates of each value (last 5 Myrs in each simulation).

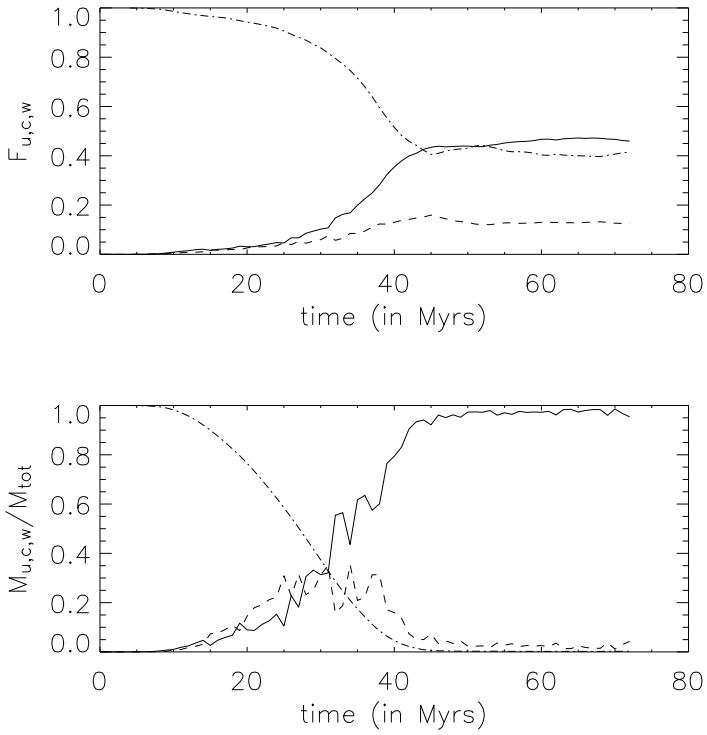

Figure 6.18: Time evolution of the volume filling factor (top) and mass fraction of the unstable gas (150 K $\lesssim T \lesssim$ 7500 K, dashed line), cold gas ($T <$ 150 K, solid line) and warm gas ($T >$ 7500 K, dot-dashed line).

rates are used, both the direct supernova driving and thermal instability would not be able to sustain turbulence in the medium. Turbulence will then decay before the next supernova explosion occurs.

As the simulations described in this chapter are not scale free, because of the presence of a realistic cooling function, another relevant point to investigate is the role of the average density. Empirical star formation laws state that the star formation rate decreases with decreasing gas surface density. In the previous simulations, we have used an average density of 0.5 cm^{-3}. It is particularly interesting to test the effect of varying the density for small values of the supernova rate. Over-plotted on Fig. 6.15 are the results of two simulations with $\eta/\eta_G = 0.05$ and $\eta/\eta_G = 0.01$ where the average density have been decreased, by a factor of 5 and 10, respectively. These are shown with the full square and full hexagon, respectively. Dropping the scaling coefficient, if one assumes the supernova rate (i.e., star formation rate)-gas density to follow a Kennicutt type law $\eta/\eta_G = \bar{n}^{1.4\pm0.15}$ (Kennicutt 1998), for an average density value $\bar{n} = 0.5$ cm^{-3} $\eta/\eta_G = 0.38\pm^{0.042}_{0.037}$. To values of $\eta/\eta_G = 0.05$ and 0.01 will correspond, using the same law, average densities of $\bar{n} = 0.117\pm^{0.027}_{0.026}$ cm^{-3} and $\bar{n} = 0.037\pm^{0.0139}_{0.0123}$ cm^{-3}, which roughly equal the densities of 0.1 cm^{-1} and 0.05 cm^{-1} we have adopted for those rates. Thus, we can consider the three points $(\eta/\eta_G, \bar{n}[cm^{-3}]) = (0.5, 0.5)$,

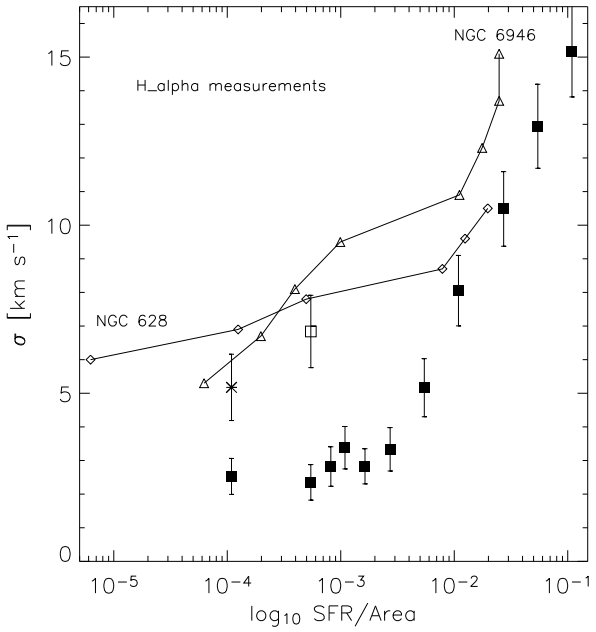

Figure 6.19: Velocity dispersion of the gas σ as a function of the star formation rate per unit area ($M_\odot$ yr^{-1} kpc^{-2}) (filled squares). open square and star correspond to simulations where the density has been reduced by a factor of 5 and 10, respectively. The displayed data has been obtained using a spectral bin size of 0.1 km s^{-1}. For NGC 628 (open diamonds) and NGC 6946 (open triangles), the velocity dispersion is derived from H I 21 cm line observations and the star formation rates from Hα observations.

(0.05,0.1) and (0.01,0.05) as being a rough representation of a Kennicutt law in the $\eta - \sigma$ space and fit their corresponding $\eta/\eta_G - \sigma$ data. Due to the large scatter and the limited number of points, the fit parameters can only be obtained with associated large uncertainties. The fit to the data, which has the form $\sigma = -0.159 \log_{10}(\eta/\eta_G) + 5.44$ is over-plotted to the three data points in Fig. 6.15. Tentatively, the conclusion we can draw here is that the flatness of the $\sigma - \eta$ relation around $\sim 5 - 6$ km s^{-1} can be maintained at low values of the supernova rate if the average density is reduced for lower rates, as predicted by the empirical star formation laws such as the Kennicutt law. However, more simulations are needed to confirm this result and to probe the results for other star formation laws. Unfortunately, this is beyond the scope of this work, essentially for reasons of CPU time.

6.5.1 Comparison to the observations

In Fig. 6.19, the same data appearing in Fig. 6.15 is shown after transforming the SN rate per unit volume into a star formation rate per unit area (units of $M_\odot$ yr^{-1} kpc^{-2}). We use the transformation of the SN rate into a star formation rate (SFR), η/SFR=0.0067, derived using the PEGASE stellar population synthesis model (Fioc and Rocca-Volmerange 1997) and assuming a Salpeter Initial Mass Function (IMF) (Salpeter 1955). We perform a comparison to two galaxies, NGC 628 and NGC 6946 for which the star formation rates have been

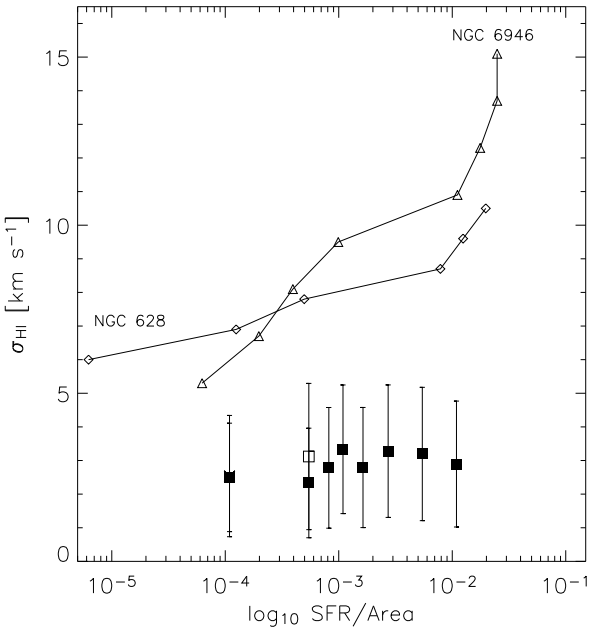

Figure 6.20: Velocity dispersion of the H I gas $\sigma_{\rm H\,I}$ as a function of the star formation rate per unit area ($M_\odot$ yr^{-1} kpc^{-2}) (filled squares). open square and star correspond to simulations where the density has been reduced by a factor of 5 and 10, respectively. The displayed data has been obtained using a spectral bin size of 1 km s^{-1}. For NGC 628 (open diamonds) and NGC 6946 (open triangles), the velocity dispersion is derived from H I 21 cm line observations and the star formation rates from Hα observations.

estimated, at different radii, from Hα observations (Martin and Kennicutt 2001), along with velocity dispersion estimates which are derived from H I 21 cm line observations (Shostak and van der Kruit 1984 and Kamphuis and Sancisi 1993). Fig. 6.20 shows a comparison of the velocity dispersion measured from the H I gas (100 K $\lesssim T \lesssim$ 12000 K) velocity profile $\sigma_{\rm H\,I}$ to the same observations. A number of remarks can be drawn from the comparison presented in Fig. 6.19 and Fig. 6.20 : (a) The position of the transition to the starburst regime (i.e., location of sharp increase in the velocity dispersion) at around SFR/Area $\simeq 5 \times 10^{-2} - 10^{-2}$ $M_\odot$ yr^{-1} kpc^{-2} observed in the simulations, is relatively in good agreement with the observations in NGC 628 and NGC 6949. It is also in very good agreement with the transition to the starburst regime observed in Fig. 6.2, (b) there is good agreement between our models and the observations at the high SN rate values within $2-3$ km s^{-1}. This difference can be easily explained by the effect of beam smearing which tends to increase the observed velocity dispersions, particularly in the inner parts of galaxies and (c) at the intermediate and low SN rate values, σ and $\sigma_{\rm H\,I}$ fall below the observed values by a factor of 2-3 even when the density correction is taken into account in the case of $\sigma_{\rm H\,I}$ (open square and star in Fig. 6.20). The value of σ and $\sigma_{\rm H\,I}$ become very similar at the low rate values as most of the gas in these simulations has a temperature below 12000 K. On the other hand no H I is found in the simulations with $\eta/\eta_G \geq 1$.

However, the velocity dispersions observed in NGC 628 and NGC 6946 (same for the observations presented in Fig. 6.2), in addition of being affected to some degree by beam smearing due to the limited resolution of radio telescopes (this is a minor effect at the outer galactic radii), are a *global* velocity dispersion which do not disentangle the true dynamical value (which is the only one we have in our simulations) from the thermal broadening of the line, simply because the temperature structure of the gas in the observations in not known. Thermal broadening, $v_T = \sqrt{2\ k_b\ T/m}$, is the dispersion of the velocity probability distribution function for an ensemble of particles of a non relativistic and non degenerate gas which is in thermal equilibrium at a kinetic temperature T, where m is the mass of the particles and in our case, m is the equal to the proton mass. The value of the thermal broadening that would affect the H I 21 cm emission line is shown as function of temperature in Fig .6.21. We have corrected for the effect of thermal broadening in two ways :

(a) **the simplistic method** : We can subtract from the observational velocity dispersion values a velocity component associated with thermal broadening at a given equilibrium temperature for the H I. This is obviously a simplification as we have assumed the H I gas to have the same temperature at all radii. Fig. 6.22 shows the corrected velocity dispersion, using this method, for three values of the equilibrium temperature of the H I gas, namely 100 K, 500 K, and 750 K. The correction improves the agreement between the observations and the simulations, particularly at the outer galactic radii and if the H I is assumed to be warmer than 100 K (look at middle and bottom plots in Fig. 6.22 where the H I gas in NGC 628 and NGC 6946 is assumed to be at 500 K and 750 K, respectively). The fact that the gas in the outer parts could have temperatures higher than 100 K is plausible since the density in the outer parts is low and the gas could be more easily heated by extragalactic cosmic rays and X-ray photons. This is unlikely however to be the case for the inner parts of the galaxy where the H I gas is more likely to have, like in the Milky Way, a non-negligible fraction of the H I in the cold phase at around 100 K. Nevertheless, recent observations by Heiles (2001) suggest that about half of the mass of the diffuse interstellar gas in the Galaxy may have temperatures which are larger than 100 K (a few hundreds to a few thousands Kelvin). Only an accurate determination of the temperature structure in galaxies such as NGC 628 and NGC 6946 may lay out strong constraints on the contribution of thermal broadening as a function of radius to the total velocity dispersion (details might be more complicated due, for example, to the presence of spiral structures).

(b) **the less simplistic method** : Here, we have assumed that the particles in each cell have a Gaussian velocity profile which is centered around the local dynamical velocity and which have a dispersion in the velocity space equal to v_T, where v_T is the local thermal broadening calculated using the local temperature. The amplitude of the profile is given by the local density. Only cells with $T \leq 12000$ K and $\bar{n} \geq 0.25$ cm^{-3} are taken into account. The individual velocity profiles are summed up in the velocity space and binned with a spectral bin size of 1 km s^{-1} (also with a spectral bin size of 0.1 km s^{-1} for the purpose of comparison). Fig. 6.23 and Fig. 6.24 display two mass weighted, thermally broadened velocity profiles corresponding to simulations $(\eta/\eta_G, \epsilon)$=(1,0.25) and (0.1,0.25), respectively. They can be compared to Fig. 6.8 and Fig. 6.10 (though the data there is binned with a spectral bin size of 1 km s^{-1}), respectively, in order to appreciate the effects of thermal broadening on the line profile. Fig. 6.25 shows a comparison of the H I velocity dispersion $\sigma_{\rm H\,I}$ to the observational data using this more reliable approach for correcting for the effect of thermal broadening.

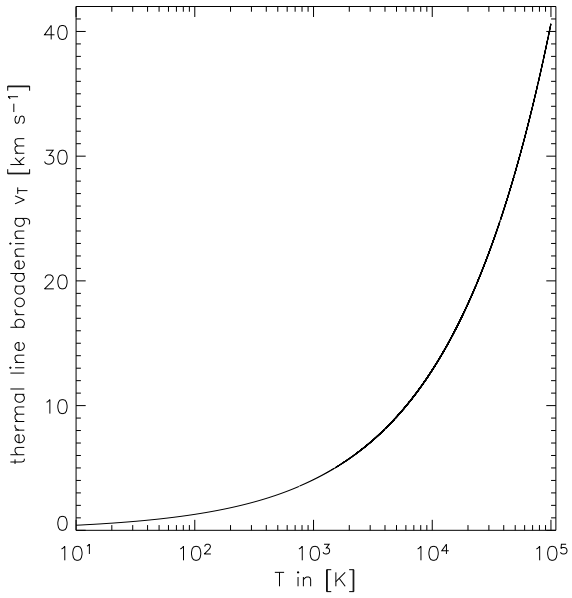

Figure 6.21: Thermal line broadening v_T as a function of temperature for a hydrogen gas.

The result is somewhat encouraging. For SFR/Area in the range of $5 \times 10^{-3} - 10^{-2}$ M $_\odot$ yr^{-1} kpc^{-2} (i.e., $\eta/\eta_G \simeq 0.5 - 1$), the agreement to the observations concerning both NGC 628 and NGC 6946 is quite acceptable. At the lower SN rates values, the agreement is less satisfying even when the Kennicutt rate-adapted average densities are used (open square and star in Fig. 6.25). However, a comparison only to the data of NGC 628 and NGC 6946 might be slightly misleading. In the case of galaxies such as NGC 1058 (Dickey et al. 1990) and NGC 3938 (van der Kruit and Shostak 1982), for which we unfortunately do not have radially dependant estimates of the star formation rate, the velocity dispersion levels off in the outer radii at a value of the order of 5-6 km s^{-1} which is in better agreement to the values coming out from our simulations. There is another effect, which we haven't included in our current simulations and which provides a source of secondary heating in the medium other than the direct heating by supernova explosions, namely a background heating on the scale of the entire system provided by the photoelectric effect, cosmic rays and soft X-rays (see next sections for more discussion). These background heating processes might be of quite little importance in the case of media with SFR/Area $\gtrsim 5 \times 10^{-3}$ M$_\odot$ yr^{-1} kpc^{-2} (i.e. $\eta/\eta_G \gtrsim 0.5$), but they might play a significant role in maintaining a warmer phase of the gas at the lower SN rate values. Thus the velocity line profiles might be broader than what we have calculated in the absence of such background heating processes.

6.6 The need for improved models

Effect of the vertical structure : The vertical stratification, which we have neglected in this present work for reasons of simplifying the problem might be one of the physical effects that we need to include first in subsequent models. We intend to perform models with a

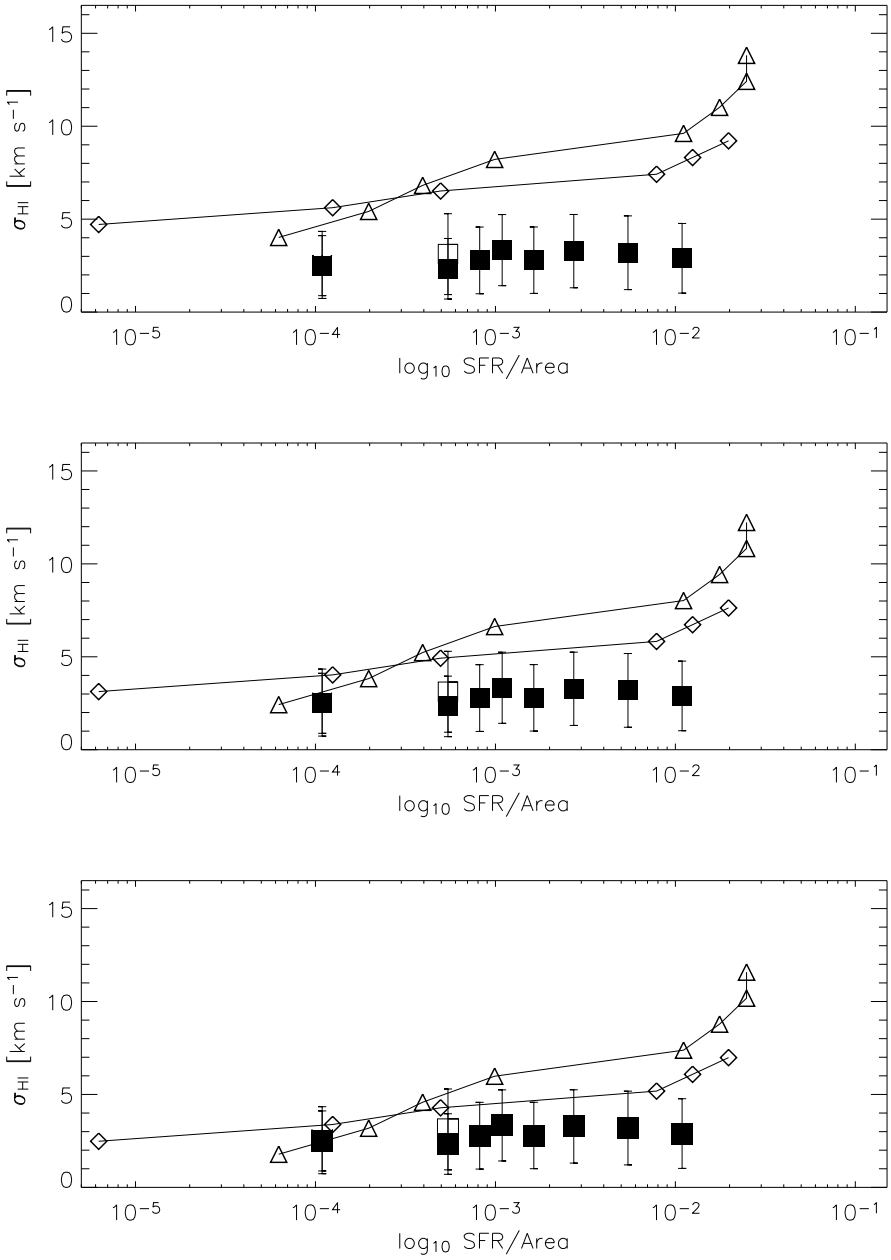

Figure 6.22: Same as in Fig. 6.20 but where thermal broadening has been subtracted from the observed velocity dispersion assuming that the H I gas is at 100 K (top), 500 K (middle) and 750 K (bottom). Spectral bin size used is 1 km s^{-1}.

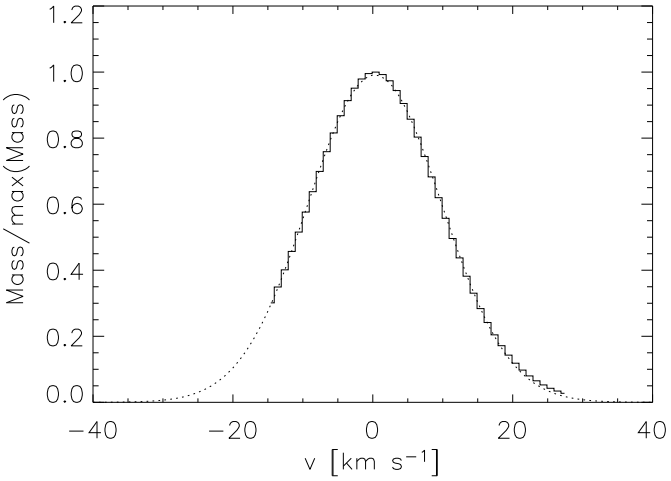

Figure 6.23: Mass weighted velocity profile for the model with $(\eta/\eta_G, \epsilon)$=(1,0.25) and corrected for thermal broadening. The spectral bin size of 1 km s^{-1}. The profile samples only gas elements with $T \leq 12000$ K and $n \geq 0.25$ cm^{-3}. Over-plotted is a Gaussian fit (dotted line).

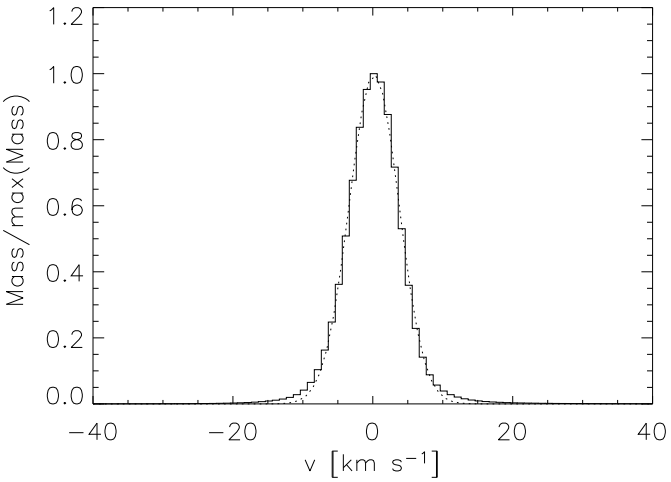

Figure 6.24: Mass weighted velocity profile for the model with $(\eta/\eta_G, \epsilon)$=(0.1,0.25) and corrected for thermal broadening. The spectral bin size of 1 km s^{-1}. The profile samples only gas elements with $T \leq 12000$ K and $n \geq 0.25$ cm^{-3}. Over-plotted is a Gaussian fit (dotted line).

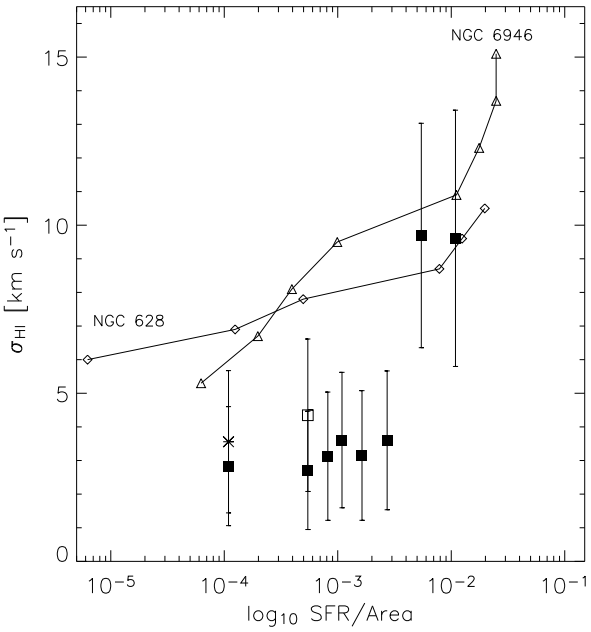

Figure 6.25: Velocity dispersion of the H I gas $\sigma_{\rm H\,I}$ as a function of the star formation rate per unit area ($M_\odot$ yr^{-1} kpc^{-2}) (filled squares). The values have been corrected for the effect of thermal broadening. Open square and star correspond to simulations where the density has been reduced by a factor of 5 and 10, respectively. The displayed data has been obtained using a spectral bin size of 1 km s^{-1}.

much larger length of the box in the vertical direction, using outflow boundary conditions to allow the gas to escape from the upper and lower boundaries of the simulation box. The escaping hot gas would not affect the H I 21 cm line profile. However, denser blobs of gas which are expelled at higher latitudes by the SN explosions will cool and fall back into the disk in the form of high velocity clouds. In principle, these high velocity clouds should normally be observed as broad wings in the velocity profile and are usually fitted with a second Gaussian. Infalling decelerated gas, close to the galactic disk will be most probably mixed with the local gas in the disk, thereby contributing, eventually, to the broadening of the velocity profile.

Effect of the chemistry : In the simulations presented in this chapter, the cooling curve we have used is a solar metallicity curve that assumes chemical equilibrium. This cooling curve describes principally the radiative cooling by neutral atoms whereas molecular cooling by molecules such as the H_2 molecule has not been included. At the high and intermediate rate values, this might not be of much relevance as the over-densities that are produced are a factor 3-5 the average density (a few cm^{-3}) (see Fig. 6.5) and no dense molecular material is expected to form is these simulations, in contrast to the cases with the low rates values, where clouds have time to form and condense further before being destroyed by the next generation of SNe (see Fig. 6.6). Molecular hydrogen, starts to form when densities of the order of 10^3 cm^{-3} are reached and which are shielded against UV radiation. Such densities are not

reached in our simulations, however, this might be only a resolution effect. The introduction of a chemical network in a hydrodynamical AMR code would help tackle the problem of the molecules formation in the expanding shells more accurately, and help better describe the additional molecular cooling effect and the associated fragmentation process and it's effects on the local velocity field.

Effect of the metallicity : The occurrence and efficiency of the thermal instability is intimately related to the shape of the cooling curve which characterizes the medium. Cooling curves are a reflexion of the strength of the emission lines of atoms present in the medium. At lower metallicity, the emission lines from metals are weaker and the cooling less efficient. The dependence of the cooling rate on the metallicity has been calculated by Boehringer and Hensler (1989), unfortunately only in the temperature range $10^4 - 10^8$ K. Their results show that the cooling rates may differ, in some temperature ranges, by several orders of magnitude for metallicities between $10^{-2} \leq Z/Z_\odot \leq 2$ ($Z/Z_\odot = 2$ is the upper metallicity limit in their calculations) and becomes independent of the metallicity for $Z/Z_\odot < 10^{-2}$. In future work, we plan to investigate the role of metallicity on the dynamics of the ISM by including it as a parameter in our simulations.

effect of a background heating : The intensity of this background heating is difficult to estimate for systems with a different SN rate. As no established formulations of this problem exist in the literature, we intend to model the background heating from photoelectric effect, cosmic rays and soft X-rays as being fractions of the total supernova heating associated with a given SN rate. We have introduced routines for the photoelectric heating, cosmic rays heating and soft X-ray heating into the ZEUS code and simulations taking into account these effects will be presented elsewhere.

6.7 Summary and discussion

In this chapter, we have investigated the dependence of the velocity dispersion in the interstellar medium (ISM) on the supernova (SN) rate and SN feedback efficiency and in some cases on the ISM average number density. We used local, three-dimensional numerical simulations in which the SN type II explosions are detonated in random positions of the grid, separated by time intervals which are inversely proportional to the SN rate. Radiative cooling of the gas is also taken into account with a minimum cutoff temperature of 100 K. For each simulation, we calculate the three-dimensional characteristic velocity dispersion v_c (Eq. 6.1) and the one-dimensional velocity dispersion, σ, obtained by fitting the line of sight velocity profile by specific mathematical functions, and in particular with a Gaussian profile. We also calculate $\sigma_{\rm H\,I}$, which is the one-dimensional velocity dispersion obtained from fitting the line of sight velocity profile of the gas with a temperature $T \leq 12000$ K and a number density $n \geq 0.25$ cm^{-3} (i.e., the H I gas). Ideally, a full investigation of the two-dimensional parameter space would be necessary, however, this would lead us beyond our current computational capabilities. At this stage, we have taken an intermediate approach and explored the effects of η and ϵ independently by fixing one parameter and varying the other.

On the observational side, in many disk galaxies, the velocity dispersion of the gas is seen to vary radially from 12-15 km s^{-1} in the inner parts and drop to nearly constant values around

5-8 km s^{-3} at the outer radii. Fig. 6.1 shows the radial profile of the velocity dispersion in NGC 1058 while Fig. 6.19 displays the velocity dispersion of NGC 628 and NGC 6946 where the star formation rate is known as a function of the radius. Additionally, if the characteristic velocity dispersion (despite it is an ill defined value due to the large beam smearing effects), is plotted versus the star formation rate in a large sample of galaxies, it clearly shows a similar behavior to the galaxies where star formation is radially resolved. The velocity dispersion is seen to be independent of the star formation rate per unit area for values lower than $5 \times 10^{-3} - 10^{-2}$ $M_\odot$ yr^{-1} kpc^{-2}, before increasing sharply at larger values of the star formation rate (see Fig. 6.2). For the purpose of comparing our results to NGC 628 and NGC 6946, we have transformed the supernova rate into a star formation rate by using the stellar population synthesis model PEGASE (Fioc and Rocca-Volmerange 1997). Other mechanisms have been suggested in the literature in order to explain the flatness of the velocity dispersion profile in the outer parts of galaxies. The role of the magneto-rotational instability (MRI) has been discussed by Sellwood and Balbus (1999) in the case of NGC 1058. However, recent numerical simulations in isothermal disks show that MRI-induced turbulence is restricted to the very inner parts of the galactic disk where the shear is stronger and drops rapidly at larger radii (Dziourkevitch et al. 2004). Recent simulations show that the MRI might be completely overwhelmed by the effect of stellar feedback (M. Korpi, private communication).

Our results show that v_c, σ and $\sigma_{\rm H\,I}$ depend on the supernova feedback efficiency ϵ as $A\sqrt{\epsilon}$, where A is a scaling coefficient, different for each quantity. This is expected as the velocity has the dimensions of the square root of an energy. The dependence of v_c, σ and $\sigma_{\rm H\,I}$ on the SN rate η is more complex. For values of $\eta/\eta_G \gtrsim 0.5$ (i.e., SFR/Area $\geq 10^{-2}$ $M_\odot$ yr^{-1} kpc^{-2}), where η_G is the Galactic SN rate, σ increases sharply with η and is in good agreement with the observations (for $\eta/\eta_G \geq 1$ no H I gas is found in the simulations). For $\eta/\eta_G \lesssim 0.5$, σ and $\sigma_{\rm H\,I}$ are observed to be independent of η and possess a value of ~ 3 km s^{-1}. This plateau at ~ 3 km s^{-1} is a factor $2-3$ lower that the velocity dispersion plateau observed in galaxies such as NGC 1058 (Dickey et al. 1990), NGC 628 (Shostak and van der Kruit 1984) and NGC 6964 (Kamphuis and Sancisi 1993). Interestingly, the position of the transition to the starburst regime (i.e., transition to the SN or SFR range where the velocity dispersion increases rapidly with the SN rate) is found to be the same as the one observed in the observations (see Fig. 6.2 and Fig. 6.19). To remedy for the low level of agreement between the models and the observations at the lower SN rate values, we have corrected the velocity profiles by accounting for the effect of thermal broadening. We have attempted to correct for the thermal broadening effect in two ways : In the first approach, we have subtracted a thermal broadening contribution from the velocity dispersion in the observations (NGC 628 and NGC 6946). Since the radial temperature structure of the gas in these galaxies in not known, we have calculated the thermal broadening assuming the gas is at 100 K, 500 K, and 750 K. An acceptable agreement is reached between the models and the observations if the H I gas in the galaxies is assumed to be at temperatures larger than 100 K, which is a plausible assumption in their outer parts, where the density is low and where the gas can be heated by extragalactic cosmic rays. In a second, more consistent approach, we have assumed that the particles in each cell have a Gaussian distribution centered around the local dynamical velocity, of an amplitude equal to the local density, and of a width given by the local thermal velocity calculated from the local temperature. By summing up the velocity profiles, we obtain naturally a global velocity profile in which the effect of thermal broadening is accounted for. The results of this second approach are somewhat encouraging.

An excellent agreement is found between the models and the observations for values of the SFR/Area in the range $5 \times 10^{-3} - 10^{-2}$ $M_\odot$ yr^{-1} kpc^{-2}. For smaller values of SFR/Area, the lower level of agreement is probably an indication of the existence of secondary heating mechanisms in the outer parts of galaxies where the star formation rate is low and which are not taken into account in our simulations such as the existence of a background heating due to the photoelectric effect, cosmic rays and soft X-rays which help maintain the low density gas in the outer parts of galaxies at temperatures higher than 100 K and thereby broaden the velocity profile of the gas when observed in the 21 cm H I line. We have discussed the need for improved numerical models which take into account more sophisticated descriptions of the physical processes that may affect the global dynamical properties of the gas such as the effect of the previously mentioned background heating, stratification of the gas in the galaxy, the effect of metallicity which affects the efficiency of the cooling process and the effects of a non-equilibrium chemistry.

Chapter 7

Conclusions and perspectives

7.1 Conclusions

In this thesis, we have investigated several aspects of the interstellar medium (ISM) structure and dynamics. In Chap. 1, we reviewed the most relevant observed properties of the ISM which are, in particular : The different phases of the ISM (molecular gas, neutral gas, ionized gas and dust), their distribution in galaxies and the observational techniques astronomers use nowadays to monitor them along with a mention of the most powerful instruments used for that purpose. We also discussed the role of some physical processes such as magnetic fields and cosmic rays, despite they are not explicitly taken into account in our model, with the aim of providing the reader with a more complete picture about the complexity of the ISM. In the second part of this chapter, we discussed the origin and effects of turbulence which is observed on many scales in the ISM. We particularly focused our discussion on the interesting problem concerning the origins of the support molecular clouds seem to enjoy against the effects of gravity and the plausible role turbulence may play in that context. We ended this chapter by presenting the most relevant turbulence drivers on the many scales in the ISM and their energy input into the galaxy. In the second chapter, we have discussed technical aspects of relevance to this thesis, namely the numerical code we have used to model the ISM, the clump finding algorithm we have used to search for condensations and quantify their properties and the scheme we have used to generate artificial turbulence in the interstellar medium. In Chap. 3, we have discussed the conditions under which a medium becomes unstable against thermal perturbations (thermal instability, TI) and gravitational perturbations (gravitational instability, GI) and discussed the role of stabilizing effects as for example the role of thermal conduction which tends to erase the effects of TI.

Chap. 4 is mainly devoted to study the role of TI and GI on the structure and the dynamics of the ISM using a simple description of the cooling and heating functions of the gas. The models we have used here were local, three-dimensional models of the ISM on a 1 kpc scale with a decaying turbulence, that is, the medium contains a certain amount of kinetic energy initially and is left to evolve afterwards without any further injection of kinetic energy. With this approach, we aimed at answering questions like : does TI lead to the formation of molecular clouds ? can TI drive a self-sustained turbulence ? what are the properties of the molecular clouds that are eventually formed by TI ? The basic answers we obtained to these questions are :

- TI is able to compress diffuse interstellar (of number density ~ 0.5 cm^{-3}) gas by a factor of $1-210^2$, which leads to the transformations of neutral gas into dense and cold molecular gas. In the case of massive condensations (i.e., molecular clouds or large complexes of cold neutral gas), the effects of the self-gravity of the gas may become important and the central densities in the clouds may rise drastically until the cloud reach the stage of gravitational collapse.

- TI, in the absence of any gravitational collapse which converts efficiently gravitational energy into kinetic energy, is unable to generate a self-sustained turbulence in the ISM. We have showed that kinetic energy decays in a cooling medium even faster than in an isothermal medium. We find, in agreement with other studies, that TI is only able to generate a weak turbulence on the smallest scales which are the order $\lesssim 60$ pc.

- We have searched, for the condensations formed after the occurrence of TI in our simulations, for Larson-type relations. These relations describe the condensations mass spectrum and the correlations that exist between the size of the condensations and their average density and characteristic velocity dispersion. Our analysis show that, with some scatter, particularly for the smallest condensations, the Larson relations are inherited by the condensations after the occurrence of TI, which is an indication of the relevance of TI as an agent of structure formation in the ISM.

Until very recently, it was believed that the H I hole and shell-like structure observed in ISM of many galaxies can only be the result of supernova expanding shells. New theoretical and observational evidences challenge this picture, particularly in the case of gas-rich, dwarf irregular galaxies. On the observational side, Rhode et al. (1999) used deep photometry to search for remnant stellar clusters inside the H I holes of the Holmberg II (Ho II) galaxy, which should be observed within their detection limit. However, 86 percent of the H I holes in Ho II show no associated remnant stellar cluster, thus discrediting the hypothesis that the holes could have been formed by supernova explosions. In the case of the LMC, Wada et al. (2000) showed that the large scale H I structure and the CO clouds mass spectrum are better reproduced with models that do not have star formation included. In their model, shells and holes can form as the combined result of thermal and gravitational instabilities. However, Wada et al. (2000) did not perform any analysis of the gas morphology in order to link the morphology to the gas physics. Using the ZEUS code (Stone and Norman 1992a), we performed local, 3D numerical simulations of driven turbulence including heating, cooling, and the self-gravity of the gas (Dib and Burkert 2004a). In a second step, we built 21 cm line emission maps from the data cubes. In order to quantify the comparison between our synthetic H I maps and the observations, we calculated the autocorrelation length-physical scale relation ($L - L_{cr}$ relation) for different models (i.e., different cooling rates) and compared it to the relation we found from the H I map of Ho II. The best agreement was found when turbulence is coupled to a weak efficiency cooling. We also show that the turnover point in the $L - L_{cr}$ relation is directly associated with the energy injection scale. Though we were not able to define the nature of the turbulence driver in Ho II, it was possible to determine its length-scale ($\sim$ 6 kpc). This is much larger than the scale implied by supernova explosions. The large scale driving in Ho II is consistent with the result found by Stanimirović and Lazarian (2001) for the Small Magellanic Cloud (SMC). The kinetic energy spectra they have drawn for the SMC shows no sign of energy injection up to the largest

scale they have considered (4 kpc). The results found for Ho II and the SMC are probably an indication that processes such as tidal interactions and ram pressure stripping might be playing an important role in stirring the gas on large scales in these galaxies. Whereas tidal interaction is clearly a process which affects the SMC, the observations of Bureau et al. (2004) for Ho II remain so far non conclusive about the role played by tidal interactions in this galaxy.

In most spiral galaxies, the velocity dispersion of the gas is observed to vary radially from 12-15 km/s in the central parts of the galaxy and flattens around 4-6 km s^{-1} in the outer H I layers (e.g., Dickey et al. 1990 for NGC 1058). Additionally, when the characteristic velocity dispersion of individual galaxies is plotted versus the star formation rate, it shows a similar behavior (see Fig. 6.2). The constancy and homogeneity of the velocity dispersion in the outer parts of galactic disks where star formation rates drop rapidly and the relation that exists between the star formation rate and the velocity dispersion of the gas are still unresolved issues. In Chap. 6, Using the ZEUS code, we performed local, three-dimensional numerical simulations of supernova driven turbulence in order to investigate the relationship that exist between the velocity dispersion of the gas, the supernova rate and supernova feedback efficiency. Our aim is also to investigate whether the constancy of the velocity dispersion in the outer parts of galactic disks can be explained by the effect of star formation alone. We compare the results of our models by deriving the velocity dispersion σ from a Gaussian fitting of the line of sight velocity profile and after correcting for effects such as thermal broadening. We also derive in a similar fashion the velocity dispersion associated with the H I gas only ($T \leq 12000$). When comparing to the observations, the SN rate per unit volume has been transformed to a star formation rate per unit surface. Our results show that :

- In the $\sigma - \eta$ (equivalently the σ-SFR/Area) relation, the position of the transition to the starburst regime (i.e., location of sharp increase in the velocity dispersion) at around $\eta/\eta_G \sim 0.5$ (SFR/Area $\simeq 5 \times 10^{-3} - 10^{-2}$ $M_\odot$ yr^{-1} kpc^{-2}), where η_G is the Galactic supernova rate, which is observed in the simulations, is relatively in good agreement with the observations in NGC 628 and NGC 6949. It is also in very good agreement with the transition to the starburst regime observed in Fig. 6.2.

- There is good agreement between our models and the observations at the high SN rate values within $2 - 3$ km s^{-1}. This difference can be easily explained by the effect of beam smearing which tends to increase the observed velocity dispersions, particularly in the inner regions of galaxies.

- At the intermediate and low SN rate values, σ and $\sigma_{\rm H\,I}$ are independent of the SN rate for values of $\eta/\eta_G \leq 0.5$, leveling off at a value of ~ 3 km s^{-1} below the observed values by a factor of 2-3. The values of σ and $\sigma_{\rm H\,I}$ become very similar at the low rate values as most of the gas in these simulations has a temperature below 12000 K. On the other hand, no H I is found in the simulations with $\eta/\eta_G \geq 1$. A good agreement can still be observed, at least between the $\eta - \sigma$ relation and the observations when the SN rate and the average density of the medium are chosen such that they follow an empirical star formation law (i.e., we used a Kennicutt law). In that case σ is seen to flatten at the low SN rate values at ~ 5.5 km s^{-1} in good agreement with the observations.

7.2 Perspectives

As already mentioned in each chapter, the results of the research presented in this thesis need necessarily to be developed in many aspects. A central problem that has been investigated in this thesis is that of star formation and supernova feedback. It is now a well established fact that the star formation rate in galactic disks seems to be closely related to the local density of molecular hydrogen (H_2) (Wong and Blitz 2002). Additionally, Blitz and Rosolowsky (2004) have observed in a sample of 28 galaxies that the stellar surface density, in all galaxies, nears a constant value of ~ 120 $M_\odot$ pc^{-2} at the radius where the molecular and atomic hydrogen surface densities are equal. If this value proves indeed to be universal, it might set the ground for a physically motivated star formation recipe. In order to gain a better understanding on the process of star formation, it is therefore crucial to investigate what determines the molecular gas surface density.

Motivated by these observations, we have incorporated into the ZEUS code a detailed network to calculate locally the abundance of the H_2 molecule. We follow the time evolution of the H_2 number density by solving a network which includes : The triple neutral hydrogen reaction path and the corresponding inverse reaction, the H_2 formation and destruction on dust particles (with a fixed dust to gas number densities ratio) and the process of the H_2 photodissociation by UV radiation (see Lepp and Shull 1983; Abel et al. 1997). The radiation field is a free parameter of the model but can be later on evaluated from the total galactic star formation rate or constrained at different galactic radii from observations. We evaluate the local electron number density based on the local temperature value after a calibration with the results of a detailed chemical network (this particular point is done in collaboration with Dmitry Semenov, MPIA/Heidelberg). The models include also a detailed description of the cooling and heating rates of the gas. Namely we account for : Heating by the photoelectric effect (Hollenbach and McKee 1989; Wolfire et al. 1995) which is regulated by the radiation field; heating by cosmic rays (Wolfire et al. 1995); heating from soft X-rays (Wolfire et al. 1995); UV heating from the ionization of neutral atoms (Dalgarno and McCray 1972); electron density-dependent radiative cooling (Dalgarno and McCray (1972)). Taking into account the electron-dependency of the cooling curve is crucial as the cooling rate may vary by 2-3 order of magnitudes depending on the electron fraction; cooling from the electron recombination onto positively charged grains (Wolfire et al. 1995); cooling from Bremsstrahlung radiation for temperatures larger than 10^4 K (Smith and Rosen 2003); cooling from dust-gas collisions (Hollenbach and McKee 1989; Smith and Rosen 2003); heating resulting from the reformation of the H_2 molecule and the cooling from the vibrational and rotational modes as well as the cooling associated with dissociation of H_2 (Lepp and Shull 1983; Smith and Rosen 2003). An extension of the code is also foreseen in order to include the cooling through rotational and vibrational modes of CO induced by collisions with both atomic and molecular hydrogen. By introducing the H_2 chemistry into our code we principally aim at estimating on the small scales the accumulation time that is needed to form molecular hydrogen (i.e., time needed to transform neutral hydrogen into molecular hydrogen or, equivalently, time needed until H_2 reaches a high enough column density to shield itself against UV radiation) under different conditions of compression (i.e., strength of shocks), local density and the radiation field. Such a relation coming from the modeling, on small scales ($\sim$ 1-10 pc), in media subject to different physical conditions would be used in the large scale ($\sim$ 1 kpc) simulations in order to estimate the local H_2 fraction and the efficiency of star formation. In the points developed below we

discuss some problems that we thinks are worthwhile investigating in more detail :

7.2.1 On the small scales

Detailed fragmentation in a post-shock region : We intend to investigate with 2D and 3D numerical simulations a scenario for low-mass star formation and eventually Brown Dwarf formation in which low mass objects can form by thermal fragmentation in post-shock regions in the Cold Neutral Medium (CNM) and Warm Neutral Medium (WNM) without the usual accompanying higher mass stellar spectrum. Our work is motivated by the simulations of Koyama and Inutsuka (2000, 2002, 2004) and Bergin et al. (2004) in which they find strong condensations in the post-shock regions, especially in the case of strong shocks. However, the latter simulations, in addition of being mostly restricted to 1D, do not include the effect of the gas self-gravity which might change significantly the future evolution of the pre-stellar cores. Additionally, due to the low dimensionality of the latter simulations, the authors could not perform any measurements of the individual properties of the cores such as their mass and angular momentum, which we are intend and are able to do with the above mentioned code and the analysis tools presented in Chap. 2.2. The basic parameters of the model are the relative velocity of the shock and the value of the interstellar radiation field which regulates the balance of cooling and heating. We also plan to include the effects of magnetic fields which will tend to broaden the shock region and reduce the compression factor. We intend to compare our results with recently obtained proto-stellar mass spectra like the mass spectrum of the Rho Ophiuchi A molecular cloud which extends down to the sub-stellar regime (Khanzadyan et al. 2004; Stanke et al. 2004, submitted).

Building the initial conditions for Brown Dwarf formation : Recent findings indicate that, while the IMF for low mass stars seems to be rather independent of the star-forming regions, it does not seem to be the case for sub-stellar objects (Briceño et al. 2002; Kroupa and Bouvier 2003). This emphasizes the importance of investigating the initial conditions of Brown Dwarfs formation further, especially the initial conditions of the emerging cluster of pre-stellar cores. Using the results of our thermal fragmentation calculations in post-shock regions, we intend to describe the properties of the forming cluster of fragments and follow its further evolution by means of N-Body simulations. This way, we expect to derive binary fractions and binary properties of Brown Dwarfs which are crucial in order to distinguish between the different formation scenarios. It would be also very interesting to verify under which conditions the ejection scenario of Reipurth and Clarke (2001).

The existence of $< n > -\sigma$ relation : As discussed in Chap. 4, the ISM structure and dynamics are often described with scaling laws known as the Larson relations (Larson 1981). Whereas the velocity dispersion-radius relation ($\sigma - R$) has been found in numerical simulations of decaying and driven turbulence (e.g., Chap. 4 in this thesis), the existence of the mean density-radius relation ($< n > -R$) is still a matter of debate. Recently, Ballesteros-Paredes (2004) analysed condensations in supersonic, isothermal, MHD simulations. They found that the average density of the projected clumps is independent of their radius. This contrasts our findings for simulations that include cooling, heating, and gravity (Dib, Burkert & Hujeirat 2004, Chap. 4 : Fig. 4.17). However, we have searched for the relation directly in the 3D data whereas Ballesteros-Paredes and Mac Low (2002) performed their analysis on

the 2D line of sight integrated density maps. It could be simply that the $< n > -R$ relation would not show up in isothermal simulations due to the small over-densities which can form there in contrast to simulations which include cooling and gravity, therefore yielding nearly constant column densities. A more careful study should be performed in order to unveil the existence of this relation under different conditions such as a different balance of the cooling and heating processes and at different stages of the gravitational contraction. A comparison of the 2D and 3D data relations from the same simulations is also needed in order to better understand the effects of projection.

7.2.2 On the large scales

The effects of metallicity and star formation on the global gas morphology : In connection with Chap. 5, we are interested in investigating the relationship that may exist between the structure function index α ($S(l) = l^{\alpha}$, where l is the physical scale) of the H I gas and the global metallicity of the galaxy. Such a relation might exist for dwarf irregular galaxies with small star formation rates and where the gas morphology is likely to be shaped by the interplay of turbulence and the thermodynamical properties of the gas. By building a large library of models including also star formation and feedback, it might also be possible to uncover the relation that exists between the structure function index, the metallicity, and the star formation rate. It is not yet known whether a combination of the metallicity (or a radially dependent metallicity profile) and a radially dependent star formation rate can lead to a unique, non degenerate, large scale morphology of the gas. The ZEUS code is particularly suited for this project. In addition to the energy feedback from stars, we intend to implement sink particles in the ZEUS code to mimick the stellar populations, allowing for an exchange of mass (and metals) between stars and the ISM. Establishing such relations between the gas morphology and metallicity (eventually with a radial dependence) would be extremely useful for determining the metallicity of galaxies in a very simple way from their gas morphologies. Interestingly, Dr Fabian Walter (MPIA, Heidelberg) and Dr. Martin Bureau (Oxford) have recently obtained a large sample of H I observations ($\sim$ 40 galaxies) with the VLA, among them are $\sim$ 10 gas rich dwarf irregular galaxies of different metallicities which can serve as the perfect observational sample to compare our models with.

Towards a physical criterion for star formation :Blitz and Rosolowsky (2004), in deriving the value of stellar surface density at the transition radius in the sample of galaxies they have studied (radius where H I and H_2 densities are equal), made the simple assumption that the gas in the galactic disk is, on average, in hydrostatic equilibrium. Using this assumption and a number of other simplifications, they argued that the hydrostatic equilibrium pressure is primarily related to the stellar surface density. Regarding the large number of assumptions made in this scenario, and the independance of the hydrostatic pressure from the gas surface density, it is crucial to test it with numerical simulations. Our version of the ZEUS code which already contains the chemistry of the H_2 molecule is particularly suited for this study. However addressing this problem numerically requires resolving the H_2 abundance locally, therefore high resolution 2D models are preferred. High resolution 2D axisymmetric models including the H_2 chemistry and star formation would help identify the vertical and radial correlation between the H_2 fraction and the star formation rate whereas using the vertical symmetry and modeling the (r,θ) disk (including spiral arms) would help constrain the H_2 fraction radial dependence with the star formation rate in the presence of the spiral structure.

The effects of gas infall to the galactic disk on star formation will also be investigated in this context.

7.2.3 AMR codes

We intend to continue learning a new numerical tool, namely, the adaptative mesh refinement (AMR) code FLASH. With FLASH, many astrophysical problems should be revisited. A particularly interesting astrophysical application for an AMR code is the protostellar collapse problem. This problem has been mainly adressed so far with SPH simulations, known to be very dissipative, a fact that can alter the dynamics in the innermost parts of the collapsing core. Another interesting area of application for an AMR code is the supernova driven turbulence problem which has been already investigated with the ZEUS code in this thesis (in Chap. 6). AMR methods are particularly suited for this problem as they allow for an enhanced resolution in the dense cooling shells of the supernova remnants. So far, only one person is currently performing such simulations (de Avillez 2000; de Avillez and Breitschwerdt 2004a) with a (non-public) AMR code. More generally, up to now, a benchmark for codes simulating the supernova driven turbulence does not exist. It would be of a large interest to the community if such benchmark existed. We intend to do simulations with ZEUS and FLASH (for a start) with similar setups. The comparison will include calculating the volum filling factors and quantities like the dimensionless kinetic energy dissipation rate $C_\epsilon = \epsilon \times L/v_{rms}^3$ where ϵ is the energy dissipation rate, L the characteristic scale and v_{rms} the *rms* velocity (de Avillez and Breitschwerdt 2004b). We will also seek to establish a comparison of the results for a similar setup problem with other authors who are currently modelling the supernova driven ISM. (de Avillez 2000; de Avillez and Breitschwerdt 2004a; Korpi et al. 1999a,b; Kim et al. 2001).

Appendix A

Code scaling prescriptions

$$velocity\ [m\ s^{-1}\ ]:\ 1\ \hat{v}\ [ms^{-1}] = \left(\frac{\gamma}{\mu}\right)^{-1/2}\ \left(\frac{k_b T_4}{m_H}\right)^{1/2}, \tag{A.1}$$

$$time\ [s]\ :\ 1\ \hat{t} = \frac{1}{\mu^{1/2}}\ 0.2993 \times 10^{17} n_4^{-1/2}, \tag{A.2}$$

$$lenght\ [m]\ :\ 1\ \hat{L} = \frac{\gamma^{1/2}}{\mu}\ 0.2719 \times 10^{21} T_4^{1/2} n_4^{1/2}, \tag{A.3}$$

$$density\ [kg\ m^{-3}]\ :\ 1\ \hat{\rho} = \mu\ 1.6726 \times 10^{-23} n_4, \tag{A.4}$$

$$energy/unit\ volume\ [J\ m^{-3}]\ :\ 1\ \hat{e} = (\gamma - 1)\ 1.38066 \times 10^{-15} T_4 n_4, \tag{A.5}$$

$$mass\ [kg]\ :\ 1\ \hat{M} = \frac{\gamma^{3/2}}{\mu^2}\ 0.033 \times 10^{40} T_4^{3/2} n_4^{-1/2}, \tag{A.6}$$

$$angular\ momentum\ [kg\ m\ s^{-1}]\ :\ 1\ \hat{J} = \frac{\gamma}{\mu^{3/2}}\ 0.247 T_4^{1/2} n_4^{-1/2} \tag{A.7}$$

$$energy\ [J]\ :\ 1\ \hat{E} = \frac{\gamma^{5/2}}{\mu^3}\ 2.71 \times 10^{46} T_4^{5/2} n_4^{-1/2}, \tag{A.8}$$

$$gravitational\ potential\ [m^2\ s^{-2}]\ :\ 1\ \hat{\phi} = \frac{\gamma}{\mu}\ 0.825 \times 10^{8} T_4, \tag{A.9}$$

Bibliography

Abbott, D. C.: 1982, The return of mass and energy to the interstellar medium by winds from early-type stars, *Astrophysical Journal* **263**, 723

Abel, T., Anninos, P., Zhang, Y., and Norman, M. L.: 1997, Modeling primordial gas in numerical cosmology, *New Astronomy* **2**, 181

Anders, E. and Grevesse, N.: 1989, Abundances of the elements - Meteoritic and solar, *Geochimica and Chosmochimica Acta* **53**, 197

Armstrong, J. W., Rickett, B. J., and Spangler, S. R.: 1995, Electron density power spectrum in the local interstellar medium, *Astrophysical Journal* **443**, 209

Aschenbach, B.: 1988, Recent X-Ray Observations of Supernova Remnants and Their Interpretation *in IAU Colloq. 101: Supernova Remnants and the Interstellar Medium*, p. 99

Balbus, S. A.: 1985, Classical thermal evaporation of clouds - an electrostatic analogy, *Astrophysical Journal* **291**, 518

Balbus, S. A. and Hawley, J. F.: 1991, A powerful local shear instability in weakly magnetized disks. I - Linear analysis. II - Nonlinear evolution, *Astrophysical Journal* **376**, 214

Ballesteros-Paredes, J.: 2004, Molecular Clouds: Formation and Disruption, *Astrophysics and Space Science* **289**, 243

Ballesteros-Paredes, J., Hartmann, L., and Vázquez-Semadeni, E.: 1999a, Turbulent Flow-driven Molecular Cloud Formation: A Solution to the Post-T Tauri Problem?, *Astrophysical Journal* **527**, 285

Ballesteros-Paredes, J., Klessen, R. S., and Vázquez-Semadeni, E.: 2003, Dynamic Cores in Hydrostatic Disguise, *Astrophysical Journal* **592**, 188

Ballesteros-Paredes, J. and Mac Low, M.: 2002, Physical versus Observational Properties of Clouds in Turbulent Molecular Cloud Models, *Astrophysical Journal* **570**, 734

Ballesteros-Paredes, J., Vázquez-Semadeni, E., and Scalo, J.: 1999b, Clouds as Turbulent Density Fluctuations: Implications for Pressure Confinement and Spectral Line Data Interpretation, *Astrophysical Journal* **515**, 286

Bania, T. M. and Lyon, J. G.: 1980, OB stars and the structure of the interstellar medium - Cloud formation and effects of different equations of state, *Astrophysical Journal* **239**, 173

Beck, R.: 2001, Galactic and Extragalactic Magnetic Fields, *Space Science Reviews* **99**, 243

Beck, R.: 2004, The Role of Magnetic Fields in Spiral Galaxies, *Astrophysics and Space Science* **289**, 293

Beck, R., Brandenburg, A., Moss, D., Shukurov, A., and Sokoloff, D.: 1996, Galactic Magnetism: Recent Developments and Perspectives, *Annual Review of Astronomy and Astrophysics* **34**, 155

Bergin, E. A., Hartmann, L. W., Raymond, J. C., and Ballesteros-Paredes, J.: 2004, Molecular Cloud Formation behind Shock Waves, *Astrophysical Journal* **612**, 921

Binney, J. and Tremaine, S.: 1987, *Galactic dynamics*, Princeton, NJ, Princeton University Press

Blandford, R. and Eichler, D.: 1987, Particle Acceleration at Astrophysical Shocks - a Theory of Cosmic-Ray Origin, *Physical Reports* **154**, 1

Blandford, R. D. and Ostriker, J. P.: 1978, Particle acceleration by astrophysical shocks, *Astrophysical Journal Letters* **221**, L29

Blitz, L.: 1993, Giant molecular clouds *in Protostars and Planets III.*, p. 125

Blitz, L. and Rosolowsky, E.: 2004, The Role of Pressure in Giant Molecular Cloud Formation, *Astrophysical Journal Letters* **612**, L29

Blitz, L. and Shu, F. H.: 1980, The origin and lifetime of giant molecular cloud complexes, *Astrophysical Journal* **238**, 148

Boehringer, H. and Hensler, G.: 1989, Metallicity-dependence of radiative cooling in optically thin, hot plasmas, *Astronomy and Astrophysics* **215**, 147

Bohlin, R. C., Savage, B. D., and Drake, J. F.: 1978, A survey of interstellar H I from L-alpha absorption measurements. II, *Astrophysical Journal* **224**, 132

Bonazzola, S., Heyvaerts, J., Falgarone, E., Perault, M., and Puget, J. L.: 1987, Jeans collapse in a turbulent medium, *Astronomy and Astrophysics* **172**, 293

Boroson, T.: 1981, The distribution of luminosity in spiral galaxies, *Astrophysical Journal Supplement Series* **46**, 177

Boulanger, F., Abergel, A., Bernard, J.-P., Burton, W. B., Desert, F.-X., Hartmann, D., Lagache, G., and Puget, J.-L.: 1996, The dust/gas correlation at high Galactic latitude., *Astronomy and Astrophysics* **312**, 256

Boulanger, F., Boisssel, P., Cesarsky, D., and Ryter, C.: 1998, The shape of the unidentified infra-red bands: analytical fit to ISOCAM spectra, *Astronomy and Astrophysics* **339**, 194

Boulanger, F. and Pérault, M.: 1988, Diffuse infrared emission from the galaxy. I - Solar neighborhood, *Astrophysical Journal* **330**, 964

Boulares, A. and Cox, D. P.: 1990, Galactic hydrostatic equilibrium with magnetic tension and cosmic-ray diffusion, *Astrophysical Journal* **365**, 544

Brandenburg, A., Nordlund, A., Stein, R. F., and Torkelsson, U.: 1995, Dynamo-generated Turbulence and Large-Scale Magnetic Fields in a Keplerian Shear Flow, *Astrophysical Journal* **446**, 741

Briceño, C., Luhman, K. L., Hartmann, L., Stauffer, J. R., and Kirkpatrick, J. D.: 2002, The Initial Mass Function in the Taurus Star-forming Region, *Astrophysical Journal* **580**, 317

Brogan, C. L., Frail, D. A., Goss, W. M., and Troland, T. H.: 2000, OH Zeeman Magnetic Field Detections toward Five Supernova Remnants Using the VLA, *Astrophysical Journal* **537**, 875

Bronfman, L., Casassus, S., May, J., and Nyman, L.-Å.: 2000, The radial distribution of OB star formation in the Galaxy, *Astronomy and Astrophysics* **358**, 521

Bureau, M. and Carignan, C.: 2002, Environment, Ram Pressure, and Shell Formation in Holmberg II, *Astronomical Journal* **123**, 1316

Bureau, M., Walter, F., van Gorkom, J., and Carignan, C.: 2004, HI and Hot Gas in the Outskirts of the M81 Group, *IAU Symposium* p. 452

Burgers, J. M.: 1974, *The nonlinear Diffusion Equation*, Dordrecht : Reidel

Burkert, A. and Bodenheimer, P.: 1993, Multiple Fragmentation in Collapsing Protostars, *Monthly Notices of the Royal Astronomical Society* **264**, 798

Burkert, A. and Lin, D. N. C.: 2000, Thermal Instability and the Formation of Clumpy Gas Clouds, *Astrophysical Journal* **537**, 270

Cappellaro, E., Evans, R., and Turatto, M.: 1999, A new determination of supernova rates and a comparison with indicators for galactic star formation, *Astronomy and Astrophysics* **351**, 459

Cardelli, J. A., Meyer, D. M., Jura, M., and Savage, B. D.: 1996, The Abundance of Interstellar Carbon, *Astrophysical Journal* **467**, 334

Carr, J. S.: 1987, A study of clumping in the Cepheus OB 3 molecular cloud, *Astrophysical Journal* **323**, 170

Caselli, P. and Myers, P. C.: 1995, The Line Width–Size Relation in Massive Cloud Cores, *Astrophysical Journal* **446**, 665

Casoli, F., Sauty, S., Gerin, M., Boselli, A., Fouque, P., Braine, J., Gavazzi, G., Lequeux, J., and Dickey, J.: 1998, Molecular gas in spiral galaxies, *Astronomy and Astrophysics* **331**, 451

Cernicharo, J.: 1991, The Physical Conditions of Low Mass Star Forming Regions *in NATO ASIC Proc. 342: The Physics of Star Formation and Early Stellar Evolution*, p. 287

Cesarsky, D., Lequeux, J., Abergel, A., Perault, M., Palazzi, E., Madden, S., and Tran, D.: 1996, Infrared spectrophotometry of NGC 7023 with ISOCAM., *Astronomy and Astrophysics* **315**, L305

Chandran, B. D. G. and Cowley, S. C.: 1998, Thermal Conduction in a Tangled Magnetic Field, *Physical Review Letters* **80**, 3077

Chandrasekhar, S.: 1951, ., Vol. 210, Proc. R. Soc. London A

Chandrasekhar, S.: 1961, *Hydrodynamic and hydromagnetic stability*, International Series of Monographs on Physics, Oxford: Clarendon, 1961

Chevalier, R. A.: 1974, The Evolution of Supernova Remnants. Spherically Symmetric Models, *Astrophysical Journal* **188**, 501

Chevalier, R. A.: 1977, The interaction of supernovae with the interstellar medium, *Annual Review of Astronomy and Astrophysics* **15**, 175

Chiang, W. and Bregman, J. N.: 1988, A model for the interaction between stars and gas in the interstellar medium, *Astrophysical Journal* **328**, 427

Chiang, W.-H. and Prendergast, K. H.: 1985, Numerical study of a two-fluid hydrodynamic model of the interstellar medium and population I stars, *Astrophysical Journal* **297**, 507

Cho, J. and Lazarian, A.: 2003, Compressible magnetohydrodynamic turbulence: mode coupling, scaling relations, anisotropy, viscosity-damped regime and astrophysical implications, *Monthly Notices of the Royal Astronomical Society* **345**, 325

Cho, J., Lazarian, A., and Vishniac, E. T.: 2003, Ordinary and Viscosity-damped Magnetohydrodynamic Turbulence, *Astrophysical Journal* **595**, 812

Cho, J., Lazarian, A., and Yan, H.: 2002, Scaling of ISM Turbulence: Implications for H I *in ASP Conf. Ser. 276: Seeing Through the Dust: The Detection of HI and the Exploration of the ISM in Galaxies*, p. 170

Chyży, K. T., Beck, R., Kohle, S., Klein, U., and Urbanik, M.: 2000, Regular magnetic fields in the dwarf irregular galaxy NGC 4449, *Astronomy and Astrophysics* **355**, 128

Clayton, G. C., Anderson, C. M., Magalhaes, A. M., Code, A. D., Nordsieck, K. H., Meade, M. R., Wolff, M. J., Babler, B., Bjorkman, K. S., Schulte-Ladbeck, R. E., Taylor, M., and Whitney, B. A.: 1992, The first spectropolarimetric study of the wavelength dependence of interstellar polarization in the ultraviolet, *Astrophysical Journal Letters* **385**, L53

Combes, F.: 2004, The Cold Universe, *Saas-Fee Advanced Course 32, Springer-Verlag, 2004. Edited by A.W. Blain, F. Combes, B.T. Draine, D. Pfenniger and Y. Revaz.*

Cowie, L. L. and McKee, C. F.: 1977, The evaporation of spherical clouds in a hot gas. I - Classical and saturated mass loss rates, *Astrophysical Journal* **211**, 135

Cox, D. P.: 2004, In ISM Modeling, The Devil is in the Details: You Show Me Your OVI and I'll Show You Mine, *Astrophysics and Space Science* **289**, 469

Cox, D. P. and Smith, B. W.: 1974, Large-Scale Effects of Supernova Remnants on the Galaxy: Generation and Maintenance of a Hot Network of Tunnels, *Astrophysical Journal Letters* **189**, L105

Dahlem, M., Ehle, M., Jansen, F., Heckman, T. M., Weaver, K. A., and Strickland, D. K.: 2003, The quest for hot gas in the halo of NGC 1511, *Astronomy and Astrophysics* **403**, 547

Dalgarno, A. and McCray, R. A.: 1972, Heating and Ionization of HI Regions, *Annual Review of Astronomy and Astrophysics* **10**, 375

Dame, T. M., Elmegreen, B. G., Cohen, R. S., and Thaddeus, P.: 1986, The largest molecular cloud complexes in the first galactic quadrant, *Astrophysical Journal* **305**, 892

Davies, G. and Widrow, L. M.: 2000, A Possible Mechanism for Generating Galactic Magnetic Fields, *Astrophysical Journal* **540**, 755

Davis, L. J. and Greenstein, J. L.: 1951, The Polarization of Starlight by Aligned Dust Grains., *Astrophysical Journal* **114**, 206

de Avillez, M. A.: 2000, Disc-halo interaction - I. Three-dimensional evolution of the Galactic disc, *Monthly Notices of the Royal Astronomical Society* **315**, 479

de Avillez, M. A. and Breitschwerdt, D.: 2004a, Volume filling factors of the ISM phases in star forming galaxies. I. The role of the disk-halo interaction, *Astronomy and Astrophysics* **425**, 899

de Avillez, M. A. and Breitschwerdt, D.: 2004b, Volume filling factors of the ISM phases in star forming galaxies. I. The role of the disk-halo interaction, *Astronomy and Astrophysics* **425**, 899

de Jager, G. and Davies, R. D.: 1971, Neutral hydrogen in M 33., *Monthly Notices of the Royal Astronomical Society* **153**, 9

Dib, S. and Burkert, A.: 2004a, On the origin of the HI holes in the interstellar medium of dwarf irregular galaxies, *ArXiv Astrophysics e-prints, astro-ph/0402593*

Dib, S. and Burkert, A.: 2004b, The Origin of the H I Holes in the Interstellar Medium of Holmberg II, *Astrophysics and Space Science* **292**, 135

Dib, S., Burkert, A., and Hujeirat, A.: 2004, On the thermal instability in numerical models of the interstellar medium, *Astrophysics and Space Science* **289**, 465

Dickey, J. M., Hanson, M. M., and Helou, G.: 1990, NGC 1058 - Gas motions in an extended, quiescent spiral disk, *Astrophysical Journal* **352**, 522

Dickey, J. M. and Lockman, F. J.: 1990, H I in the Galaxy, *Annual Review of Astronomy and Astrophysics* **28**, 215

Dopita, M. A. and Ryder, S. D.: 1994, On the law of star formation in disk galaxies, *Astrophysical Journal* **430**, 163

Draine, B.: 1989, On the Interpretation of the λ 2175 Å Feature *inIAU Symp. 135: Interstellar Dust*, p. 313

Draine, B.: 2004, The Cold Universe, *Saas-Fee Advanced Course 32, Springer-Verlag, 2004. Edited by A.W. Blain, F. Combes, B.T. Draine, D. Pfenniger and Y. Revaz.*

Draine, B. T.: 1990, Evolution of interstellar dust it in ASP Conf. Ser. 12: The Evolution of the Interstellar Medium, p. 193

Dziourkevitch, N., Elstner, D., and Rüdiger, G.: 2004, Interstellar turbulence driven by the magnetorotational instability, *Astronomy and Astrophysics* **423**, L29

Ehlerová, S., Palouš, J., and Wünsch, R.: 2004, HI shells in the Leiden-Dwingeloo HI survey, *Astrophysics and Space Science* **289**, 279

Elmegreen, B. G.: 1992, *The galactic interstellar medium Springer-Verlag, eds. Pfenninger, D. and Bartholdi, P.*

Elmegreen, B. G.: 1997, Intercloud Structure in a Turbulent Fractal Interstellar Medium, *Astrophysical Journal* **477**, 196

Elmegreen, B. G.: 2000, Star Formation in a Crossing Time, *Astrophysical Journal* **530**, 277

Elmegreen, D. M. and Elmegreen, B. G.: 1984, Blue and near-infrared surface photometry of spiral structure in 34 nonbarred grand design and flocculent galaxies, *Astrophysical Journal Supplement Series* **54**, 127

Fabbiano, G.: 1989, X rays from normal galaxies, *Annual Review of Astronomy and Astrophysics* **27**, 87

Faison, M. D. and Goss, W. M.: 2001, The Structure of the Cold Neutral Interstellar Medium on 10-100 AU Scales, *Astronomical Journal* **121**, 2706

Falgarone, E., Phillips, T. G., and Walker, C. K.: 1991, The edges of molecular clouds - Fractal boundaries and density structure, *Astrophysical Journal* **378**, 186

Falgarone, E., Puget, J.-L., and Perault, M.: 1992, The small-scale density and velocity structure of quiescent molecular clouds, *Astronomy and Astrophysics* **257**, 715

Ferguson, A. M. N., Wyse, R. F. G., Gallagher, J. S., and Hunter, D. A.: 1998, Discovery of Recent Star Formation in the Extreme Outer Regions of Disk Galaxies, *Astrophysical Journal Letters* **506**, L19

Ferrara, A. and Shchekinov, Y.: 1993, Dynamics of Conductive/Cooling Fronts: Cloud Implosion and Thermal Solitons, *Astrophysical Journal* **417**, 595

Ferrière, K.: 1992a, Effect of an ensemble of explosions on the Galactic dynamo. I - General formulation, *Astrophysical Journal* **389**, 286

Ferrière, K.: 1992b, Effect of the explosion of supernovae and superbubbles on the Galactic dynamo, *Astrophysical Journal* **391**, 188

Ferrière, K.: 1998a, Global Model of the Interstellar Medium in Our Galaxy with New Constraints on the Hot Gas Component, *Astrophysical Journal* **497**, 759

Ferrière, K.: 1998b, The Hot Gas Filling Factor in Our Galaxy, *Astrophysical Journal* **503**, 700

Ferrière, K. and Schmitt, D.: 2000, Numerical models of the galactic dynamo driven by supernovae and superbubbles, *Astronomy and Astrophysics* **358**, 125

Ferrière, K. M.: 2001, The interstellar environment of our galaxy, *Reviews of Modern Physics* **73**, 1031

Field, G. B.: 1962, *in interstellar matter in galaxies,, Benjamin, New York, ed L. Woltjer* **142**, 531

Field, G. B.: 1965, Thermal Instability., *Astrophysical Journal* **142**, 531

Field, G. B., Goldsmith, D. W., and Habing, H. J.: 1969, Cosmic-Ray Heating of the Interstellar Gas, *Astrophysical Journal Letters* **155**, L149

Field, G. B., Somerville, W. B., and Dressler, K.: 1966, Hydrogen Molecules in Astronomy, *Annual Review of Astronomy and Astrophysics* **4**, 207

Fioc, M. and Rocca-Volmerange, B.: 1997, PEGASE: a UV to NIR spectral evolution model of galaxies. Application to the calibration of bright galaxy counts., *Astronomy and Astrophysics* **326**, 950

Fleck, R. C.: 1981, On the generation and maintenance of turbulence in the interstellar medium, *Astrophysical Journal Letters* **246**, L151

Frisch, U.: 1995, *Turbulence. The legacy of A.N. Kolmogorov*, Cambridge: Cambridge University Press, —c1995

Fuller, G. A. and Myers, P. C.: 1992, Dense cores in dark clouds. VII - Line width-size relations, *Astrophysical Journal* **384**, 523

Gómez, G. C. and Cox, D. P.: 2002, Three-dimensional Magnetohydrodynamic Modeling of the Gaseous Structure of the Galaxy: Setup and Initial Results, *Astrophysical Journal* **580**, 235

Gazol, A., Vázquez-Semadeni, E., Sánchez-Salcedo, F. J., and Scalo, J.: 2001, The Temperature Distribution in Turbulent Interstellar Gas, *Astrophysical Journal Letters* **557**, L121

Gazol-Patiño, A. and Passot, T.: 1999, A Turbulent Model for the Interstellar Medium. III. Stratification and Supernova Explosions, *Astrophysical Journal* **518**, 748

Genzel, R.: 1992, *The galactic interstellar medium Springer-Verlag, eds. Pfenninger, D. and Bartholdi, P.*

Gerritsen, J. P. E. and Icke, V.: 1997, Star formation in N-body simulations. I. The impact of the stellar ultraviolet radiation on star formation., *Astronomy and Astrophysics* **325**, 972

Godunov, S. K.: 1959, *Matematicheskii sbornik*

Goldreich, P. and Sridhar, S.: 1995, Toward a theory of interstellar turbulence. 2: Strong alfvenic turbulence, *Astrophysical Journal* **438**, 763

Goodman, A. A., Barranco, J. A., Wilner, D. J., and Heyer, M. H.: 1998, Coherence in Dense Cores. II. The Transition to Coherence, *Astrophysical Journal* **504**, 223

Gordon, K. J.: 1971, A 21-CENTIMETER Study of the Spiral Galaxy Messier 33, *Astrophysical Journal* **169**, 235

Gorenstein, P., Harnden, F. R., and Tucker, W. H.: 1974, The X-ray spectra of the VELA and Puppis supernova remnants and the shock-wave model of supernova remnants, *Astrophysical Journal* **192**, 661

Graham, R. and Langer, W. D.: 1973, Pressure Equilibrium of Finite-Size Clouds in the Interstellar Medium, *Astrophysical Journal* **179**, 469

Haffner, L. M., Reynolds, R. J., and Tufte, S. L.: 1999, WHAM Observations of Hα, [S II], and [N II] toward the Orion and Perseus Arms: Probing the Physical Conditions of the Warm Ionized Medium, *Astrophysical Journal* **523**, 223

Hall, J. S.: 1949, Observations of the Polarized Light from Stars, *Science* **109**, 166

Hanasz, M., Kowal, G., Otmianowska-Mazur, K., and Lesch, H.: 2004, Amplification of Galactic Magnetic Fields by the Cosmic-Ray-driven Dynamo, *Astrophysical Journal Letters* **605**, L33

Hanasz, M. and Lesch, H.: 2000, Cosmic-Ray Evolution in Parker-unstable Galactic Magnetic Fields, *Astrophysical Journal* **543**, 235

Hanasz, M. and Lesch, H.: 2003, Incorporation of cosmic ray transport into the ZEUS MHD code. Application for studies of Parker instability in the ISM, *Astronomy and Astrophysics* **412**, 331

Harding, D. S. and Harding, A. K.: 1982, The distribution of free electrons in the inner Galaxy from pulsar dispersion measures, *Astrophysical Journal* **257**, 603

Hartmann, D. and Burton, W. B.: 1997, *Atlas of galactic neutral hydrogen*, Cambridge; New York: Cambridge University Press

Haugen, N. E. and Brandenburg, A.: 2004, Inertial range scaling in numerical turbulence with hyperviscosity, *Physical Review E* **70(2)**, 6405

Hawley, J. F. and Balbus, S. A.: 1991, A Powerful Local Shear Instability in Weakly Magnetized Disks. II. Nonlinear Evolution, *Astrophysical Journal* **376**, 223

Hawley, J. F., Wilson, J. R., and Smarr, L. L.: 1984, A numerical study of nonspherical black hole accretion. II - Finite differencing and code calibration, *Astrophysical Journal Supplement Series* **55**, 211

Heiles, C.: 1979, H I shells and supershells, *Astrophysical Journal* **229**, 533

Heiles, C.: 1984, H I shells, supershells, shell-like objects, and 'worms', *Astrophysical Journal Supplement Series* **55**, 585

Heiles, C.: 1987, Supernovae versus models of the interstellar medium and the gaseous halo, *Astrophysical Journal* **315**, 555

Heiles, C.: 2000, 9286 Stars: An Agglomeration of Stellar Polazization Catalogs, *Astronomical Journal* **119**, 923

Heiles, C.: 2001, New Temperatures of Diffuse Interstellar Gas: Thermally Unstable Gas, *Astrophysical Journal Letters* **551**, L105

Heitsch, F.: 2001, Turbulence and fragmentation in molecular clouds, *Ph.D. Thesis*

Heitsch, F., Mac Low, M., and Klessen, R. S.: 2001, Gravitational Collapse in Turbulent Molecular Clouds. II. Magnetohydrodynamical Turbulence, *Astrophysical Journal* **547**, 280

Hennebelle, P. and Pérault, M.: 1999, Dynamical condensation in a thermally bistable flow. Application to interstellar cirrus, *Astronomy and Astrophysics* **351**, 309

Hiltner, W. A.: 1949, On the Presence of Polarization in the Continuous Radiation of Stars. II., *Astrophysical Journal* **109**, 471

Hippelein, H., Haas, M., Tuffs, R. J., Lemke, D., Stickel, M., Klaas, U., and Völk, H. J.: 2003, The spiral galaxy M 33 mapped in the FIR by ISOPHOT. A spatially resolved study of the warm and cold dust, *Astronomy and Astrophysics* **407**, 137

Hollenbach, D. and McKee, C. F.: 1989, Molecule formation and infrared emission in fast interstellar shocks. III - Results for J shocks in molecular clouds, *Astrophysical Journal* **342**, 306

Houlahan, P. and Scalo, J.: 1990, Recognition and characterization of hierarchical interstellar structure. I - Correlation function, *Astrophysical Journal Supplement Series* **72**, 133

Huchtmeier, W. K.: 1973, A neutral hydrogen survey of the galaxy M 33., *Astronomy and Astrophysics* **22**, 91

Hunter, D. A. and Gallagher, J. S.: 1985, Star-forming properties and histories of dwarf irregular galaxies - Down but not out, *Astrophysical Journal Supplement Series* **58**, 533

Jahoda, K., Lockman, F. J., and McCammon, D.: 1990, Galactic H I and the interstellar medium in Ursa Major, *Astrophysical Journal* **354**, 184

Jeans, J. H.: 1902, *Philos. Trans. R. Soc. London A* **199**, 1

Jenkins, E. B.: 2002, Hot Gas in the Milky Way. *in ASP Conf. Ser. 253: Chemical Enrichment of Intracluster and Intergalactic Medium*, p. 365

Jenkins, E. B. and Meloy, D. A.: 1974, A survey with Copernicus of interstellar O VI absorption, *Astrophysical Journal Letters* **193**, L121

Jenkins, E. B. and Savage, B. D.: 1974, Ultraviolet photometry from the orbiting astronomical observatory. XIV. an extension of the survey of Lyman-alf absorption from interstellar hydrogen., *Astrophysical Journal* **187**, 243

Jenniskens, P. and Desert, F.-X.: 1994, A survey of diffuse interstellar bands (3800-8680 A), *Astronomy and Astrophysics Supplement Series* **106**, 39

Jokipii, J. R. and Parker, E. N.: 1969, Cosmic-Ray Life and the Stochastic Nature of the Galactic Magnetic Field, *Astrophysical Journal* **155**, 799

Jones, A. P., Tielens, A. G. G. M., Hollenbach, D. J., and McKee, C. F.: 1994, Grain destruction in shocks in the interstellar medium, *Astrophysical Journal* **433**, 797

Kamphuis, J. and Sancisi, R.: 1993, Widespread High Velocity Gas in the Spiral Galaxy NGC6946, *Astronomy and Astrophysics* **273**, L31

Kaneda, Y., Ishihara, T., Yokokawa, M., Itakura, K., and Uno, A.: 2003, Energy dissipation rate and energy spectrum in high resolution direct numerical simulations of turbulence in a periodic box, *Physics of Fluids* **15**, L21

Karachentsev, I. D., Sharina, M. E., Dolphin, A. E., Grebel, E. K., Geisler, D., Guhathakurta, P., Hodge, P. W., Karachentseva, V. E., Sarajedini, A., and Seitzer, P.: 2002, New distances to galaxies in the Centaurus A group, *Astronomy and Astrophysics* **385**, 21

Kennicutt, R. C.: 1998, The Global Schmidt Law in Star-forming Galaxies, *Astrophysical Journal* **498**, 541

Kerp, J., Walter, F., and Brinks, E.: 2002, ROSAT X-Ray Observations of the Dwarf Galaxy Holmberg II, *Astrophysical Journal* **571**, 809

Kessel-Deynet, O. and Burkert, A.: 2003, Radiation-driven implosion of molecular cloud cores, *Monthly Notices of the Royal Astronomical Society* **338**, 545

Khanzadyan, T., Gredel, R., Smith, M. D., and Stanke, T.: 2004, An unbiased search for the signatures of protostars in the ρ Ophiuchi A molecular cloud. I. Near-infrared observations, *Astronomy and Astrophysics* **426**, 171

Kim, J., Balsara, D., and Mac Low, M.: 2001, Turbulence Driven by Supernova Explosions in a Radiatively-Cooling Magnetized Interstellar Medium, *Journal of Korean Astronomical Society* **34**, 333

Kim, S., Dopita, M. A., Staveley-Smith, L., and Bessell, M. S.: 1999, H I Shells in the Large Magellanic Cloud, *Astronomical Journal* **118**, 2797

Kim, S., Martin, P. G., and Hendry, P. D.: 1994, The size distribution of interstellar dust particles as determined from extinction, *Astrophysical Journal* **422**, 164

Kolesnik, I. G.: 1991, Formation of giant molecular cloud complexes in galaxies, *Astronomy and Astrophysics* **243**, 239

Kolmogorov, A. N.: 1941, The local structure of turbulence in incompressible viscous fluid for very large Reynolds numbers, *Dokl. Akad. Nauk. SSSR (Reprinted in Proc. R. Soc. Lond. A 434, 9, 1991)* **30**, 9

Korpi, M. J.: 1999, Interstellar turbulence and magnetic fields: The role of supernova explosions, *Ph.D. Thesis*

Korpi, M. J., Brandenburg, A., Shukurov, A., and Tuominen, I.: 1999a, Evolution of a superbubble in a turbulent, multi-phased and magnetized ISM, *Astronomy and Astrophysics* **350**, 230

Korpi, M. J., Brandenburg, A., Shukurov, A., Tuominen, I., and Nordlund, Å.: 1999b, A Supernova-regulated Interstellar Medium: Simulations of the Turbulent Multiphase Medium, *Astrophysical Journal Letters* **514**, L99

Koyama, H. and Inutsuka, S.: 2000, Molecular Cloud Formation in Shock-compressed Layers, *Astrophysical Journal* **532**, 980

Koyama, H. and Inutsuka, S.: 2002, An Origin of Supersonic Motions in Interstellar Clouds, *Astrophysical Journal Letters* **564**, L97

Koyama, H. and Inutsuka, S.: 2004, The Field Condition: A New Constraint on Spatial Resolution in Simulations of the Nonlinear Development of Thermal Instability, *Astrophysical Journal Letters* **602**, L25

Kritsuk, A. G. and Norman, M. L.: 2002a, Interstellar Phase Transitions Stimulated by Time-dependent Heating, *Astrophysical Journal Letters* **580**, L51

Kritsuk, A. G. and Norman, M. L.: 2002b, Thermal Instability-induced Interstellar Turbulence, *Astrophysical Journal Letters* **569**, L127

Kroupa, P. and Bouvier, J.: 2003, On the origin of brown dwarfs and free-floating planetary-mass objects, *Monthly Notices of the Royal Astronomical Society* **346**, 369

Kulkarni, S. R., Heiles, C., and Blitz, L.: 1982, Atomic hydrogen in the outer Milky Way, *Astrophysical Journal Letters* **259**, L63

Kulsrud, R. M.: 1999, A Critical Review of Galactic Dynamos, *Annual Review of Astronomy and Astrophysics* **37**, 37

Lagache, G., Abergel, A., Boulanger, F., and Puget, J.-L.: 1998, The interstellar cold dust observed by COBE, *Astronomy and Astrophysics* **333**, 709

Landau, L. D. and Lifshitz, E. M.: 1959, *Fluid mechanics*, Course of theoretical physics, Oxford: Pergamon Press, 1959

Lang, K. R.: 1980, *Astrophysical Formulae*, A Compendium for the Physicist and Astrophysicist. Springer-Verlag Berlin Heidelberg New York.

Larson, R. B.: 1981, Turbulence and star formation in molecular clouds, *Monthly Notices of the Royal Astronomical Society* **194**, 809

Leitherer, C.: 1999, The stellar initial mass function in local dwarf galaxies, *in Dwarf Galaxies and Cosmology, ed. T. X. Thuan, C. Balkowski, V. Cayette, & J. Trân Thanh Vân (Gif-sur-Yvette: Ed. Frontière)* p. 235

Lepp, S. and Shull, J. M.: 1983, The kinetic theory of H2 dissociation, *Astrophysical Journal* **270**, 578

Li, A. and Greenberg, J. M.: 1997, A unified model of interstellar dust., *Astronomy and Astrophysics* **323**, 566

Loren, R. B.: 1989, The cobwebs of Ophiuchus. I - Strands of (C-13)O - The mass distribution, *Astrophysical Journal* **338**, 902

Mac Low, M.: 1999, The Energy Dissipation Rate of Supersonic, Magnetohydrodynamic Turbulence in Molecular Clouds, *Astrophysical Journal* **524**, 169

Mac Low, M.: 2004, Turbulence in the Interstellar Medium, *Astrophysics and Space Science* **289**, 323

Mac Low, M. and Klessen, R. S.: 2004, Control of star formation by supersonic turbulence, *Reviews of Modern Physics* **76**, 125

Mac Low, M., Klessen, R. S., Burkert, A., and Smith, M. D.: 1998, Kinetic Energy Decay Rates of Supersonic and Super-Alfvénic Turbulence in Star-Forming Clouds, *Physical Review Letters* **80**, 2754

Mallik, D. C. V.: 1975, Temperature and Emission-Line Structure at the Edges of H II Regions, *Astrophysical Journal* **197**, 355

Martin, C. L. and Kennicutt, R. C.: 2001, Star Formation Thresholds in Galactic Disks, *Astrophysical Journal* **555**, 301

Masunaga, H. and Inutsuka, S.: 2000, A Radiation Hydrodynamic Model for Protostellar Collapse. II. The Second Collapse and the Birth of a Protostar, *Astrophysical Journal* **531**, 350

Masunaga, H., Miyama, S. M., and Inutsuka, S.: 1998, A Radiation Hydrodynamic Model for Protostellar Collapse. I. The First Collapse, *Astrophysical Journal* **495**, 346

Mathewson, D. S. and Ford, V. L.: 1970, Polarization observations of 1800 stars, *Mem. R. Astron. Soc.* **74**, 139

Mathis, J. S., Rumpl, W., and Nordsieck, K. H.: 1977, The size distribution of interstellar grains, *Astrophysical Journal* **217**, 425

Matzner, C. D.: 2002, On the Role of Massive Stars in the Support and Destruction of Giant Molecular Clouds, *Astrophysical Journal* **566**, 302

McCammon, D. and Sanders, W. T.: 1990, The soft X-ray background and its origins, *Annual Review of Astronomy and Astrophysics* **28**, 657

McKee, C. F.: 1989, Photoionization-regulated star formation and the structure of molecular clouds, *Astrophysical Journal* **345**, 782

McKee, C. F.: 1995, The Multiphase Interstellar Medium *in ASP Conf. Ser. 80: The Physics of the Interstellar Medium and Intergalactic Medium*, p. 292

McKee, C. F.: 1999, The Dynamical Structure and Evolution of Giant Molecular Clouds *in NATO ASIC Proc. 540: The Origin of Stars and Planetary Systems*, p. 29

McKee, C. F. and Begelman, M. C.: 1990, Steady evaporation and condensation of isolated clouds in hot plasma, *Astrophysical Journal* **358**, 392

McKee, C. F. and Cowie, L. L.: 1977, The evaporation of spherical clouds in a hot gas. II - Effects of radiation, *Astrophysical Journal* **215**, 213

McKee, C. F. and Ostriker, J. P.: 1977, A theory of the interstellar medium - Three components regulated by supernova explosions in an inhomogeneous substrate, *Astrophysical Journal* **218**, 148

McKee, C. F. and Williams, J. P.: 1997, The Luminosity Function of OB Associations in the Galaxy, *Astrophysical Journal* **476**, 144

McKee, C. F. and Zweibel, E. G.: 1992, On the virial theorem for turbulent molecular clouds, *Astrophysical Journal* **399**, 551

McKee, C. F. and Zweibel, E. G.: 1995, Alfven Waves in Interstellar Gasdynamics, *Astrophysical Journal* **440**, 686

Mestel, L. and Spitzer, L.: 1956, Star formation in magnetic dust clouds, *Monthly Notices of the Royal Astronomical Society* **116**, 503

Meurer, G. R., Carignan, C., Beaulieu, S. F., and Freeman, K. C.: 1996, NGC 2915.II.A Dark Spiral Galaxy With a Blue Compact Dwarf Core, *Astronomical Journal* **111**, 1551

Meurer, G. R., Mackie, G., and Carignan, C.: 1994, Optical observations of NGC 2915: A nearby blue compact dwarf galaxy, *Astronomical Journal* **107**, 2021

Miesch, M. S. and Bally, J.: 1994, Statistical analysis of turbulence in molecular clouds, *Astrophysical Journal* **429**, 645

Mihalas, D. and Binney, J.: 1981, *Galactic astronomy: Structure and kinematics*, San Francisco, CA, W. H. Freeman and Co.

Miller, G. E. and Scalo, J. M.: 1979, The initial mass function and stellar birthrate in the solar neighborhood, *Astrophysical Journal Supplement Series* **41**, 513

Moss, D. and Shukurov, A.: 1996, Turbulence and magnetic fields in elliptical galaxies., *Monthly Notices of the Royal Astronomical Society* **279**, 229

Mouschovias, T. C. and Spitzer, L.: 1976, Note on the collapse of magnetic interstellar clouds, *Astrophysical Journal* **210**, 326

Muller, E., Staveley-Smith, L., Zealey, W., and Stanimirović, S.: 2003, High-resolution HI observations of the Western Magellanic Bridge, *Monthly Notices of the Royal Astronomical Society* **339**, 105

Myers, P. C. and Goodman, A. A.: 1988, Evidence for magnetic and virial equilibrium in molecular clouds, *Astrophysical Journal Letters* **326**, L27

Norman, M. L., Wilson, J. R., and Barton, R. T.: 1980, A new calculation on rotating protostar collapse, *Astrophysical Journal* **239**, 968

Oort, J. H., Kerr, F. J., and Westerhout, G.: 1958, The galactic system as a spiral nebula (Council Note), *Monthly Notices of the Royal Astronomical Society* **118**, 379

Ossenkopf, V. and Mac Low, M.-M.: 2002, Turbulent velocity structure in molecular clouds, *Astronomy and Astrophysics* **390**, 307

Parker, E. N.: 1953, Instability of Thermal Fields., *Astrophysical Journal* **117**, 431

Parker, E. N.: 1979, *Cosmical magnetic fields: Their origin and their activity*, Oxford, Clarendon Press; New York, Oxford University Press, 1979, 858 p.

Passot, T., Vázquez-Semadeni, E., and Pouquet, A.: 1995, A Turbulent Model for the Interstellar Medium. II. Magnetic Fields and Rotation, *Astrophysical Journal* **455**, 536

Pavlovski, G., Smith, M. D., Mac Low, M., and Rosen, A.: 2002, Hydrodynamical simulations of the decay of high-speed molecular turbulence - I. Dense molecular regions, *Monthly Notices of the Royal Astronomical Society* **337**, 477

Pendleton, Y. J. and Allamandola, L. J.: 2002, The Organic Refractory Material in the Diffuse Interstellar Medium: Mid-Infrared Spectroscopic Constraints, *Astrophysical Journal Supplement Series* **138**, 75

Penston, M. V. and Brown, F. E.: 1970, The doud-intercloud phase-change in the interstellar medium, *Monthly Notices of the Royal Astronomical Society* **150**, 373

Piontek, R. A. and Ostriker, E. C.: 2004, Thermal and Magnetorotational Instability in the Interstellar Medium: Two-dimensional Numerical Simulations, *Astrophysical Journal* **601**, 905

Prantzos, N. and Silk, J.: 1998, Star Formation and Chemical Evolution in the Milky Way: Cosmological Implications, *Astrophysical Journal* **507**, 229

Press, W. H., Teukolsky, S. A., Vetterling, W. T., and Flannery, B. P.: 1992, *Numerical recipes in FORTRAN. The art of scientific computing*, Cambridge: University Press, —c1992, 2nd ed.

Puche, D., Westpfahl, D., Brinks, E., and Roy, J.: 1992, Holmberg II - A laboratory for studying the violent interstellar medium, *Astronomical Journal* **103**, 1841

Rachford, B. L., Snow, T. P., Tumlinson, J., Shull, J. M., Roueff, E., Andre, M., Desert, J.-M., Ferlet, R., Vidal-Madjar, A., and York, D. G.: 2001, Far Ultraviolet Spectroscopic Explorer Observations of Molecular Hydrogen in Translucent Interstellar Clouds. II. The Line of Sight toward HD 110432, *Astrophysical Journal* **555**, 839

Reipurth, B. and Clarke, C.: 2001, The Formation of Brown Dwarfs as Ejected Stellar Embryos, *Astronomical Journal* **122**, 432

Reynolds, R. J.: 1985, The forbidden line of S II lambda 6716 in the galactic emission-line background, *Astrophysical Journal* **294**, 256

Reynolds, R. J.: 1989, The column density and scale height of free electrons in the galactic disk, *Astrophysical Journal Letters* **339**, L29

Rhode, K. L., Salzer, J. J., Westpfahl, D. J., and Radice, L. A.: 1999, A Test of the Standard Hypothesis for the Origin of the H I Holes in Holmberg II, *Astronomical Journal* **118**, 323

Rohlfs, K. and Wilson, T. L.: 1996, *Tools of Radio Astronomy*, Tools of Radio Astronomy, XVI, 423 pp. Springer-Verlag Berlin Heidelberg New York

Rosen, A. and Bregman, J. N.: 1995, Global Models of the Interstellar Medium in Disk Galaxies, *Astrophysical Journal* **440**, 634

Rownd, B. K., Dickey, J. M., and Helou, G.: 1994, H I distribution and kinematics in the peculiar spiral galaxy NGC 5474, *Astronomical Journal* **108**, 1638

Ruzmaikin, A., Sokolov, D., and Shukurov, A.: 1988, Magnetism of spiral galaxies, *Nature* **336**, 341

Sánchez-Salcedo, F. J.: 2001, On the Formation of Giant Holes in the Interstellar Medium by Disk Instabilities, *Astrophysical Journal* **563**, 867

Sánchez-Salcedo, F. J.: 2002, A New Look at the Holes of IC 2574, *Revista Mexicana de Astronomia y Astrofisica* **38**, 39

Sánchez-Salcedo, F. J., Vázquez-Semadeni, E., and Gazol, A.: 2002, The Nonlinear Development of the Thermal Instability in the Atomic Interstellar Medium and Its Interaction with Random Fluctuations, *Astrophysical Journal* **577**, 768

Salpeter, E. E.: 1955, The Luminosity Function and Stellar Evolution., *Astrophysical Journal* **121**, 161

Salpeter, E. E.: 1976, Planetary nebulae, supernova remnants, and the interstellar medium /The Henry Norris Russell Lecture/, *Astrophysical Journal* **206**, 673

Savage, B. D. and Jenkins, E. P.: 1972, A Survey of Local Interstellar Hydrogen from OAO-2 Observations of Lyman Alpha Absorption., *Astrophysical Journal* **172**, 491

Savage, B. D., Sembach, K. R., Jenkins, E. B., Shull, J. M., York, D. G., Sonneborn, G., Moos, H. W., Friedman, S. D., Green, J. C., Oegerle, W. R., Blair, W. P., Kruk, J. W., and Murphy, E. M.: 2000, Far Ultraviolet Spectroscopic Explorer Observations of O VI Absorption in the Galactic Halo, *Astrophysical Journal Letters* **538**, L27

Savage, B. D., Sembach, K. R., and Lu, L.: 1997, Absorption by Highly Ionized Interstellar Gas Along Extragalactic and Galactic Sight Lines, *Astronomical Journal* **113**, 2158

Scalo, J.: 1990, Perception of interstellar structure - Facing complexity *ASSL Vol. 162: Physical Processes in Fragmentation and Star Formation*, p. 151

Scalo, J. and Chappell, D.: 1999, Clustering Properties of Stars in Simulations of Wind-DrivenStar Formation, *Astrophysical Journal* **510**, 258

Scalo, J. M.: 1985, Fragmentation and hierarchical structure in the interstellar medium *in Protostars and Planets II*, p. 201

Scalo, J. M.: 1987, Theoretical approaches to interstellar turbulence *ASSL Vol. 134: Interstellar Processes*, p. 349

Scheffler, H. and Elsaesser, H.: 1987, *Physics of the galaxy and interstellar matter*, Berlin and New York, Springer-Verlag, 1987

Schmidt, M.: 1959, The Rate of Star Formation., *Astrophysical Journal* **129**, 243

Scoville, N. Z. and Sanders, D. B.: 1987, H2 in the Galaxy *in Interstellar Processes*, Edited by D. J. Hollenbach and H. A. Thronson, Jr. (Reidel, Dordrecht), p. 21

Sellwood, J. A. and Balbus, S. A.: 1999, Differential Rotation and Turbulence in Extended H I Disks, *Astrophysical Journal* **511**, 660

Serkowski, K.: 1973, Interstellar Polarization *IAU Symp. 52: Interstellar Dust and Related Topics*, p. 145

Shadmehri, M., Vázquez-Semadeni, E., and Ballesteros-Paredes, J.: 2002, Virial Theorem Analysis of 3D Numerical Simulations of MHD Self-Gravitating Turbulence, *itin ASP Conf. Ser. 276: Seeing Through the Dust: The Detection of HI and the Exploration of the ISM in Galaxies* p. 190

Shore, S. N.: 1992, *An introduction to astrophysical hydrodynamics*, San Diego: Academic Press, —c1992

Shostak, G. S. and van der Kruit, P. C.: 1984, Studies of nearly face-on spiral galaxies. II - H I synthesis observations and optical surface photometry of NGC 628, *Astronomy and Astrophysics* **132**, 20

Shu, F. H.: 1977, Self-similar collapse of isothermal spheres and star formation, *Astrophysical Journal* **214**, 488

Shu, F. H.: 1992, *Physics of Astrophysics, Vol. II: Gas dynamics*, A series of books in Astronomy, Mill Valley, CA : University Science Books

Shu, F. H., Adams, F. C., and Lizano, S.: 1987, Star formation in molecular clouds - Observation and theory, *Annual Review of Astronomy and Astrophysics* **25**, 23

Shu, F. H., Lizano, S., Ruden, S. P., and Najita, J.: 1988, Mass loss from rapidly rotating magnetic protostars, *Astrophysical Journal Letters* **328**, L19

Shull, J. M., Tumlinson, J., Jenkins, E. B., Moos, H. W., Rachford, B. L., Savage, B. D., Sembach, K. R., Snow, T. P., Sonneborn, G., York, D. G., Blair, W. P., Green, J. C., Friedman, S. D., and Sahnow, D. J.: 2000, Far Ultraviolet Spectroscopic Explorer Observations of Diffuse Interstellar Molecular Hydrogen, *Astrophysical Journal Letters* **538**, L73

Shull, J. M. and van Steenberg, M. E.: 1985a, Galactic interstellar abundance surveys with IUE. I - Neutral hydrogen, *Astrophysical Journal* **294**, 599

Shull, J. M. and van Steenberg, M. E.: 1985b, X-ray secondary heating and ionization in quasar emission-line clouds, *Astrophysical Journal*

Smith, M. D., Mac Low, M.-M., and Zuev, J. M.: 2000, The shock waves in decaying supersonic turbulence, *Astronomy and Astrophysics* **356**, 287

Smith, M. D. and Rosen, A.: 2003, The instability of fast shocks in molecular clouds, *Monthly Notices of the Royal Astronomical Society* **339**, 133

Snowden, S. L., Egger, R., Finkbeiner, D. P., Freyberg, M. J., and Plucinsky, P. P.: 1998, Progress on Establishing the Spatial Distribution of Material Responsible for the 1 4 keV Soft X-Ray Diffuse Background Local and Halo Components, *Astrophysical Journal* **493**, 715

Solomon, P. M., Rivolo, A. R., Barrett, J., and Yahil, A.: 1987, Mass, luminosity, and line width relations of Galactic molecular clouds, *Astrophysical Journal* **319**, 730

Spitzer, L.: 1962, *Physics of Fully Ionized Gases*, New York: Interscience (2nd edition), 1962

Spitzer, L.: 1978, *Physical processes in the interstellar medium*, New York Wiley-Interscience, 1978. 333 p.

Spitzer, L. and Jenkins, E. B.: 1975, Ultraviolet studies of the interstellar gas, *Annual Review of Astronomy and Astrophysics* **13**, 133

Spitzer, L. J.: 1956, On a Possible Interstellar Galactic Corona., *Astrophysical Journal* **124**, 20

Stanimirović, S. and Lazarian, A.: 2001, Velocity and Density Spectra of the Small Magellanic Cloud, *Astrophysical Journal Letters* **551**, L53

Stanimirovic, S., Staveley-Smith, L., Dickey, J. M., Sault, R. J., and Snowden, S. L.: 1999, The large-scale HI structure of the Small Magellanic Cloud, *Monthly Notices of the Royal Astronomical Society* **302**, 417

Staveley-Smith, L., Sault, R. J., Hatzidimitriou, D., Kesteven, M. J., and McConnell, D.: 1997, An HI aperture synthesis mosaic of the Small Magellanic Cloud, *Monthly Notices of the Royal Astronomical Society* **289**, 225

Stecher, T. P. and Donn, B.: 1965, On Graphite and Interstellar Extinction, *Astrophysical Journal* **142**, 1681

Stewart, S. G., Fanelli, M. N., Byrd, G. G., Hill, J. K., Westpfahl, D. J., Cheng, K., O'Connell, R. W., Roberts, M. S., Neff, S. G., Smith, A. M., and Stecher, T. P.: 2000, Star Formation Triggering Mechanisms in Dwarf Galaxies: The Far-Ultraviolet, Hα, and H I Morphology of Holmberg II, *Astrophysical Journal* **529**, 201

Stil, J. M. and Israel, F. P.: 2002, HI distribution and kinematics of NGC 1569, *Astronomy and Astrophysics* **392**, 473

Stone, J. M. and Norman, M. L.: 1992a, ZEUS-2D: A radiation magnetohydrodynamics code for astrophysical flows in two space dimensions. I - The hydrodynamic algorithms and tests., *Astrophysical Journal Supplement Series* **80**, 753

Stone, J. M. and Norman, M. L.: 1992b, ZEUS-2D: A Radiation Magnetohydrodynamics Code for Astrophysical Flows in Two Space Dimensions. II. The Magnetohydrodynamic Algorithms and Tests, *Astrophysical Journal Supplement Series* **80**, 791

Stone, J. M., Ostriker, E. C., and Gammie, C. F.: 1998, Dissipation in Compressible Magnetohydrodynamic Turbulence, *Astrophysical Journal Letters* **508**, L99

Strickland, D. K., Heckman, T. M., Colbert, E. J. M., Hoopes, C. G., and Weaver, K. A.: 2004a, A High Spatial Resolution X-Ray and Hα Study of Hot Gas in the Halos of Star-forming Disk Galaxies. I. Spatial and Spectral Properties of the Diffuse X-Ray Emission, *Astrophysical Journal Supplement Series*

Strickland, D. K., Heckman, T. M., Colbert, E. J. M., Hoopes, C. G., and Weaver, K. A.: 2004b, A High Spatial Resolution X-Ray and Hα Study of Hot Gas in the Halos of Star-forming Disk Galaxies. II. Quantifying Supernova Feedback, *Astrophysical Journal*

Sutherland, R. S. and Dopita, M. A.: 1993, Cooling functions for low-density astrophysical plasmas, *Astrophysical Journal Supplement Series* **88**, 253

Tammann, G. A., Loeffler, W., and Schroeder, A.: 1994, The Galactic supernova rate, *Astrophysical Journal Supplement Series* **92**, 487

Tenorio-Tagle, G. and Bodenheimer, P.: 1988, Large-scale expanding superstructures in galaxies, *Annual Review of Astronomy and Astrophysics* **26**, 145

Thornton, K., Gaudlitz, M., Janka, H.-T., and Steinmetz, M.: 1998, Energy Input and Mass Redistribution by Supernovae in the Interstellar Medium, *Astrophysical Journal* **500**, 95

Trumpler, R. J.: 1930, Absorption of Light in the Galactic System, *Publications of the Astronomical Society of the Pacific* **42**, 214

Tully, R. B., Bottinelli, L., Gougenheim, L., Fisher, J. R., Sancisi, R., and van Woerden, H.: 1978, Gas distribution, motions and dynamics for some dwarf irregular galaxies, *Astronomy and Astrophysics* **63**, 37

Valentijn, E. A. and van der Werf, P. P.: 1999, First Extragalactic Direct Detection of Large-Scale Molecular Hydrogen in the Disk of NGC 891, *Astrophysical Journal Letters* **522**, L29

van den Bergh, S. and McClure, R. D.: 1990, Supernova rates and galaxy inclinations, *Astrophysical Journal* **359**, 277

van der Hulst, T. and Sancisi, R.: 1988, High-velocity gas in M101, *Astronomical Journal* **95**, 1354

van der Kruit, P. C. and Shostak, G. S.: 1982, Studies of nearly face-on spiral galaxies. I - The velocity dispersion of the H I gas in NGC 3938, *Astronomy and Astrophysics* **105**, 351

van Leer, B.: 1977, Towards the ultimate conservative difference scheme: IV. A new approach to numerical convection, *Journal of Computational Physics* **23**, 276

van Zee, L.: 2001, The Evolutionary Status of Isolated Dwarf Irregular Galaxies. II. Star Formation Histories and Gas Depletion, *Astronomical Journal* **121**, 2003

van Zee, L., Maddalena, R. J., Haynes, M. P., Hogg, D. E., and Roberts, M. S.: 1997, Obtaining High Precision HI Fluxes for Galaxies, *Astronomical Journal* **113**, 1638

Vázquez-Semadeni, E.: 1994, Hierarchical Structure in Nearly Pressureless Flows as a Consequence of Self-similar Statistics, *Astrophysical Journal* **423**, 681

Vázquez-Semadeni, E.: 2002, Numerical Models of the ISM *in ASP Conf. Ser. 276: Seeing Through the Dust: The Detection of HI and the Exploration of the ISM in Galaxies*, p. 155

Vázquez-Semadeni, E., Ballesteros-Paredes, J., and Rodriguez, L. F.: 1997, A Search for Larson-Type Relations in Numerical Simulations of the ISM: Evidence for Nonconstant Column Densities, *Astrophysical Journal* **474**, 292

Vázquez-Semadeni, E. and Gazol, A.: 1995, Gravitational instability in turbulent, non-uniform media., *Astronomy and Astrophysics* **303**, 204

Vázquez-Semadeni, E., Gazol, A., and Scalo, J.: 2000a, Is Thermal Instability Significant in Turbulent Galactic Gas?, *Astrophysical Journal* **540**, 271

Vázquez-Semadeni, E., Ostriker, E. C., Passot, T., Gammie, C. F., and Stone, J. M.: 2000b, Compressible MHD Turbulence: Implications for Molecular Cloud and Star Formation, *Protostars and Planets IV* p. 3

Vivekanand, M. and Narayan, R.: 1982, Interstellar electron density, *Journal of Astrophysics and Astronomy* **3**, 399

von Neumann, J. and Richtmyer, R. D.: 1950, , *J. Appl. Phys* **21**, 232

Wada, K., Meurer, G., and Norman, C. A.: 2002, Gravity-driven Turbulence in Galactic Disks, *Astrophysical Journal* **577**, 197

Wada, K. and Norman, C. A.: 1999, The Global Structure and Evolution of a Self-Gravitating Multiphase Interstellar Medium in a Galactic Disk, *Astrophysical Journal Letters* **516**, L13

Wada, K. and Norman, C. A.: 2001, Numerical Models of the Multiphase Interstellar Matter with Stellar Energy Feedback on a Galactic Scale, *Astrophysical Journal* **547**, 172

Wada, K., Spaans, M., and Kim, S.: 2000, Formation of Cavities, Filaments, and Clumps by the Nonlinear Development of Thermal and Gravitational Instabilities in the Interstellar Medium under Stellar Feedback, *Astrophysical Journal* **540**, 797

Wakker, B. P., Savage, B. D., Sembach, K. R., Richter, P., Meade, M., Jenkins, E. B., Shull, J. M., Ake, T. B., Blair, W. P., Dixon, W. V., Friedman, S. D., Green, J. C., Green, R. F., Kruk, J. W., Moos, H. W., Murphy, E. M., Oegerle, W. R., Sahnow, D. J., Sonneborn, G., Wilkinson, E., and York, D. G.: 2003, The Far Ultraviolet Spectroscopic Explorer Survey of O VI Absorption in and near the Galaxy, *Astrophysical Journal Supplement Series* **146**, 1

Walter, F. and Brinks, E.: 1999, Holes and Shells in the Interstellar Medium of the Nearby Dwarf Galaxy IC 2574, *Astronomical Journal* **118**, 273

Warren, B. E., Jerjen, H., and Koribalski, B. S.: 2004, ESO 215-G?009: An Extreme H I-Rich Dwarf Irregular Galaxy, *Astronomical Journal* **128**, 1152

Weingartner, J. C. and Draine, B. T.: 2001a, Dust Grain-Size Distributions and Extinction in the Milky Way, Large Magellanic Cloud, and Small Magellanic Cloud, *Astrophysical Journal*

Weingartner, J. C. and Draine, B. T.: 2001b, Photoelectric Emission from Interstellar Dust: Grain Charging and Gas Heating, *Astrophysical Journal Supplement Series*

Wielebinski, R. and Krause, F.: 1993, Magnetic fields in galaxies, *Astronomy and Astrophysics Review* **4**, 449

Williams, J. P., de Geus, E. J., and Blitz, L.: 1994, Determining structure in molecular clouds, *Astrophysical Journal* **428**, 693

Wolff, M. J., Clayton, G. C., Kim, S., Martin, P. G., and Anderson, C. M.: 1997, Ultraviolet Interstellar Linear Polarization. III. Features, *Astrophysical Journal* **478**, 395

Wolfire, M. G., Hollenbach, D., McKee, C. F., Tielens, A. G. G. M., and Bakes, E. L. O.: 1995, The neutral atomic phases of the interstellar medium, *Astrophysical Journal* **443**, 152

Wong, T. and Blitz, L.: 2002, The Relationship between Gas Content and Star Formation in Molecule-rich Spiral Galaxies, *Astrophysical Journal* **569**, 157

Wood, D. O. S., Myers, P. C., and Daugherty, D. A.: 1994, IRAS images of nearby dark clouds, *Astrophysical Journal Supplement Series* **95**, 457

Woosley, S. E. and Weaver, T. A.: 1986, The physics of supernova explosions, *Annual Review of Astronomy and Astrophysics* **24**, 205

Wuchterl, G. and Klessen, R. S.: 2001, The First Million Years of the Sun: A Calculation of the Formation and Early Evolution of a Solar Mass Star, *Astrophysical Journal Letters* **560**, L185

Wuchterl, G. and Tscharnuter, W. M.: 2003, From clouds to stars. Protostellar collapse and the evolution to the pre-main sequence I. Equations and evolution in the Hertzsprung-Russell diagram, *Astronomy and Astrophysics* **398**, 1081

York, D. G.: 1974, Highly ionized atoms observed with Copernicus, *Astrophysical Journal Letters* **193**, L127

Young, L. M.: 2002, Molecular Gas in Elliptical Galaxies: Distribution and Kinematics, *Astronomical Journal* **124**, 788

Yusef-Zadeh, F., Roberts, D. A., Goss, W. M., Frail, D. A., and Green, A. J.: 1996, Detection of 1720 MHz Hydroxl Masers at the Galactic Center: Evidence for Shock-excited Gas and Milligauss Fields, *Astrophysical Journal Letters* **466**, L25

Zel'dovich, Y. B. and Pikel'ner, S. B.: 1969, *Soviet Phys.-JETP* **29**, 170

Zezas, A. L., Georgantopoulos, I., and Ward, M. J.: 1999, ROSAT observations of the dwarf star-forming galaxy Holmberg II (UGC 4305), *Monthly Notices of the Royal Astronomical Society* **308**, 302

Zubko, V. G., Krelowski, J., and Wegner, W.: 1996, The size distribution of dust grains in single clouds.I. The analysis of extinction using multicomponents mixtures of bare spherical grains., *Monthly Notices of the Royal Astronomical Society* **283**, 577

Zweibel, E. G. and Heiles, C.: 1997, Magnetic fields in galaxies and beyond., *Nature* **385**, 131

... "*who teaches me a word, I am his slave*" (Imam Ali). I here take the occasion to thank those who helped me increase my knowledge

My supervisor, Prof. Andreas Burkert for giving me the chance to start this work in his group, his patience, and continued support. Dear Andi, I keep in mind what I have heard from you once that "Ein Tag ohne Paper ist kein Tag".

Prof. Hans-Walter Rix and Prof. Thomas Henning for the interest they had in my work, moral support, and their efforts to provide the necessary fuel of war to keep my projects going. Without your assistance, things would have been slightly more difficult.

Prof. Matthias Bartelmann and Prof. Ulrich Platt for kindly accepting to be members of the examination jury.

many collaborators, Dr Eric Bell for analysing the bubbles with me but also for the interesting discussions; Eric, I am looking forward for more theory-observations matching with you, Dr Fabian Heitsch (code business but mostly for the sympathy), Dr Katherine Rhode (for the data), Dr Javier-Ballesteros Paredes and Prof. Enrique Vazquez-Semadeni for lively discussions about everything interstellar, Prof. Axel Brandenburg and Dr Maarit Korpi for the interesting discussions I had with them at NORDITA, Dr Micheal Smith for the many advices, at many different times. I also wish to thank Dr Hubert Klahr, Dr Fabian Walter and Dr Kees Dullemond for proof-reading parts of this thesis, Dr Jürgen Steinacker for many things, in particular for setting the webpage for the football bets (my secret source of income at MPIA). I am also very grateful to all the friendly people, too many to name here, who helped me in multiple ways during my thesis. Despite some annoying events like a broken knee here and there... I have really enjoyed being here.

Roland, my faithfull ally in the raids against the night elves and the terrible burning legion, und Frau Astrid Jesseit für die warme Gastfreundschaft in Hamburg.

Jakob, pour tout, surtout les multiples dépannages, question logement.

my numerous friends all around the globe. I will get back to each of you,

the people of the South, for they have tought me pride and strength. The stars under the skies of Jabal Amel, sometime ago, looked different, had a different meaning than burning hydrogen spheres, and probably ... have inspired this thesis,

my larger family (including of course all the cousins, sons and daughters of cousins, ect ...), ... yes I know, I know, wisdom would have wanted me to do business or study medecine. I go from the principle that there has to be a perturber of the peace in each family. I have here a particular thought to my grandfathers, Marcel and Hassan. The latter taught me, wisely, he who never had the chance to attend any school, that life is all about "beautiful patience",

My parents, Dr Ahmad and Marie-Louise and my brother Walid as they really tried hard to convince the rest of the family (especially the cousins..) that studying astronomy is not so bad afterall. Who convinced whom at the end needs further investigation.